CNWRA 2003-01

PASSIVE DISSOLUTION OF CONTAINER MATERIALS—MODELING AND EXPERIMENTS

Prepared for

U.S. Nuclear Regulatory Commission
Contract NRC–02–02–012

Prepared by

Center for Nuclear Waste Regulatory Analyses
San Antonio, Texas

October 2002

CNWRA 2003-01

PASSIVE DISSOLUTION OF CONTAINER MATERIALS—MODELING AND EXPERIMENTS

Prepared for

U.S. Nuclear Regulatory Commission
Contract NRC–02–02–012

Prepared by

O. Pensado
D.S. Dunn
G.A. Cragnolino
V. Jain

Center for Nuclear Waste Regulatory Analyses
San Antonio, Texas

October 2002

PREVIOUS REPORTS IN SERIES

Number	Name	Date Issued
CNWRA 91-004	A Review of Localized Corrosion of High-Level Nuclear Waste Container Materials—I	April 1991
CNWRA 91-008	Hydrogen Embrittlement of Candidate Container Materials	June 1991
CNWRA 92-021	A Review of Stress Corrosion Cracking of High-Level Nuclear Waste Container Materials—I	August 1992
CNWRA 93-003	Long-Term Stability of High-Level Nuclear Waste Container Materials: I—Thermal Stability of Alloy 825	February 1993
CNWRA 93-004	Experimental Investigations of Localized Corrosion of High-Level Nuclear Waste Container Materials	February 1993
CNWRA 93-014	A Review of the Potential for Microbially Influenced Corrosion of High-Level Nuclear Waste Containers	June 1993
CNWRA 94-010	A Review of Degradation Modes of Alternate Container Designs and Materials	April 1994
CNWRA 94-028	Environmental Effects on Stress Corrosion Cracking of Type 316L Stainless Steel and Alloy 825 as High-Level Nuclear Waste Container Materials	October 1994
CNWRA 95-010	Experimental Investigations of Failure Processes of High-Level Radioactive Waste Container Materials	May 1995
CNWRA 95-020	Expert-Panel Review of the Integrated Waste Package Experiments Research Project	September 1995
CNWRA 96-004	Thermal Stability and Mechanical Properties of High-Level Radioactive Waste Container Materials: Assessment of Carbon and Low-Alloy Steels	May 1996
CNWRA 97-010	An Analysis of Galvanic Coupling Effects on the Performance of High-Level Nuclear Waste Container Materials	August 1997
CNWRA 98-004	Effect of Galvanic Coupling Between Overpack Materials of High-Level Nuclear Waste Containers—Experimental and Modeling Results	March 1998

PREVIOUS REPORTS IN SERIES (continued)

Number	Name	Date Issued
CNWRA 98-008	Effects of Environmental Factors on Container Life	July 1998
CNWRA 99-003	Assessment of Performance Issues Related to Alternate Engineered Barrier System Materials and Design Options	September 1999
CNWRA 99-004	Effects of Environmental Factors on the Aqueous Corrosion of High-Level Radioactive Waste Containers—Experimental Results and Models	September 1999
CNWRA 2000-06 Revision 1	Assessment of Methodologies to Confirm Container Performance Model Predictions	January 2001
CNWRA 2001-003	Effect of Environment on the Corrosion of Waste Package and Drip Shield Materials	September 2001
CNWRA 2002-01	Effect of In-Package Chemistry on the Degradation of Vitrified High-Level Radioactive Waste and Spent Nuclear Fuel Cladding	October 2001
CNWRA 2002-02	Evaluation of Analogs for the Performance Assessment of High-level Waste Container Materials	March 2002

ABSTRACT

One of the key attributes of the overall system performance in the U.S. Department of Energy Repository Safety Strategy for the proposed repository at Yucca Mountain, Nevada, is the estimated long life of waste packages as the main engineered barrier to radionuclide release. The anticipated long life of the waste packages is primarily derived from the slow rate of dissolution of Alloy 22 (Ni-22Cr-13Mo-3W-3Fe) containers in aqueous environments (a dissolution behavior termed passive dissolution). The corrosion rate of Alloy 22 under passive conditions is so slow (approximately hundreds of nanometers per year) that the waste package wall is estimated to take tens of thousands of years to be corroded through, in the absence of conditions leading to localized corrosion or stress corrosion cracking. Although a significant number of studies have been performed to define the critical conditions determining the transition between passive and localized corrosion, no studies have addressed the validity of extrapolating passive dissolution behavior for extended periods. This report is a preliminary effort to fill that gap by clearly outlining long-term extrapolation assumptions and discussing those assumptions that may not be valid for extended periods, as well as the potential influence on total system performance assessments. The composition of the oxide film is discussed based on thermodynamic data available in the literature. A brief review of oxide film-growth models is presented, highlighting common trends in the derivation of growth laws. Gravimetric and electrochemical methods for the measurement of corrosion rates are discussed, presenting strengths and limitations of each method, as well as potential sources of error. The corrosion rate of Alloy 22, measured as a function of time and temperature using electrochemical methods, is reported. An apparent activation energy is estimated to account for the temperature dependence of the corrosion rate. A model for the anodic passive dissolution of Alloy 22 is proposed and consequences of the model to long-term extrapolation are discussed. Alternative mechanisms with the possibility of causing enhanced dissolution rates are briefly analyzed. Additional work is proposed to address some of the model assumptions, to validate or refute model predictions, or to provide additional data for model refinement.

CONTENTS

CONTENTS (continued)

FIGURES

TABLES

ACKNOWLEDGMENTS

This report was prepared to document work performed by the Center for Nuclear Waste Regulatory Analyses (CNWRA) for the U.S. Nuclear Regulatory Commission (NRC) under Contract No. NRC–02–02–012. The activities reported here were performed on behalf of the NRC Office of Nuclear Material Safety and Safeguards, Division of Waste Management. The report is an independent product of CNWRA and does not necessarily reflect the views or regulatory position of the NRC.

The authors thank J. Gonzalez and A. Ramos for their assistance in preparing this report. The authors also acknowledge Drs. N. Sridhar and C.S. Brossia for their technical reviews, Dr. B. Sagar for his programmatic review, and C. Cudd, B. Long, and A. Woods for their editorial reviews.

QUALITY OF DATA: Sources of data are referenced in each chapter. CNWRA-generated data contained in this report meet quality assurance requirements described in the CNWRA quality assurance manual. Data from other sources, however, are freely used. The respective sources of non-CNWRA data should be consulted for determining levels of quality assurance. Experimental data have been recorded in CNWRA scientific notebook numbers 366, 485, and 520.

ANALYSES AND CODES: Mathematica Version 4.1 (Wolfram Research, Inc., 1999) and the OLI Systems Corrosion Analyzer Software Version 6.5 (OLI Systems, Inc., 2001) were used for analyses contained in this report. Mathematica Version 4.1 is a commercial software for general mathematical analyses and the OLI Systems Corrosion Analyzer Software is a thermodynamic speciation and process simulation software. The Corrosion Analyzer Software Version 6.5 is controlled under the CNWRA Technical Operating Procedure (TOP–018) (Development and Control of Scientific and Engineering Software). Mathematica is not under TOP–18 control. Procedures developed in Mathematica Version 4.1 were constructed to perform statistical analyses and calculations associated with Alloy 22 passive dissolution modeling. Details concerning these procedures can be found in CNWRA scientific notebook numbers 304 and 534.

REFERENCES

OLI Systems, Inc. "Corrosion Analyzer Software." Version 6.5. Morris Plains, New Jersey: OLI Systems, Inc. 2001.

Wolfram Research, Inc. *The Mathematica Book.* 4th Edition. Champaign, Illinois: Wolfram Media and Cambridge University Press. 1999.

EXECUTIVE SUMMARY

One of the key attributes of the overall system performance in the U.S. Department of Energy Repository Safety Strategy for the proposed repository at Yucca Mountain, Nevada, is the estimated long life of waste packages as the main engineered barrier to radionuclide release. The estimated long life of the outer container is predicated on the excellent resistance of Alloy 22 (Ni-22Cr-13Mo-3W-3Fe) to various modes of aqueous corrosion for broad ranges of temperature, pH, and concentrations of anionic and oxidizing species. For conditions where localized corrosion cannot occur, Alloy 22 is expected to corrode uniformly in aqueous environments at a slow rate, a dissolution behavior termed passive dissolution. The corrosion rate of Alloy 22 under passive conditions, in the aqueous environments that could contact the waste packages, is so slow (only hundreds of nanometers per year) that a 2-cm [0.79-in] thick container of Alloy 22 is estimated to take tens of thousands of years to be corroded through. A central objective of this report is to analyze the validity of the assumptions supporting these estimates.

The composition of the oxide controlling the passive dissolution of Alloy 22 is discussed based on thermodynamic data and surface analysis results reported in the literature. It is concluded that the oxide is most likely composed of Cr_2O_3, although $Ni[OH]_2$ and $NiMoO_4$ are also thermodynamically stable phases for a range of conditions. According to recent reports in the literature, the overall oxide is of a bilayered structure with chromium-nickel and nickel-molybdenum rich phases. Chromium oxide is believed the predominant contributor to the passivity of Alloy 22.

Models for oxide growth are briefly reviewed, focusing on discriminating criteria to determine the growth law applicable to a particular system. Currently, no models are available that can be used confidently to evaluate long-term passive dissolution, mainly because the problem of extrapolating passive dissolution behavior to extremely long times is of little importance to most industrial applications, compared with the analysis of factors determining passivity and passivity breakdown.

Traditional methods to measure corrosion rates are reviewed, such as weight loss and electrochemical methods, based on measurements of anodic passive current density, polarization resistance, and electrochemical impedance. The basis of the methods, as well as strengths, limitations, and sources of error, are discussed. Weight loss measurements are appropriate for systems where loss of metal can be accurately determined in a short period. For passive metals with low corrosion rates, short-term tests have large measurement uncertainty. In addition, confounding effects, such as the formation of oxide films and the accumulation of corrosion products and deposits, introduce additional uncertainty in the corrosion rate measurements. Electrochemical methods have, in general, higher resolution than gravimetric methods and allow monitoring of the corrosion rate in a nearly continuous manner. Electrochemical methods measure the current flow caused by various simultaneous oxidation and reduction reactions, and only some reactions are related to the dissolution of the metal. Therefore, accurate measurement of dissolution rate requires separation of the contributing electrochemical reactions to the corrosion rate. Another disadvantage of the electrochemical methods is the need for extensive instrumentation which present difficulties for long-term monitoring. Ideally, a multiplicity of techniques, including electrochemical methods, is necessary to determine corrosion rates.

Passive corrosion rates of Alloy 22, determined by potentiostatic anodic passive current density and polarization resistance methods, are reported. There is significant uncertainty in the corrosion rate determined by the polarization resistance method. Also, the selection of the scan rate has an influence on the apparent polarization resistance and derived corrosion rate. The scan rate must be selected to minimize capacitive effects. At 95 °C [203 °F], a reasonable upper bound for the corrosion rate is 5×10^{-4} mm/yr [2×10^{-5} in/yr]. Passive corrosion rates were found to be independent of the composition of the solution, but are dependent on the temperature. From median values of the potentiostatic anodic passive current density data it is verified that the dependence of the current density on the temperature is of Arrhenius form, with a mean apparent activation energy of 44.7 kJ mol^{-1} [10.7 kcal mol^{-1}] and a standard deviation of 5.5 kJ mol^{-1} [1.3 kcal mol^{-1}].

A model for the passive dissolution of nickel-chromium-molybdenum alloys (of which Alloy 22 is a particular example), based on the Point Defect Model, was developed. The Point Defect Model has been formulated to develop a mechanistic understanding of passivity and passivity breakdown of metals in low temperature aqueous systems. From the model and thermodynamic data, it is hypothesized that the predominant species transporting charge through the oxide film are cation interstitials. Dissolution of the alloy in the form of interstitials creates vacancies in the alloy. Vacancy creation resulting from metal oxidation has been noted in high-temperature nickel-chromium systems. The model predicts that if vacancies are created in the alloy and accumulate at the metal-film interface, the passive current density should decrease as a function of time. This observation is consistent with experimental data. The passive current density decreased steadily in 2-week experiments under potentiostatic control at 95 °C [203 °F] in various solutions. Adequate goodness of fit is obtained between experimental data and simulated current densities for particular selections of rate constants and finite difference parameters. It is thus concluded that the experimental data are consistent with the hypotheses of predominant interstitial cation conduction and vacancy injection at the metal-film interface. It is proposed that steady state in the anodic current density occurs after reaching a saturation value of the vacancy concentration at the metal-film interface. It is acknowledged that the proposed model for the passive dissolution of the alloy ceases to be valid after reaching the vacancy saturation concentration.

The model is used to address the question of whether or not dissolution is stoichiometric. It is argued that dissolution can be initially nonstoichiometric, but in the long term, it evolves toward stoichiometry, which is consistent with observations reported in the literature for similar alloy systems. The conclusion of congruent or stoichiometric dissolution depends on the assumption that diffusion coefficients for the atoms of the alloying elements are similar, an assumption consistent with the literature of solid-state diffusion.

The main implication of the hypothesis of vacancy injection is the possible long-term instability of the oxide film. References are provided to support this view. It is not anticipated that periodic spalling of the film will significantly accelerate the penetration rate of the corrosion front because a protective chromium oxide could form again in case of spalling. It is envisioned, however, that the main consequence of the possible long-term instability of the oxide film is the evolution of the surface into a rough morphology. In performance assessments, the effect of spalling is presumably within the uncertainty of the computed time to failure due to the passive dissolution of the container. Otherwise, it is recommended, from engineering judgement, to introduce a factor in the range of 0.5 to 0.7 to adjust the failure time computed in total system performance assessments.

Other alternatives and interpretations that could also be consistent with the electrochemical data are considered and discussed. Possibilities leading to enhanced alloy dissolution rates are discussed, such as transpassive dissolution and anodic sulfur segregation. It is argued that transpassive dissolution is unlikely to occur because of the significant concentration of oxidizing species in the solution that is necessary to cause the corrosion potential to exceed a critical potential for transpassivity. Additional analyses are necessary to support this view. According to the literature, sulfur-enhanced dissolution promoted by anodic sulfur segregation affects predominantly the dissolution of nickel in nickel-chromium alloys. In alloys containing chromium, it appears that the stability of Cr_2O_3 precludes the dissolution rate enhancement caused by anodic segregation of sulfur. Because the model indicates preferential dissolution of one alloy component during extended periods (assuming diffusion coefficients of the atoms of the elements of the alloy are similar) is not possible, it is concluded that preferential dissolution of nickel via sulfur-enhanced dissolution cannot be sustained for extended periods.

Additional work is proposed to address some of the model assumptions, to validate or refute model predictions, or to provide additional data for model refinement.

In summary, the corrosion rate of Alloy 22 at 95 °C [203 °F] is approximately 5×10^{-4} mm/yr [2×10^{-5} in/yr] and it decreases exponentially with decreasing temperature. The effect of film spalling is presumably within the uncertainty in the failure time computed by current total system performance assessments. No credible scenario has been envisioned by which catastrophic failure may occur as a result of passive dissolution in the 10,000-year regulatory compliance period.

1 INTRODUCTION

One of the key attributes of the overall system performance in the U.S. Department of Energy (DOE) Repository Safety Strategy for the proposed repository at Yucca Mountain, Nevada, is the estimated long life of waste packages as the main engineered barrier to radionuclide release (CRWMS M&O, 2000). According to the reference design, the waste package will be composed of two concentric cylindrical containers placed horizontally in a drift. The outer container will be made of a corrosion-resistant alloy, Alloy 22 (Ni-22Cr-13Mo-3W-3Fe); whereas, the inner container will be made of Type 316 nuclear grade stainless steel intended to provide structural strength to the waste package. The estimated long life of the outer container is dictated by the resistance of Alloy 22 to various modes of aqueous corrosion throughout broad ranges of temperature, pH, and concentrations of anionic and oxidizing species. In an aqueous environment, assumed to be established when the relative humidity achieves a critical value, and in the absence of conditions leading to localized corrosion, Alloy 22 will dissolve under passive conditions. The slow, passive dissolution rate (approximately hundreds of nanometers per year) is estimated to corrode through a 2-cm [0.79-in] thick container in tens of thousands of years. Because of the extremely low passive dissolution rate of Alloy 22 and its high resistance to various modes of accelerated corrosion, the performance of the waste package is postulated as one of the principal factors in the DOE postclosure safety case (CRWMS M&O, 2000). The issue of long-term passive behavior of Alloy 22 as a container materials has been the subject of a recent international workshop with the participation of many corrosion experts (Sagüés and DiBella, 2001).

1.1 Objective

This report is consistent with review methods described in the Yucca Mountain Review Plan—Draft Report for Comment (NRC, 2002) concerning data uncertainty, model uncertainty, and model support for the degradation of engineered barriers. The principal purpose of the Yucca Mountain Review Plan is to ensure the quality, uniformity, and consistency of U.S. Nuclear Regulatory Commission (NRC) staff reviews of any license application and any amendments. The objective of this report is to provide some basis to evaluate if models used by the DOE are not likely to underestimate the actual degradation and failure of engineered barriers as a result of corrosion or other degradation processes. Proposing a model for the degradation process known as passive dissolution is an attempt to envision potential mechanisms that could possibly affect long-term estimates of the degradation of waste package materials.

1.2 Scope and Content of the Report

The low passive dissolution rate of Alloy 22 depends on the existence and stability of a passive oxide film. Although a significant number of studies have been made to define the critical conditions that determine the transition between passive and localized corrosion, no studies have addressed the validity of extrapolating passive dissolution behavior for extended periods. This report is intended to partially fill that gap, by clearly outlining long-term extrapolation assumptions and discussing assumptions that may not be valid over extended periods as well as their potential influence on total system performance analyses.

A model, based on the Point Defect Model, was developed to study the low-temperature passive dissolution of nickel-chromium-molybdenum alloys. From the model, it is suggested that vacancies are created or injected into the alloy as a result of the passive dissolution process. The injection of vacancies in metals that dissolve because of the transport of cations through the oxide film is a well-established phenomenon in high-temperature systems, including nickel-chromium alloys, and it has been used to account for the formation of voids, constant volume oxidation, and oxide detachment, among other phenomena (Gibbs and Hales, 1977). Although reports on the injection of vacancies in low-temperature systems are limited (e.g., Berghezan, et al., 1961; Dobson and Smallman, 1966), it is considered to be a feasible phenomenon for Alloy 22, which could lead to the instability of the oxide layer over extended periods. In this report, the possible accumulation of vacancies at the metal-film interface is used to explain the decrease in time, in 2-week experiments, of the passive current density. The potential instability of the oxide over extended periods and the stochastic nature of the kinetic phenomena are suggested to result in the evolution of the surface into a rough morphology. The front-most points of the corrosion front will penetrate earlier the alloy thickness than the "average" corrosion front. However, the effect of oxide spalling and surface roughening on the time to failure is presumably within the uncertainty in the failure time computed by current total system performance assessments.

This report is structured as follows. In Chapter 2, the composition of the passive oxide film is discussed from a thermodynamic viewpoint, using information available in the literature for nickel-chromium alloys and Alloy 22. Models of passive film growth available in the literature are also discussed. In Chapter 3, gravimetric and electrochemical methods for the measurement of corrosion rates are discussed, outlining the basis of the different methods and computation of corrosion rates from particular test parameters. A discussion of standard methods and recommended practices is included, as well as sources of error for the various methods for the determination of corrosion rates. Chapter 3 contains a presentation of the common method to compute times to failure of an alloy slab of a defined thickness under passive dissolution, and the assumptions for long-term extrapolation of the passive dissolution behavior. In Chapter 4, electrochemical measurements of Alloy 22 corrosion rate are reported, including potentiostatic polarization and polarization resistance. Chapter 4 concludes with computations of the apparent activation energy to estimate the dependence of the passive dissolution rate on the temperature. The model for the passive dissolution of nickel-chromium-molybdenum alloys (of which Alloy 22 is a particular example) is developed in Chapter 5. This chapter includes a discussion of the finite difference implementation of the model and model results, as well as a discussion on implications of the model to long-term extrapolation of the passive dissolution behavior. Chapter 5 concludes with a discussion of alternatives to explain the experimental data and other feasible mechanisms that could yield higher alloy dissolution rates. In Chapter 6, the main findings of the report are summarized, as well as proposed future work. References are listed in Chapter 7. Two appendices are included to provide additional details on the interstitial conduction assumption and the implementation of the finite difference equations of the passive dissolution model.

1.3 Yucca Mountain Review Plan Acceptance Criteria

The Yucca Mountain Review Plan—Draft Report for Comment (NRC, 2002) provides guidance to evaluate any license application for a proposed repository at Yucca Mountain. The licensing criteria are in 10 CFR Part 63. The U.S. Secretary of Energy recommended the Yucca

Mountain site to the President of the United States for the development of a nuclear waste repository. The President notified Congress that he considers Yucca Mountain qualified for a construction permit application, and Congress approved the recommendation (after overriding a veto by the State of Nevada). DOE is expected to submit a license application to NRC. The principal purpose of the Yucca Mountain Review Plan is to ensure the quality, uniformity, and consistency of NRC staff reviews of any license application and any amendments. The Yucca Mountain Review Plan—Draft Report for Comment (NRC, 2002) has separate sections for reviews of repository safety before permanent closure, repository safety after permanent closure, the research and development program to resolve safety questions, the performance confirmation program, and administrative and programmatic requirements. Each of these sections supports determining compliance with specific regulatory requirements from 10 CFR Part 63. Particular acceptance criteria in the draft Yucca Mountain Review Plan relevant to this report are the following:

Acceptance Criterion 3

Data Uncertainty Is Characterized and Propagated through the Model Abstraction

- Models use parameter values, assumed ranges, probability distributions, and/or bounding assumptions that are technically defensible and reasonably account for uncertainties and variabilities

- For those degradation processes that are significant to the performance of the engineered barriers, DOE provides appropriate parameters, based on techniques that may include laboratory experiments, field measurements industrial analogs, and process-level modeling studies conducted under conditions relevant to the range of environmental conditions within the waste package emplacement drifts. DOE also demonstrates the capability to predict the degradation of the engineered barriers in laboratory and field tests

- For the selection of parameters used in conceptual and process-level models of engineered barrier degradation that can be expected under repository conditions, the assumed range of values and probability distributions is not likely to underestimate the actual degradation and failure of engineered barriers as a result of corrosion.

Acceptance Criterion 4

Model Uncertainty Is Characterized and Propagated Through the Model Abstraction

- Alternative modeling approaches of features, events, and processes are considered and consistent with available data and current scientific understanding, and the results and limitations are appropriately considered in the abstraction.

- Conceptual model uncertainties are defined and documented, and conclusions regarding performance of the engineered barriers are properly assessed.

- DOE uses alternative modeling approaches consistent with available data and current scientific understanding and evaluates the model results and limitations using tests and analyses that are sensitive to the processes modeled. For example, for processes such as uniform corrosion, localized corrosion, and stress-corrosion cracking of the engineered barriers, DOE considers alternative modeling approaches to develop its understanding of environmental conditions and material factors significant to these degradation processes.

Acceptance Criterion 5

Model Abstraction Output Is Supported by Objective Comparisons

- Models implemented in the total system performance assessment abstraction provide results consistent with output from detailed process-level models and/or empirical observations (laboratory and field testings and/or natural analogs).
- Numerical corrosion models used to calculate the lifetimes of the engineered barriers are adequate representations considering the associated uncertainties in the expected long-term behaviors, the range of conditions (including residual stresses), and the variability in engineered barrier fabrication processes (including welding).
- Evidence is sufficient to show that models used to evaluate performance are not likely to underestimate the actual degradation and failure of engineered barriers as a result of corrosion or other degradation processes.
- Mathematical models for the degradation of engineered barriers are based on the same environmental parameters, material factors, assumptions, and approximations shown to be appropriate for closely analogous engineering or industrial applications and experimental investigations.
- Accepted and well-documented procedures are used to construct and test the numerical models that simulate the engineered barrier chemical environment and degradation of engineered barriers.
- Sensitivity analyses or bounding analyses are provided to support the abstraction of degradation of engineered barriers that cover ranges consistent with the site data, field or laboratory experiments and tests, and industrial analogs.

1.4 DOE and NRC Agreements Related to this Report

The NRC staff have, for many years, engaged in extensive interactions with DOE and various stakeholders including the State of Nevada, Native Americans, affected units of local government, representatives of the nuclear industry, and interested members of the public. In recent years, the interactions focused on what NRC staff termed key technical issues. The intent of the key technical issues is to focus prelicensing work on those topics most critical to the postclosure performance of the proposed geological repository. To address and document the key technical issues, the NRC staff initiated a formal issue resolution process that includes reviewing DOE documents; conducting independent analyses, experiments, and field work; interacting with DOE in public technical meetings; and identifying the information that DOE will need to provide in any potential license application. This report is mainly focused on the Container Life and Source Term Key Technical Issue. A list of DOE and NRC agreements (Table 1-1) on the Container Life and Source Term and Total System Performance Assessment and Integration Key Technical Issue derived during technical exchange and management meetings related to this report is included in this section.

Table 1-1. DOE and NRC Agreements Related to this Report	
Agreement	**DOE and NRC Agreement**
CLST.1.02	Provide the documentation for the path forward items listed on slide 12. (Surface elemental analysis of alloy test specimens is necessary for determination of selective dissolution; surface analysis of welded specimens for evidence of dealloying; continue testing including simulated saturated repository environment to confirm enhancement factor). DOE will provide the documentation in a revision to the Analysis Model Report General and Localized Corrosion of Waste Package Outer Barrier by license application.
CLST.1.03	Provide documentation that confirms the linear polarization resistance measurements with corrosion rate measurements using other techniques. DOE will provide the documentation in a revision to the General and Localized Corrosion of Waste Package Outer Barrier Analysis and Model Report by license application.
CLST.1.06	Provide the documentation on testing showing corrosion rates in the absence of silica deposition. DOE will document the results of testing in the absence of silica deposits in the revision of Alloy 22 Analysis and Model Report (ANL–EBS–MD–000003) prior to license application.
CLST.1.07	Provide the documentation for the alternative methods to measure the corrosion rate of the waste package material (e.g., ASTM G–102 Testing) or provide justification for the current approach. DOE will document the alternative methods of corrosion measurement in the revision of Alloy 22 Analysis and Model Report (ANL–EBS–MD–000003), prior to license application.
CLST.1.08	Provide the documentation for Alloy 22 and titanium for the path forward items listed on slides 16 and 17. (Calculate potential-pH diagrams for multicomponent Alloy 22; grow oxide films at higher temperatures in autoclaves, in air and/or electrochemically to accelerate film growth for compositional and structural studies below; resolve kinetics of film growth: parabolic or higher order, if film growth becomes linear, and if, as film grows, it becomes mechanically brittle and spalls off; determine chemical, structural, and mechanical properties of films, including thicken films; correlate changes in E_{corr} measured in long-term corrosion test facility with compositional changes in passive film over time; perform analyses on cold-worked materials to determine changes in film structural properties; perform examination of films formed on naturally occurring Josephinite; compare films formed on Alloy 22 with other similar passive film alloys with longer industrial experience). DOE will provide the documentation in the revision to analysis and model reports (ANL–EBS–MD–000003 and ANL–EBS–MD–000004) prior to license application.
CLST.1.09	Provide the data that characterize the passive film stability, including the welded and thermally aged specimens. DOE will provide the documentation in a revision to Analysis and Model Reports (ANL–EBS–MD–000003 and ANL–EBS–MD–000004) prior to license application.

Table 1-1. DOE and NRC Agreements Related to this Report (continued)

Agreement	DOE and NRC Agreement
CLST.1.10	Provide the documentation for Alloy 22 and titanium for the path forward items listed on slides 21 and 22. (Measure corrosion potentials in the long-term corrosion test facility to determine any shift of potential with time toward the critical potentials for localized corrosion; determine critical potentials on welded and welded and aged coupons of Alloy 22 versus those for base metal—particularly important if precipitation or severe segregation of alloying elements occurs in the welds; separate effects of ionic mix of specimens in Yucca Mountain waters on critical potentials—damaging species from potentially beneficial species; determine critical potentials in environments containing heavy metal concentrations.) DOE will provide the documentation in a revision to Analysis and Model Reports (ANL–EBS–MD–000003 and ANL–EBS–MD–000004) prior to license application.
TSPAI.3.01	Propagate significant sources of uncertainty into projections of waste package and drip shield performance included in future performance assessments. Specific sources of uncertainty that should be propagated (or strong technical basis provided as to why it is insignificant) include (i) the uncertainty from measured crevice and weight-loss samples, general corrosion rates, and the statistical differences between the populations; (ii) the uncertainty from alternative explanations for the decrease in corrosion rates with time (i.e., silica coatings that alter the reactive surface area); (iii) the uncertainty from utilizing a limited number of samples to define the correction for silica precipitation; (iv) the confidence in the upper limit of corrosion rates resulting from the limited sample size; and (v) the uncertainty from alternative statistical representations of the population of empirical general corrosion rates. The technical basis for sources of uncertainty will be established on completion of existing agreement items CLST 1.4, 1.5, 1.6, and 1.7. DOE will then propagate significant sources of uncertainty into projections of waste package and drip shield performance included in future performance assessments. This technical basis will be documented in a future revision of the General and Localized Corrosion of Waste Package Outer Barrier Analysis and Model Report (ANL–EBS–MD–000003) expected to be available consistent with the scope and schedules for the specified Container Life and Source Term Agreements. The results of the Analysis and Model Report analyses will be propagated into future total system performance assessment analyses for any potential license application.
TSPAI.3.04	Provide the technical basis that the representation of the variation of general corrosion rates (if a significant portion is lack of knowledge uncertainty) does not result in risk dilution of projected dose responses (ENG1.3.3). DOE will provide the technical basis that the representation of the variation of general corrosion rates results in reasonably conservative projected dose rates. The technical basis will be documented in an update to the WAPDEG Analysis of Waste Package and Drip Shield Degradation Analysis and Model Report (ANL–EBS–PA–000001). This analysis and model report is expected to be available to NRC in fiscal year 2003. These results will be incorporated into future total system performance assessment documentation for any potential license application.

2 COMPOSITION OF THE PASSIVE FILM AND MODELS OF FILM GROWTH

In this chapter, the composition of the oxide film on Alloy 22 is discussed based on thermodynamics and information reported in the literature. Chromium oxide is the phase with the most predominant stability domain. Models for film growth on metals developing protective oxides are briefly reviewed, as well as common ideas employed in the development of film growth rate laws. It is noted that similar film growth rates can be consistent with dissimilar mechanisms of film formation, making difficult the identification of the prevailing mechanisms based only on measurements of film thickness and current density transients.

2.1 Thermodynamics and Experimental Composition

The slow dissolution rate of Alloy 22 depends on the existence and stability of a passive oxide film formed on the metal surface as the product of solid-state electrochemical reactions. The oxide is probably a multilayered structure or one with a gradient in composition, with a chromium-rich oxide film forming next to the metal and external layers containing hydrated nickel and molybdenum oxides. Figure 2-1 shows Pourbaix diagrams of the nickel-chromium-water and chromium-nickel-molybdenum-water systems at 95 °C [203 °F] for 10^{-2} M concentrations of ions in solution. These diagrams provide a thermodynamic framework for the possible structure of the oxide film. Caution should be exercised in using thermodynamic potential-pH diagrams because (i) the activities of solid phases (nickel, chromium, and molybdenum) in solid solution are not equal to unity as assumed in these thermodynamic calculations, (ii) bulk oxide and thin film oxide thermodynamic properties may be significantly different (MacDougall and Graham, 1995), and (iii) passive films for these alloys are seldom equilibrium structures. The diagrams in Figure 2-1 were computed using the OLI Systems Corrosion Analyzer Software (OLI Systems, Inc., 2001), which is a thermodynamic speciation and process simulation software. The pH of the aqueous solution was adjusted either by HCl in the acidic regime or NaOH in the alkaline regime. The formation of chloride complexes is a result of HCl used as a titrant in the acidic regime. Note that chloride is one of the prevailing anionic species in the groundwater and can be concentrated on a metal surface by physical and electrochemical processes. To be noted in Figure 2-1 is the predominant domain of the Cr_2O_3 [Figures 2-1(a) and (b)] and $NiMoO_4$ [Figure 2-1(b)] solid phases in the potential-pH space. Other possible solid phases are hydrated nickel oxide [$Ni(OH)_2$] and MoO_2. However, these calculations only facilitate the identification of thermodynamically stable phases, but they do not definitely determine the phases that actually form. The phases composing the oxide layer are also functions of the kinetics and the interfacial properties controlling the rates of the heterogeneous reactions.

It is a natural trend for metals to continuously evolve toward the ore state (Sridhar and Cragnolino, 2002). The initial formation of an oxide film on the surface of the alloy causes the physical separation of the metal from the environment. The interfacial oxide controls the rate of dissolution of the metal (or the rate of transformation of the metal into the ore state), and this rate is slow for passive metals. Although the final ore is in a thermodynamically stable state, the composition of the interface oxide is determined not by thermodynamics but by the kinetics of the electrochemical reactions. For example, kinetic rates could determine the presence of a phase in a potential-pH region where such phase is not thermodynamically stable (in this case the phase is denoted as metastable). For instance, in the stability region of Cr^{2+} in Figure 2-1(a) (acidic pH and potential between −1.0 and −0.4 V_{SHE}), both Cr_2O_3 and chromium dissolve into Cr^{2+} in the presence of water. Besides directly dissolving into Cr^{2+}, chromium also could combine with water to form Cr_2O_3. Thus, in acidic pH and reducing conditions, kinetic processes exist that lead to the formation and dissolution of Cr_2O_3. If the rate of Cr_2O_3 formation is greater than or equal to the rate of oxide dissolution, Cr_2O_3 can exist as a metastable phase in the stability region of Cr^{2+}; otherwise, Cr_2O_3 dissolves. Therefore, thermodynamic diagrams do not suffice to explain the existence of the various phases of the oxide film formed on nickel-chromium-molybdenum alloys. Based on the dimension of the stability area of Cr_2O_3 in the potential-pH diagram, however, it could be arguably concluded that this phase predominantly controls the anodic dissolution process. Assuming Cr_2O_3 is the controlling phase, polarization of the system to high anodic potentials within the stability region for water, causes the transformation of Cr_2O_3 into Cr(VI) species in solution according to Figure 2-1, giving rise to the transpassive dissolution experimentally observed in Alloy 22 in acidic electrolyte (Brossia, et al., 2001).

Evidence obtained by surface analysis techniques, such as Auger electron spectroscopy and low energy ion scattering spectroscopy, and x-ray photoelectron spectroscopy indicates the film that forms in the passive range (below the potential for transpassive dissolution) on nickel-chromium alloys is mainly composed of chromium oxide and nickel oxyhydroxide (Boudin, et al., 1994; Lorang, et al., 1990). For nickel-chromium alloys of high chromium content, the film is composed primarily of Cr_2O_3 (Boudin, et al., 1994). In independent studies, a critical alloy composition was identified (~15 wt% chromium), above which the anodic behavior of nickel-chromium alloys changes markedly (Tikkanen and Hyvärinen, 1969; Bond and Uhlig, 1970). In view of the study by Boudin, et al. (1994), it can be argued that such a change in the anodic behavior is caused by a conversion in the predominant composition of the film from nickel oxide to chromium oxide, as the chromium content in the alloy increases. Recent studies, at the University of Western Ontario, General Electric's Corporate Research and Development Center, and the Lawrence Livermore National Laboratory, of Alloy 22 using techniques such as time of flight, secondary ion mass spectrometry, and x-ray photoelectron spectroscopy, have corroborated the formation of a bilayered oxide, with an inner chromium-nickel-rich oxide layer and an outer nickel-molybdenum-rich layer in 1 M NaCl + 0.1 M H_2SO_4 (pH = 1) (Waste Package Materials Performance Peer Review Panel, 2002). Table 2-1 summarizes x-ray photoelectron spectroscopy results of the composition of the passive film and film thickness as functions of the voltage as reported in Waste Package Materials Performance Peer Review Panel (2002).

Table 2-1. Composition of the Passive Film on Alloy 22 as a Function of the Potential in 1 M NaCl + 0.1 M H_2SO_4 (Waste Package Materials Performance Peer Review Panel, 2002).

Potential	Thickness	Average Composition		
Air formed	18Å	29% Cr_2O_3	60% NiO	11% MoO_3
200 mV	20Å	43% Cr_2O_3	47% NiO	10% MoO_3
500 mV	23Å	56% Cr_2O_3	32% NiO	12% MoO_3
700 mV	28Å	63% Cr_2O_3	25% NiO	12% MoO_3

Waste Package Materials Performance Peer Review Panel. "Final Report Waste Package Materials Performance Peer Review Panel." Las Vegas, Nevada: DOE. 2002.

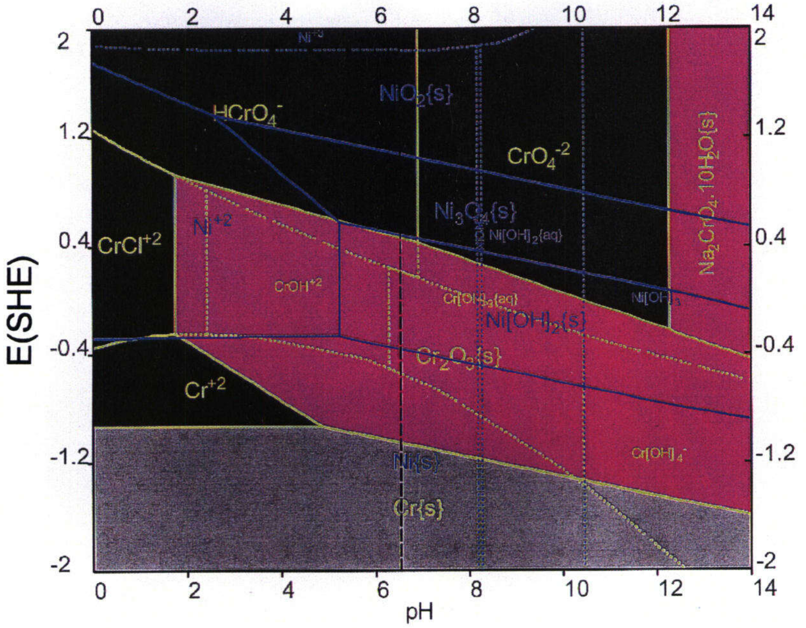

(a)

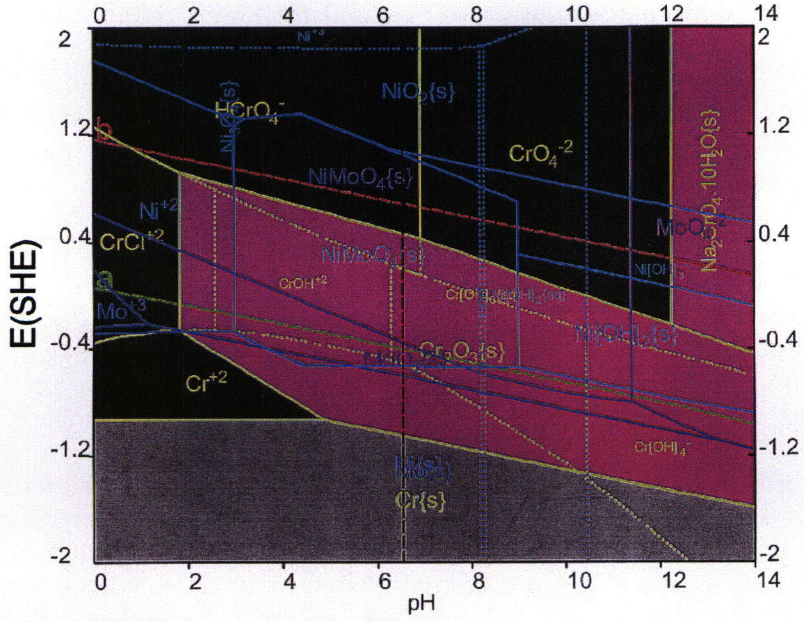

(b)

Figure 2-1. Potential-pH Stability Diagrams at 95 °C [203 °F]. (a) Nickel-Chromium-Water System. (b) Nickel-Chromium-Molybdenum-Water System. Ions in Solution Are Assumed at a Concentration of 10^{-2} M.

To be noted in Table 2-1, the thickness and chromium content of the film increase as the applied potential increases. The inner chromium oxide layer is believed to control the passive dissolution process and forms by heterogeneous solid-state electrochemical reactions. The outer oxide is possibly a precipitated layer. Other authors share that general point of view for bilayered oxides (Macdonald, 1992). The thickness of passivating oxides is, in general, proportional to the applied potential (Macdonald, 1992), and this could explain the increase in Cr_2O_3 content in the Alloy 22 oxide layer as a function of the applied potential. For a layer that forms due to dissolution and precipitation, it is expected that its thickness is independent of the applied potential for the following reasons. For the Alloy 22 system, the passive current density is independent of the applied potential over a wide range up to the potential for transpassive dissolution (Dunn, et al., 1999, 2000a). Assuming the dissolution rate of molybdenum is also independent of the applied potential and that MoO_3 is a precipitated oxide (in this case, the homogeneous reactions leading to the formation of MoO_3 are also independent of the applied potential), it is expected the content of MoO_3 in the oxide film should be independent of the applied potential. The fact that the content of MoO_3 in Table 2-1 is roughly independent of the applied potential is consistent with the notion that this oxide is a precipitated product. Nonetheless, the content of MoO_3 in the oxide film is possibly a function of time. To rationalize the apparent inverse dependence of the NiO on the applied potential, it is necessary to know the dependence of the composition of the oxide on the polarization direction. In other words, it is not known if, by reversing the applied potential from 700 mV to 200 mV, the original composition at 200 mV is reproduced. The conjecture is that the Cr_2O_3 content should be reversible with respect to the applied potential, the content of MoO_3 should remain approximately constant or possibly increase as a function of time, and the NiO content may have a stronger dependence on time than on the applied potential. Experimental verification of these suggestions is necessary to propose mechanisms for the origin of the different layers composing the oxide film on Alloy 22.

Continuous metal dissolution, after the formation of a protective oxide film, requires a driving force, such as an electric field, to transport the cations through the film into the solution. The rate of transmission of cations through the film can be correlated to the rate of film growth. In the following section, models for the growth of oxide films are discussed.

2.2 Models for Film Growth

In this section, models for film growth on metals developing protective oxides, as well as common ideas employed in the development of film growth rate laws, are reviewed briefly. It is noted that similar growth rates can be consistent with dissimilar mechanisms of film formation, making the identification of prevailing mechanisms difficult, based only on measurements of film thickness and current density transients. Models of film growth have been used in general to describe the transient growth of oxide films in both aqueous and gas environments. Oxide films are thicker at higher temperatures and could grow to a thickness limited by mechanical stresses in the oxide. At low temperatures, a steady-state thickness is usually reached within minutes after initiation of the oxidation process for metals developing protective oxides (e.g., nickel, iron, and chromium). Common laws of growth rate of the oxide layer are parabolic (the square of the film thickness is proportional to the time), inverse logarithmic (the thickness is inversely proportional to the logarithm of time), and direct logarithmic (the thickness is proportional to the logarithm of the time) (Evans, 1968). An important development in the understanding of mechanisms of film formation, specially at high temperatures, was derived from efforts to explain these growth laws. Proposed explanations of oxide growth laws are still subjects of discussion (Macdonald, et al., 1992; Macdonald and Urquidi-Macdonald, 1990).

To derive a growth rate law, Verwey (1935) assumed the rate of cation transport through the oxide film to be the rate determining step. According to Verwey (1935), in strong electric fields, the rate of drift of the ion through the film, J {mol $\mathrm{cm}^{-2}\,\mathrm{s}^{-1}$ [mol $\mathrm{in}^{-2}\,\mathrm{s}^{-1}$]}, equals

$$J = 4\,c_i\,\nu r e^{-U/kT}\,\sinh\left(\frac{K_1 V}{k\,T\,L}\right) \tag{2-1}$$

where

c_i — interstitial concentration in the oxide, mol/cm^3 [mol/in^3]
ν — jumping frequency, s^{-1}
$2r$ — distance between interstitial positions, cm [in]
U — an activation energy, J [cal]
k — Boltzmann's constant, 1.38×10^{-23} J K^{-1} [3.3×10^{-24} cal K^{-1}]
T — the absolute temperature, K
K_1 — a constant proportional to r and the ionic charge, Coul m [Coul in]
L — the oxide thickness, cm [in]
V — the potential drop across the film, Volt

The derivation by Verwey was revised by Mott (1947) and Cabrera and Mott (1948–1949) by assuming that interface kinetics controlled the rate of the dissolution reaction, as opposed to transport through the film assumed by Verwey. The mathematical form of the equation derived for the rate of ionic transport, J, by Cabrera and Mott is identical to that proposed by Verwey, differing only in factors and their interpretation. The derivation by Cabrera and Mott (1948–1949) is not free of criticism; for example, Evans (1968), hints that the equation by Cabrera and Mott is more appropriate to film transport control than to interfacial kinetics control.

In general, in the derivation of the growth rate models, it is assumed the rate of growth is proportional to the ionic flux through the oxide

$$\frac{\mathrm{d}L}{\mathrm{d}t} = \frac{1}{\Omega}J \tag{2-2}$$

where

Ω — a constant with units of mol/cm^3 [mol/in^3] proportional to the number of moles per unit of volume of the oxide

Using the Verwey (1935) and Cabrera and Mott (1948–1949) equation for the ionic flux through the film, J, the growth rate can be expressed as

$$\frac{\mathrm{d}L}{\mathrm{d}t} = 2\frac{A}{\Omega}\sinh\theta \tag{2-3}$$

where

A — a constant with units of mol cm^{-2} s^{-1} [mol in^{-2} s^{-1}]
θ — $K_1\ V/(kTL)$

Particular models differ in the simplifications made to the right side of Eq. (2-3). For example, in the limit when θ is small (because of a large thickness, L, or small potential drop, V), the growth rate equation becomes

$$\frac{\mathrm{d}L}{\mathrm{d}t} = 2\frac{A}{\Omega}\theta = 2\frac{A}{\Omega}\frac{K_1 V}{kTL} \tag{2-4}$$

which yields a parabolic growth law when integrated

$$L^2 = L_o^{\,2} + K_2\left(t - t_o\right) \tag{2-5}$$

where

L_o — initial thickness, cm [in]
t_o — initial time, s
K_2 — a constant with units of cm^2 s^{-1} [in^2 s^{-1}] that has been shown by Evans (1960) to be equal to $V\kappa\ n_e(n_c + n_a)/(\Omega\ F)$, where κ is the specific conductivity of the oxide, n_e, n_c, and n_a are the transport numbers for electrons, cations, and anions, respectively.

Values of K_2 calculated as a function of κ, n_e, n_c, and n_a compare well with experimental data [tabulated values are included in Evans (1960)], providing strong support for the derivation arguments. The parabolic growth law appears to be obeyed by the growth of multiple oxide films over a range of high temperatures {e.g., 600–800 °C [1,112–1,472 °F] for the oxidation of copper}. Sulfide, iodide, and bromide films also obey the parabolic growth law at lower temperatures (Evans, 1968).

In the limit when θ is large (because of a large electric field or thin film), Eq. (2-3) becomes

$$\frac{\mathrm{d}L}{\mathrm{d}t} = \frac{A}{\Omega}e^{\theta} \tag{2-6}$$

This expression can be integrated, under particular approximations, to yield the inverse logarithmic growth rate expression (Evans, 1968, 1960)

$$\frac{1}{L} = \frac{1}{L_o} - K_4 \ln\left[a(t - t_o) + 1\right] \tag{2-7}$$

where

K_4 — a constant with units of cm^{-1} [in^{-1}]
a — a constant with units of s^{-1}

Cabrera and Mott (1948–1949) also derived a similar equation using different arguments than those by Evans (1968, 1960). Inverse logarithmic growth laws are frequently encountered for low-temperature oxidation (Fehlner, 1986). Multiple examples exist of inverse logarithmic growth, such as aluminum oxidized in air and iron oxidized in air at room temperature, for up to 1 year (Evans, 1968).

Assuming the ejection of cations from the metal causes the creation of vacancies in the metal at the metal-film interface and these vacancies diffuse into the metal, Evans (1960) derived a direct logarithmic growth expression:

$$L = L_o \ln[a(t - t_o) + 1] \tag{2-8}$$

Other growth laws have been proposed, such as cubic, sigmoidal, and multiple-stage. There is no unique law capable of accounting for the observed growth rates at all times and throughout a range of temperatures. In fact, the curvature of the experimental data and the uncertainty in the data do not allow for unequivocal delineation of the prevailing growth law. Growth laws are indistinguishable when compared in short time periods. Methods have been proposed to distinguish between growth rate laws using electrochemical techniques for metals exposed to aqueous environments. Because the rate of injection of cations into the oxide, J, is accompanied by an equivalent production of electrons, invoking Faraday's law allows converting J into a current density. Burstein and Davenport (1989) derived an expression on the basis of the transient current density to distinguish between inverse logarithmic and direct logarithmic growth laws. Interestingly, by assuming an inverse logarithmic growth law, Burstein and Davenport (1989) derived a direct logarithmic growth law, pointing at possible inconsistencies in the approximations used to derive the inverse logarithmic growth law. Burstein and Davenport (1989) proposed that direct logarithmic and inverse logarithmic laws can be differentiated by the analysis of the equation

$$\ln \frac{I}{I_o} = K_4 (I \times t)^{-1/2} \tag{2-9}$$

where

I — current density, A cm^{-2} [A in^{-2}]
I_o — a constant with units of A cm^{-2} [A in^{-2}]
K_4 — a constant with units of $\text{Coul}^{1/2}\ \text{cm}^{-1}$ [$\text{Coul}^{1/2}\ \text{in}^{-1}$]

For inverse logarithmic systems, a plot of $\ln I$ versus $(I \times t)^{-1/2}$ yields a straight line with a finite slope. For direct logarithmic systems, the product $I \times t$ is a constant, and thus, the suggested graphical representation would yield a vertical line parallel to the $\ln(I)$ axis. Burstein and Davenport (1989) were partially successful in testing their approach. Important deviations for the considered systems from the predicted linearity were observed, which were explained based on high ohmic potential drops in the electrolyte. Equation (2-9) was evaluated with current density versus time data reported in Chapter 4, and it was concluded that Eq. (2-9) is sensitive to the way the current density versus time data are made smooth. Also, important deviations from linearity were observed, just as Burstein and Davenport (1989) noted in their original paper.

Another model requiring special examination is the Point Defect Model (Macdonald, 1992) because it is being used by U.S. Department of Energy in the theoretical studies of the Alloy 22 anodic oxidation. In the Point Defect Model, it is assumed that the rate determining step is kinetic control at the metal-film and film-solution interfaces. It is assumed that transport through the film is fast enough and does not affect the rate of the oxidation process. It is further assumed that, under potentiostatic control, the potential drops at the metal-film interface, film and film-solution interface respond instantaneously to changes in the film thickness. This assumption makes the potential drop at the metal-film interface to be proportional to the thickness of the film and to the total applied potential at all times. The rate constants of the fundamental heterogeneous charge transfer reactions at the metal-film interface are assumed to be functions of the local potential drop at the metal-film interface. The functional relationship between the local potential drop and the rate constant is postulated to be exponential. The derived differential form of the rate growth law is (Macdonald, et al., 2001)

$$\frac{dL}{dt} = a e^{-bL} - c \tag{2-10}$$

where

a — a constant exponentially related to the applied potential, cm s^{-1} [in s^{-1}]
b — a constant proportional to the magnitude of the electric field, cm^{-1} [in^{-1}]
c — a constant equal to the rate of film dissolution at the metal-film interface, cm s^{-1} [in s^{-1}]

Integration of Eq. (2-10) yields

$$L = L_o + \frac{1}{b}\ln\left(\frac{c - a e^{-bL_o}}{c - a e^{-bL}}\right) - c(t - t_o) \tag{2-11}$$

defining L implicitly as a function of t. Macdonald, et al. (2001) derived an explicit approximated expression for L as a function of time

$$L = L_o + \frac{1}{b}\ln\left[1 + \frac{a}{c} e^{-bL_o}\left(e^{bc(t-t_o)} - 1\right)\right] - c\,(t - t_o) \tag{2-12}$$

From this film growth expression, the direct logarithmic growth rate is produced in the limit when the rate of film dissolution, *c*, is sufficiently small. Equation (2-12) is presumably of wider validity for systems with interfacial control, although it also depends on a number of approximations limiting its validity.

In the absence of film dissolution at the film-solution interface, Zhang, et al. (1998) derived an expression to evaluate whether the High-Field Model assumptions of Cabrera and Mott or the Point Defect Model assumptions are more appropriate for the description of the growth of anodic oxide films on zirconium, tungsten, and tantalum under potentiostatic conditions in phosphate buffer solution. Zhang, et al. (1998) argued that if the High-Field Model prevails, the following relationship for the current holds

$$\sqrt{-\frac{I'}{I(I - I_{ss})}} = B\,V^{-1/2} \ln\left(\frac{I}{A}\right) \tag{2-13}$$

where

I — current density, A cm^{-2} [A in^{-2}]
I' — time-derivative of the current density, A cm^{-2} s^{-1} [A in^{-2} s^{-1}]
I_{ss} — steady-state limit for the current density, A cm^{-2} [A in^{-2}]
A — a constant with units of A cm^{-2} [A in^{-2}]
B — a constant with units of cm Coul$^{-1/2}$ [in Coul$^{-1/2}$]
V — applied potential, Volts

On the other hand, if the Point Defect Model assumptions hold, the left side of Eq. (2-13) must be independent of the potential. Zhang, et al. (1998) argued that the Point Defect Model was more consistent with the experimental data than the High-Field Model, based on the analysis of Eq. (2-13). It must be pointed out, however, that in the limit when the current density approaches steady state, both I' and $I - I_{ss}$ approach zero; therefore, the left side of Eq. (2-13) is not well defined in that limit. Similarly to Eq. (2-9), Eq. (2-13) is dependent on the way the current density versus time data are made smooth. The time derivative, I', is an ill-defined quantity. For example, in Figure 5-1, it is highlighted the stochastic variability in the anodic current density. This variability causes the current density versus time to be a jagged function and its time derivative, I', to be undefined. The time derivative can only be computed for a smooth approximation of the current density versus time curve, and therefore, the left side of Eq. (2-13) is not only strongly dependent on the approach to smooth the data but is only defined for the smooth approximation. Therefore, the discriminating criterion expressed as Eq. (2-13) is not robust.

The critique on Eqs. (2-9) and (2-13) is not intended to invalidate the assumptions used to derive them or the derivation approach but only to highlight that caution must be exercised in applying these equations and interpreting results. The critique also presents the challenge in deriving robust relationships correlating current densities with oxide growth rate laws. Models for the description of the growth of oxide films, in general, present viable mechanisms for the formation of protective films. It must be noted that similar growth rates can be consistent with dissimilar mechanisms of film formation, making difficult the determination of the prevailing mechanisms based only on measurements of film thickness and current density transients. It is evident that understanding the mechanisms of oxide formation and metal dissolution is important, not only from a fundamental point of view but also from a practical point of view because these mechanisms can be used to elucidate approaches to enhance the protective quality of surface oxides against corrosion. It is well accepted, as dictated by industrial experience, that a metallic component displaying passive dissolution caused by the formation of a protective oxide film will last longer than a human lifetime if the passive behavior is not disrupted. To industrial applications, it is relevant to determine factors affecting passivity. This need has dictated major lines of research on the issue of passivity and passivity breakdown for more than a century. Because of lack of importance to most practical applications, long-term implications of mechanisms of passive dissolution have been rarely analyzed, if at all. Alloys to be used to construct waste packages of the potential repository are expected to perform satisfactorily for at least 10,000 years, well beyond what human intuition can envision. In Chapter 5, a model for passive dissolution, based on the Point Defect Model, is proposed, and its implications to long-term performance are analyzed.

3 TEST METHODS FOR DETERMINING PASSIVE CORROSION RATE

In the absence of localized corrosion, uniform corrosion of metals and alloys occurs when the material is exposed to an environment where a water film is in contact with the surface. This contact may occur because of a variety of conditions ranging from full immersion to humid-air exposure and may also include transient conditions such as dripping water contacting the material surface. The rate of uniform corrosion depends on the composition of the material and the chemical composition, pH, and temperature of the environment. Materials, such as stainless steels and nickel-chromium-molybdenum alloys, have corrosion rates independent of potential or the redox potential of the environment throughout a wide range of conditions within the passive range. In the region where the passive oxide film is stable, the corrosion rates are very low {< 1μm/yr [3.9×10^{5} in/yr]} and are controlled by chemical kinetics and transport of cations and oxygen ions through the oxide film.

Passive corrosion rates have been determined using a variety of test methods. The suitability of a given test method depends on a variety of parameters including the material of interest, the environmental conditions of exposure, and the possible mechanisms that will interfere or give rise to measurement errors. For passive materials, such as stainless steels and nickel-chromium-molybdenum alloys several methods have been used to measure the corrosion rate. These methods include gravimetric or weight-loss measurements, potentiostatic measurement of anodic passive current density, polarization resistance, and electrochemical impedance. Although these test methods all have some unique constraints and assumptions, the common assumption is that the measured quantity is caused exclusively by uniform dissolution. This consideration is important because the onset of localized corrosion, if unnoticed, may significantly alter the test results and yield artificially high passive dissolution rates. Specific assumptions and constraints for the test methods are described in the subsequent sections.

There is an important distinction between the gravimetric determination of corrosion rates and the electrochemical methods discussed in this section. The gravimetric determination requires knowledge of the weight loss measured from the difference between initial weights of the test specimens and either the final weights or a series of weight measurements obtained throughout the duration of the exposure. No special instrumentation is required to perform the test which allows the gravimetric method to be used in a wide range of environmental conditions including conditions that are poorly characterized and variable with time. Measurements are discontinuous, however, and can be conducted only at given time intervals. The other methods described are electrochemical methods capable of providing continuous measurement with higher resolution through indirect calculation of corrosion rates, but these methods require sophisticated instrumentation. In addition, electrochemical measurement of corrosion rates cannot easily be performed under highly variable environments such as alternating wet and dry conditions. Electrochemical methods may not be possible for complex systems where the presence of multiple redox reactions could confound the determination of the anodic dissolution reactions rates.

3.1 Gravimetric Determination of Corrosion Rate

3.1.1 Basis of the Gravimetric Method

Gravimetric estimate of corrosion rates is obtained by measuring the change in weight of a test specimen of a known area after a exposure time (ASTM International, 2001a,b). The main advantage is the simplicity of the test. Simple equipment is required to actually measure the dimensions and weight of the specimens prior to and after exposure. Once the area, *A*, and the initial weight, W_i, are known, the specimen is exposed to the environment for a predetermined period. After the exposure is completed, the specimen is retrieved, cleaned, remeasured, and reweighed. The change in weight from W_i to the final weight, W_f, can then be determined. For many materials, such as iron-based alloys (carbon steels and low alloy steels), W_f, after properly descaling the exposed test specimen to remove any corrosion products or deposits, is less than W_i. This weight loss, $\Delta W = W_i - W_f$, is used to calculate the corrosion rate, *CR*, according to Eq. (3-1) (ASTM International, 2001b)

$$CR = \frac{K_w \, \Delta W}{A \, t \, \rho} \qquad (3\text{-}1)$$

where

K_w — constant equal to 8.76×10^4 [3.45×10^6] for a corrosion rate specified in mm/yr [mpy]
t — time of exposure, hours
ρ — density of metal or alloy, g cm^{-3} [lb in^{-3}]

It is important to note that the formation of oxides and oxyhydroxide layers on the metal surfaces can result in a weight increase.

3.1.2 Recommended Practices

Several standard test procedures for gravimetric determination of corrosion rates are published including ASTM G–4, Standard Test Method for Conducting Corrosion Coupon Tests in Plant Equipment, and ASTM G–31, Standard Practice for Laboratory Immersion Corrosion Testing of Materials. Included in both of the ASTM standards are general guidelines for preparing test specimens, test chambers for laboratory tests, and testing conditions. In general, it is suggested that the specimens, typically measuring 50 × 25 × 3 mm [2 × 1 × 0.125 in], should be weighed to the nearest 0.1 mg [2.2×10^{-7} lb] prior to exposure (ASTM International, 2001a,b). The length of the exposure required to obtain an accurate corrosion rate is not fixed and depends on the system under investigation. A general rule of thumb (ASTM International, 2001a,b) for the duration of exposure based on the corrosion rate, *CR*, is shown in Eq. (3-2)

$$\text{Time of Exposure[hours]} = \frac{50}{CR\text{[mm / yr]}} \qquad (3\text{-}2)$$

The guideline for exposure times is intended to provide a minimum time to achieve acceptable results. For example, exposure times that are too short may yield corrosion rates that are too high for systems where the corrosion rate decreases with time. Such decreasing corrosion rates are often observed with materials where the formation of protective corrosion products on the specimen surface occurs. Conversely, corrosion rates may increase with time in systems affected by breakdown of protective films.

3.1.3 Sources of Error in Gravimetric Tests

There are several sources of error for gravimetric tests including errors in the measured area and initial and final weights of the specimens. For passive alloys exposed in systems with low corrosion rates, the errors associated with weight measurements are generally more significant than errors from area measurements. For example, if Alloy 22 {$\rho = 8.69$ g cm^{-3} [543 lb ft^{-3}]} exhibits a corrosion rate of 10^{-5} mm/yr [3.9×10^{-7} in/yr], using a standard size specimen with a surface area of 40.5 cm^2 [6.27 in^2], the weight loss after a 1-year exposure is 0.35 mg [7.7×10^{-7} lb]. Several possible phenomena may interfere with the accurate determination of weight loss, including the increase in oxide layer thickness and the accumulation of deposits and corrosion products on the specimen surface. The thickness of oxide films and deposits needed to offset the weight loss determined previously can be determined according to Eq. (3-3)

$$\text{Thickness of oxides or deposits [cm]} = \frac{3.5 \times 10^{-4}\text{g}}{40.5\ \text{cm}^2\ \rho\ [\text{g cm}^{-3}]} \tag{3-3}$$

For Cr_2O_3 with a density of 5.21 g cm^{-3} [325 lb ft^{-3}], an increase in thickness of 16.6 nm [6.5×10^{-7} in] would result in an increase in weight of 0.35 mg [7.7×10^{-7} lb]. Similarly, for NiO with a density of 7.45 g cm^{-3} [465 lb ft^{-3}], the increase in thickness is 11.4 nm [4.5×10^{-7} in]; whereas, a thickness of 37 nm [1.5×10^{-6} in] is required for SiO_2 with a density of 2.3 g cm^{-3} [144 lb ft^{-3}]. Clearly, small changes in the oxide layer thickness, or thin deposits of low-density compounds such as silica, can alter significantly the measured weight loss and the apparent corrosion rate. Accumulation of silica or calcareous deposits also may act as a diffusion barrier to ions derived from the anodic and cathodic reactions and thus reduce the overall metal loss. Deposits that decrease anodic dissolution rates, also may create significant errors in the corrosion rates calculated from weight loss through a reduction in the active surface area. If decrease in the area occurs, the actual corrosion rate of the areas free of deposits is actually higher than the average rate calculated assuming an uniformly corroding surface. Also, the amount and distribution of these deposits in laboratory tests may not be comparable to service conditions, which may lead to erroneous estimates of corrosion rates.

Besides the interference with corrosion product formation and the accumulation of deposits, the use of gravimetric methods has several significant limitations that cannot be overlooked. First, the corrosion rate calculated is the average corrosion rate for the entire exposure period. For steady-state conditions or well-defined environments, the use of standard corrosion coupons and gravimetric methods may be justified. In contrast, throughout transient conditions, where changes in chemistry, temperature, or other environmental conditions that influence corrosion rates are expected, the average corrosion rates calculated using gravimetric methods will not provide the range of corrosion rates that actually occurred during the time of exposure.

Second, an obvious limitation is the time required to obtain an acceptable result for passive specimens. According to Eq. (3-2), for passive specimens with a corrosion rate of 10^{-5} mm/yr [3.9×10^{-7} in/yr], the ASTM International recommended duration of exposure is 570 years. Arguably, with better resolution of the mass loss measurement, the duration of exposure may be decreased; however, this general guideline clearly demonstrates that valid results for the corrosion rates of passive materials using gravimetric methods require extensive test times.

3.2 Polarization Resistance

3.2.1 Basis of the Polarization Resistance Method

Another popular method to determine uniform corrosion rates is the use of polarization resistance. Polarization resistance is an electrochemical method that determines the amount of current required to polarize the metal or alloy test specimen a few millivolts from the corrosion potential. The corrosion rate of the specimen can then be determined using one of three possible methods. The general relationship between current and potential is given in Eq. (3-4) (Scully, 1995; Oldham and Mansfeld, 1973)

$$I = I_{\mathrm{corr}} \left\{ \exp\left[\frac{2.3(E - E_{\mathrm{corr}})}{\beta_a}\right] - \exp\left[\frac{-2.3(E_{\mathrm{corr}} - E)}{\beta_c}\right] \right\} + C\left(\frac{\partial E}{\partial t}\right) \qquad (3\text{-}4)$$

where

I — current density at any potential, E

I_{corr} — the corrosion current density at corrosion potential, E_{corr}

β_a — anodic Tafel coefficient

β_c — cathodic Tafel coefficient

C — interfacial capacitance of the electrochemical double layer

$\partial E/\partial t$ — potential scan rate

Stern and Weisert (1959) compiled data for a variety of example systems with polarization resistance ranging from < 10 to > 10^6 ohm cm^2 [<1.08×10^{-2} to 1.08×10^3 ohm ft^2].

3.2.2 Recommended Practices

Polarization resistance measurements are conducted in a three-electrode electrochemical cell. The three electrodes consist of a test specimen (or working electrode), a reference electrode, and a counter electrode. Measurements can be conducted by controlling the potential or the current; however, measurements are more reliable by controlling the potential with a potentiostat (Mansfeld, 1977). The electrochemical cell is also used for anodic passive current density measurements and electrochemical impedance spectroscopy.

Polarization resistance measurements are usually performed within a few millivolts of the corrosion potential to avoid perturbing the system too much, which can alter the kinetics of the corrosion process. For passive alloys, growth or alteration of the composition of the oxide film may be a consequence of excessive polarization. The relationship between I and E defined by Eq. (3-4) is valid only if the following assumptions hold (Oldham and Mansfeld, 1973).

- Butler-Volmer equations for electrochemical kinetics are applicable
- No ohmic voltage drops or concentration polarization occur in the system
- The corrosion potential does not lie close to the reversible potential of the metal/metal ion or other oxidizing agent/reduction product
- The entire metal surface behaves as an anode or a cathode
- No secondary electrochemical reactions are present in the system
- No thick film of corrosion products covers the electrode

Calculation of corrosion rates from polarization resistance measurements can be performed using several methods. In the traditional approach originally proposed by Stern and Geary (1957) a polarization resistance, R_p, is calculated from the slope of the E versus I curve at the E_{corr} and this resistance is related to the corrosion current density I_{corr} through Eq. (3-5)

$$R_p = \left.\frac{dE}{dI}\right|_{E_{\text{corr}}} = \frac{\beta_a \beta_c}{2.303(\beta_a + \beta_c) I_{\text{corr}}} \tag{3-5}$$

This method requires knowledge of β_a and β_c which can be problematic especially for systems where I_{corr} varies as a function of time (Oldham and Mansfeld, 1973). An alternative to the traditional polarization resistance approach of Stern and Geary (1957) is to measure the potential current relationship far from the E_{corr} where one term in Eq. (3-4) drops out. To determine the anodic response of a metal far from E_{corr}, assuming no capacitive charging effects, Eq. (3-4) can be reduced to a simple relationship between E and I, given by Eq. (3-6)

$$\log I = \log I_{\text{corr}} + \frac{E - E_{\text{corr}}}{\beta_a} \tag{3-6}$$

By plotting log I versus E, the I_{corr} at E_{corr} can be derived (Oldham and Mansfeld, 1973). Although this method does not require knowledge of β_a and β_c, it does require polarization far from the E_{corr}. For passive metals and alloys, polarization very anodic to E_{corr} may result in changes to the surface structure, such as changes in the thickness or composition of the oxide film, and this may lead to errors in the extrapolation of I_{corr} and the passive corrosion rate.

Oldham and Mansfeld (1973) also suggested a third, graphical method for determining the value of I_{corr} at E_{corr}, which does not require knowledge of β_a and β_c, or polarization far from the E_{corr}. Curve-fitting routines can also be used to simultaneously determine I_{corr}, β_a, and β_c (Mansfeld, 1973), and similar routines are available in corrosion analysis software.

3.2.3 Sources of Error

For metals and alloys with passive films, there are several limitations to the polarization resistance method. Capacitive charging of the oxide films on passive metals can cause significant interference with the polarization resistance method. As indicated in Eq. (3-4), the interference from capacitive charging of the oxide is strongly dependent on the scan rate used in the polarization resistance scan. The effect of oxide surface capacitance and polarization resistance on the maximum scan rate is shown in Table 3-1 (Silverman, 2000, 1998). For a passive metal with a polarization resistance of 10^6 ohm cm^2 [1.55 × 10^5 ohm in^2] and a surface capacitance of 100 μF cm^2 [15.5 μF in^2], the maximum scan rate is 0.005 mV/s. With a lower polarization resistance of 10^5 ohm cm^2 [1.55 × 10^4 ohm in^2] (and correspondingly a higher corrosion rate), the maximum scan rate is increased to 0.05 mV/s. For nickel-chromium-molybdenum alloys with passive corrosion rates as low as 10^{5} mm/yr [3.9 × 10^{-7} in/yr], two concerns arise using the polarization resistance method. First, the magnitude of the polarization resistance is very high. The high polarization resistance results in a very steep *E*

Table 3-1. Maximum Scan Rates For Polarization Resistance Methods (Silverman, 2000).

Solution Resistance (ohm-cm^2)	Polarization Resistance (ohm-cm^2)	Surface Capacitance (μF-cm^2)	Maximum Scan Rate (mV/s)
10	10^3	100	5.10
10	10^4	100	0.51
10	10^5	100	0.05
10	10^6	100	0.005
100	10^3	100	6.30
100	10^4	100	0.51
100	10^5	100	0.05
100	10^6	100	0.005
10	10^3	20	25.00
10	10^4	20	2.50
10	10^5	20	0.25
10	10^6	20	0.025
100	10^3	20	50.00
100	10^4	20	2.60
100	10^5	20	0.25
100	10^6	20	0.025

Reference: Silverman, D.C. "Practical Corrosion Prediction Using Electrochemical Techniques." *Uhlig's Corrosion Handbook*. 2nd Edition. R.W. Revie, ed. New York City, New York: John Wiley and Sons. pp. 1,197–1,225. 2000.

Note: English equivalents are not provided to be consistent with the original data in Silverman (2000).

versus I plot, the slope of which is nearly vertical. In addition, the combination of a high polarization resistance and a passive film capacitance of 100 μF cm^2 [15.5 μF in^2] would limit the maximum scan rate to less than 0.005 mV/s. With such a slow maximum scan rate, time-dependent changes in the E_{corr} will upset the relationship in Eq. (3-4). Using scan rates in excess of the maximum rates identified by Silverman (2000) results in the measurement of current associated with charging of the oxide rather than the current associated with cathodic reduction or anodic dissolution. Thus, use of fast scan rates result in large calculated corrosion rates.

Finally, the resistance of the solution, $R_{solution}$, can also interfere with the measurement of corrosion rates using the polarization resistance method. The potential, E, in Eq. (3-4) is assumed to be the same as the interfacial potential or $E_{interface}$. When the solution resistance is high, however, the value of E is a combination of the interfacial potential and the ohmic potential drop in solution ($I\,R_{solution}$) according to Eq. (3-7)

$$E = E_{interface} + I\,R_{solution} \tag{3-7}$$

Measurements conducted in solutions with a high value of $R_{solution}$ will result in incorrect and high values of the polarization resistance of the metal specimens. In turn, the calculated corrosion rates determined without compensation of the solution resistance are lower than the actual corrosion rates.

3.3 Anodic Passive Current Density

3.3.1 Basis of Corrosion Rate Calculation from the Anodic Passive Current Density

The corrosion rate of a metal specimen may be determined in principle, from the steady-state anodic current density. The corrosion rate, CR, based on Faraday's law, is calculated according to Eq. (3-8)

$$CR = K\frac{I_{corr}\,EW}{\rho} \tag{3-8}$$

where

K — constant equal to 3.27 × 10^{-3} mm mol/(yr cm μA) [2.73 × 10^{-2} mpy mol/(ft μA)]
I_{corr} — anodic current density in μA/cm^2 [μA/ft^2] units
EW — equivalent weight in g/mol [lb/mol] units
ρ — alloy density in g/cm^3 [lb/ft^3] units

The resulting corrosion rate, CR, is in mm/yr [mpy] units. The constant K is the inverse of Faraday's constant. The value of ρ for Alloy 22 is 8.69 g/cm^3 [543 lb/ft^3]. For a passive alloy, the value of EW depends on the atomic fraction and the atomic weight of the alloying elements, and the expected oxidation state of the corrosion products under passive conditions (Brossia, et al., 2001). The passive dissolution of nickel-chromium-molybdenum is expected to result in the formation of Ni(II), Cr(III), Mo(III), and Mo(VI) corrosion products. For Alloy 22, which also contains iron and tungsten, these alloying elements are expected to be oxidized to Fe(II) and W(IV) under passive conditions. The *EW* for Alloy 22 equals 26.04 g/equivalent [0.057 lb/equivalent] if the oxidation states are Ni(II), Cr(III), Fe(II), Mo(III) and W(IV) (ASTM International, 2001c). On the other hand, selecting Ni(II), Cr(III), Fe(II), Mo(VI) and W(VI), results in *EW* equal to 23.28 g/equivalent [0.051 lb/equivalent] (ASTM International, 2001c). In the absence of information on oxidation states, it is conservative to assume the lower oxidation states. Thus, in Chapter 4, corrosion rates are computed from current densities using *EW*=26.04 g/equivalent [0.057 lb/equivalent]. The uncertainty in the oxidation state affects at most by 10 percent (in the negative direction) corrosion rates reported in Chapter 4.

3.3.2 Recommended Practices

Passive current density measurements should be conducted at potentials anodic to the corrosion potential in deaerated solutions to avoid interference with the reduction of oxygen. Since only the net current is measured, deaerated conditions are required to keep the oxygen reduction current from the sufficiently low. In aerated solutions, it is not possible to simultaneously measure passive current and avoid interference with the oxygen reduction reaction because the potentials required to avoid interference are typically in the transpassive region for nickel-chromium-molybdenum alloys. A schematic illustration of the anodic, cathodic, and net current densities are shown in Figure 3-1 for deaerated solutions assuming a passive current density of 10^{-8} A/cm^2 [9.3×10^{-6} A/ft^2]. For applied potentials in the range of 100 mV$_{SCE}$ in deaerated solutions, the net current measured is practically identical to the passive current density. In the example shown, increasing the applied potential does not appreciably decrease the cathodic current contribution to the net current because the cathodic current from the reduction of H$^+$ ions is very small at a potential of 100 mV$_{SCE}$ under deaerated conditions. Decreasing the potential to values in the vicinity of the corrosion potential reduces the net current, and, at the corrosion potential, the net current is zero by definition.

3.3.3 Sources of Error

The limitations of the method of selection of potential and dissolved oxygen are apparent from the preceding discussion. Passive corrosion rates based on steady state passive current densities are approximately 10^{-9} to 10^{-6} A/cm^2 [9.3×10^{-7} to 9.3×10^{-4} A/ft^2]. Several processes can interfere with the ability to accurately measure such low passive current densities. Besides the interference with the cathodic reduction of oxygen or another reducible species (including organic impurities in the water), noise from ground loops or noise from induction heating units may also interfere with the ability to measure the low current densities expected under passive conditions.

Steady-state passive current density can only be measured at potentials where the cathodic reduction reaction does not interfere with the anodic current density. Because the applied potential is far from the corrosion potential, the effects of polarization on the measured current that density must be considered. The example shown in Figure 3-1 and discussed here assumes transpassive dissolution does not occur. In addition, the example also assumes the magnitude of the limiting current from the reduction of oxygen is less than the passive current density (i.e., well deaerated conditions). Because the measured or net current is the sum of the

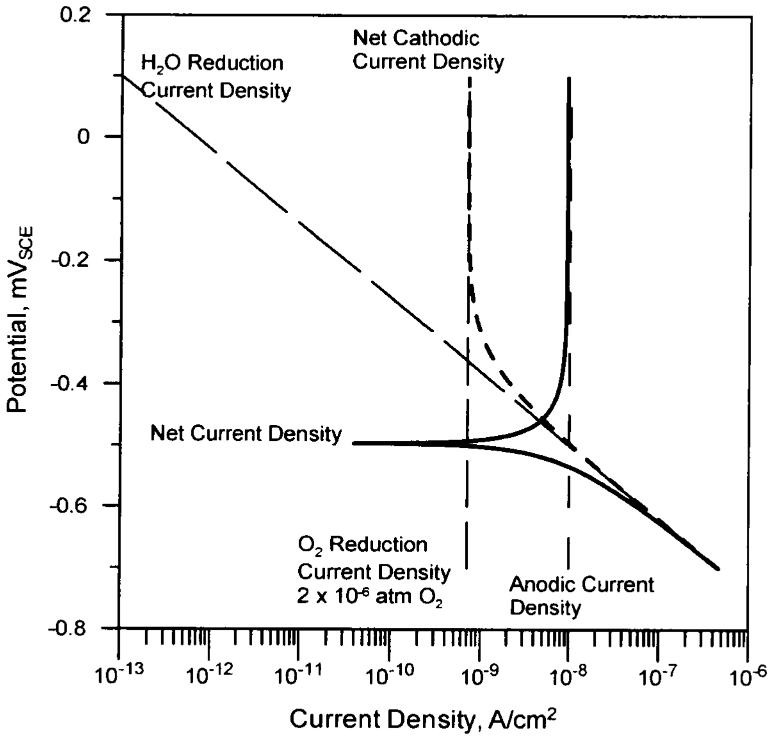

Figure 3-1. Diagram Showing Anodic, Cathodic, and Net Current for a Passive Metal Assuming an i_{corr} of 10^{-8} A cm^{-2} [9.3 × 10^{-6} A/ft^2]

anodic and cathodic currents, the net current can either be substantially reduced or even become cathodic when the dissolved oxygen concentration is large. Thus, to avoid measurement errors that can be attributed to the oxygen reduction reaction, a well deaerated system for the measurement of anodic passive current density under potentiostatic conditions is necessary.

3.4 Electrochemical Impedance Spectroscopy

3.4.1 Basis of the Method

Electrochemical impedance spectroscopy is also useful in the determination of the uniform corrosion rates and the identification of localized corrosion processes (Oltra and Keddam, 1988). An electrochemical impedance spectra is usually obtained by applying a small amplitude potential (or current) perturbation to the working electrode at discrete frequencies over a broad frequency range. At each frequency, the resulting current (or potential) waveform is out of phase with respect to the applied perturbation signal. The electrochemical impedance is the frequency-dependent-proportionality factor that acts as a transfer function between the excitation potential (or current) signal and the current (or potential) response (Scully, 1995).

Electrochemical impedance is a versatile method to characterize the electrochemical response of a corroding metal. It can be used to rapidly estimate the corrosion rate and can be applied to systems with extremely low corrosion rates {< 10^{-4} mm/yr [4 × 10^{-6} in/yr]}. By scanning a wide range of frequencies, the solution resistance and the polarization resistance of the metal can be uniquely characterized. Thus, electrochemical impedance spectroscopy can be used to determine the corrosion rates of metals in low-conductivity electrolytes. In addition, electrochemical impedance spectroscopy also can be used to assess the performance of inhibitors and coatings (Silverman, 2000).

The impedance response of the electrochemical interface of metals exposed to an electrolyte is often modeled as an analog circuit where the circuit components are selected to represent physical features of the electrical interface (Gabrielli, 1990, 1984). Except for purely resistive systems, the impedance is a function of frequency (Epelboin, et al., 1981). Resistive elements are typically used to represent polarization and solution resistance. The impedance response for resistors is given in Eqs. (3-9) through (3-11).

$$Z = R \tag{3-9}$$

$$Z' = R \tag{3-10}$$

$$Z'' = 0 \tag{3-11}$$

where

Z — complex impedance
Z' — real component of the impedance, Z
Z'' — imaginary components of the impedance, Z

Capacitive circuit elements are typically used to quantify the electrical double layer, coating, and oxide film capacitances. The impedance response of a capacitor is given by

$$Z = \frac{1}{i \omega C} \tag{3-12}$$

where

i — square root of -1
C — capacitance
ω — frequency

In other words, the real and imaginary components of the complex impedance of a capacitor are

$$Z' = 0 \tag{3-13}$$

and

$$Z'' = -\frac{1}{\omega C} \tag{3-14}$$

Inductive elements are used to quantify a process such as adsorption. The impedance response for an inductor is given in Eqs. (3-15) through (3-17)

$$Z = i\,\omega\,L \tag{3-15}$$

$$Z' = 0 \tag{3-16}$$

$$Z'' = \omega\,L \tag{3-17}$$

where L is the inductance of the system.

Constant phase elements also can be used to model the response of coatings and have a response that can be described as a leaky capacitor. The impedance response for a constant phase element is given by Eq. (3-18)

$$Z = \frac{1}{T(i\,\omega)^{P}} \tag{3-18}$$

where T is a capacitive term.

The exponent, P, characterizes the response of the constant phase element. When $P = 1$, the constant phase element is identical to a capacitor. When $P = 0.5$, the constant phase element behaves as an infinite length Warburg element used to quantify diffusion processes.

Finally, the Warburg element, frequently used to model diffusion processes, has an impedance response given by Eq. (3-19)

$$Z = \frac{R\tanh[(iT\omega)^{P}]}{(iT\omega)^{P}} \tag{3-19}$$

where R is a constant with units of resistance.

The parameter, $P = 0.5$, for a finite length Warburg element. The parameter, T, is related to the effective diffusion thickness, L, and the effective diffusion coefficient, D, according to Eq. (3-20).

$$T = \frac{L^2}{D} \tag{3-20}$$

3.4.2 Recommended Practices

Generating impedance spectra of a corroding metal surface is usually performed using commercially available instrumentation, such as a potentiostat and a function generator, with a frequency response analyzer controlled by a computer. Impedance spectra are typically obtained using a 10 mV sinusoidal perturbation, however, smaller or larger potential signals can be used so long as the relationship between the potential perturbation and the response current is linear (Silverman, 2000). Standard procedures for collecting electrochemical impedance spectra and verifying the performance of the impedance instrumentation are available (ASTM International, 2001d).

The frequency range for which the impedance spectrum must be obtained depends on the system characteristics. The maximum frequency should be high enough that the impedance of the system is determined by the solution resistance, R_{sol}. If the value of R_{sol} can be obtained at the frequency f_{max} then the upper frequency, f, for the impedance spectrum should be slightly greater than f_{max} according to Eq. (3-21) (Scully, 1995).

$$f > f_{max} = \frac{1}{2\pi C R_{sol}} \tag{3-21}$$

where C is the capacitance of the system.

The minimum frequency, f_{min}, is also dependent on the system characteristics. If the breakpoint frequency, f_{bp}, is the frequency where the impedance of the system is determined by the sum of R_p and R_{sol}, then f_{min} can be calculated according to Eq. (3-22) (Scully, 1995)

$$f_{min} < f_{bp} = \frac{1}{2\pi C(R_{sol} + R_p)} \tag{3-22}$$

Analyses of electrochemical impedance data are often performed by constructing an analog circuit from components mentioned previously (Gabrielli, 1984, 1990). The analog circuit elements are chosen based on the physical characteristics of the system under investigation. A simple model for a corroding metal interface may be described using a Randel's circuit, shown in Figure 3-2, which is composed of a solution resistance, a Faradaic impedance or polarization resistance (also called charge transfer resistance) and a double-layer capacitance (Schueller and Taylor, 1993). The impedance response of anodic oxides on aluminum alloys has been modeled using equivalent circuits that have components for both the porous outer oxide layer and the inner nonporous oxide layer as shown in Figure 3-3 (Dawson, et al., 1993). More complex models have also been proposed to account for the electrolyte resistance in the oxide pores (Dawson, et al., 1993). Charge transfer across a passive film has also been modeled using an equivalent circuit with a diffusional impedance or constant phase element shown in Figure 3-4 (Scully, 1993).

3.4.3 Sources of Error

Although electrochemical impedance spectroscopy is a versatile technique that can be used on a variety of applications, including the corrosion of passive metals, several difficulties may lead to an incorrect system characterization. Silverman (2000) summarized four attributes characteristic of a valid and useful electrochemical impedance spectrum. First, it must be assured that the impedance spectrum recorded is the result of the input perturbation as opposed to an artifact of the system being investigated. As previously indicated, the response of the system should be linear and the system should be stable. The impedance must be finite as the frequency approaches zero and large values, and continuous at all intermediate frequencies.

Assuming the validity of the electrochemical impedance spectrum can be verified, another difficulty in the analyses of impedance spectra is determining the most appropriate analog circuit model. Determination of the correct analog circuit model can be nontrivial, especially

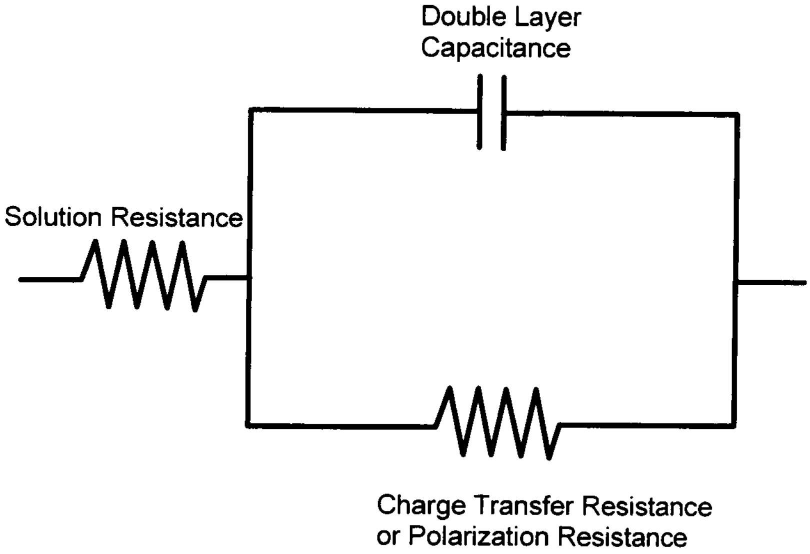

Figure 3-2. Electrical Analog Composed of a Solution Resistance, Polarization Resistance and a Double-Layer Capacitance

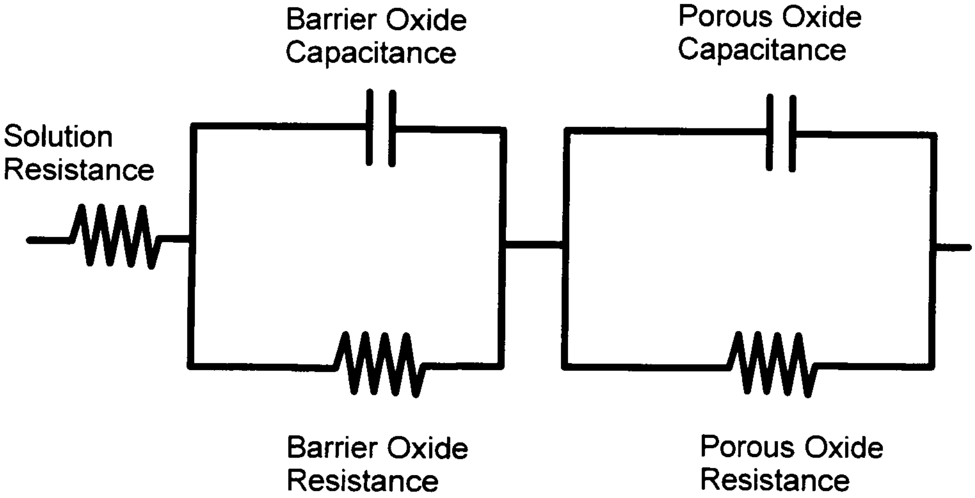

Figure 3-3. Electrical Analog Circuit for a Passive Oxide Film Composed of a Barrier Layer and a Porous Layer

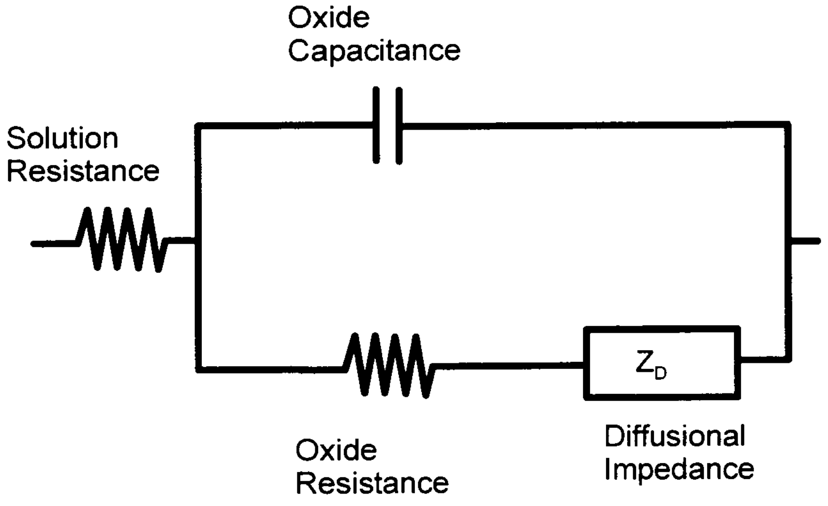

Figure 3-4. Electrical Analog Circuit with an Oxide Resistance, Oxide Capacitance, and a Diffusional Impedance

when the system is complex. In addition, several possible analog models may have the same or similar impedance responses (Silverman, 2000; Fletcher, 1994). Signal noise can also be a problem for the analyses of impedance spectra and in some cases can limit the ability of nonlinear regression circuit fitting routines to distinguish between different possible analog circuit models (Silverman, 2000, 1991).

Corrosion rates can be estimated from the low-frequency limit of the impedance modules. Such estimates may be valid if the value of R_{sol} is either known or small compared to R_p, the conditions in Eq. (3-22) are satisfied, and no inductive behavior exists. The presence of inductive processes, such as adsorption of species on the corroding metal surface, may result in significant error in the estimation of R_p and the metal corrosion rate (Silverman, 2000). It should be noted that once a value of R_p is obtained, the corrosion rate can, in principle, be determined using Eq. (3-5), assuming that appropriate values of β_a and β_c are known. In practice, the electrochemical impedance technique is limited to the same assumptions as the direct current polarization resistance method.

3.5 Long-Term Extrapolation Assumptions

Assuming that the corrosion rate, *CR*, has been measured by any technique previously discussed, the time it would take the corrosion front to penetrate a slab of material (of thickness *d*) assuming the system is at a constant temperature, is computed as

$$t = \frac{d}{CR} \tag{3-23}$$

The assumptions behind the validity of Eq. (3-23) are rarely discussed. For industrial applications, it is only relevant that the time, *t*, is in excess of the useful lifetime of the equipment (decades at most) where the metallic component is used, and, in general, that is the case for metals displaying passive behavior. In this report, dealing with the performance of a passive alloy in thousands of years, an understanding the validity of Eq. (3-23) is highly relevant. These assumptions are

Assumption No. 1:	The dissolution process is stoichiometric (i.e., the rate of dissolution of the various alloy elements is congruent with the composition of the alloy)
Assumption No. 2:	Dissolution is planar (i.e., the shape of the corrosion front is planar and perpendicular to the direction of the penetration)
Assumption No. 3:	The corrosion rate does not change with time (i.e., it is a steady-state quantity assuming other environmental variables, such as the temperature, remain constant)

Experimental evidence (Cavanaugh, et al., 1983) indicates that dissolution is not necessarily stoichiometric for Alloy C-276 (Ni-16Cr-16Mo-4W-5Fe, which is similar to the Alloy 22 composition), in chloride environments, at least in short-term experiments. The topic of stoichiometric dissolution is addressed in Section 5.4, where it is concluded that although dissolution initially may be nonstoichiometric, the system naturally evolves toward stoichiometry, provided the rates of diffusion of the various elements in the alloy are similar to each other. There is some natural analog evidence, according to the analysis of meteoritic iron-nickel alloys, that long-term dissolution proceeds in stoichiometric form (Sridhar and Cragnolino, 2002).

Planar dissolution is one central assumption in the computation of the failure time using Eq. (3-23). The corrosion rate, *CR*, is assumed uniformly distributed across the corroding surface area. Variability in the corrosion rate can occur because surface heterogeneity (e.g., caused by the presence of inclusions, primary carbides, and surface defects) and thermal and quantum dynamical fluctuations. Therefore the corroding surface could roughen as dissolution proceeds. There is some experimental evidence of the roughening phenomenon for Alloy 22 (Bedrossian and Farmer, 1999). Besides the stochastic nature of the process, the corroding surface could also increase in roughness due to other mechanisms, such as periodic local rupture of the film, defects in the alloy, and exposition of grain boundaries and inclusions. This topic of planar dissolution is discussed in Section 5.3.

Alloy 22 is expected to reach an average steady-state corrosion rate that can be correlated to an average steady-state anodic passive current density, assuming that environmental variables, such as the temperature, are invariant with time. Variability around the average steady-state value is expected because of the stochastic nature of the dissolution process. The natural trend for metals and alloys is to continuously evolve toward ore state (Sridhar and Cragnolino, 2002). Metals are, in general, found in nature in oxide form. The initial formation of an oxide film on the surface of the alloy causes the physical separation of the metal from the environment. The interface oxide controls the rate of dissolution of the metal (or the rate of transformation of the metal into the ore state) and this rate is slow for Alloy 22 passive metals. The rate of metal dissolution or corrosion rate must reach an average steady-state value in a short period. The time at which this steady-state value is reached is not necessarily the same time required for the formation of an oxide of constant thickness. Solid-state anodic reactions associated with the formation of oxides at low temperatures {<100 °C [212 °F]} are fast, and oxides usually reach a steady-state thickness (of several nanometers) within minutes (or hours at most) after initiation of the oxidation process. Experimental anodic passive current densities for Alloy 22 in chloride solutions at 95 °C [203 °F], reported in Chapter 4, seem to reach steady-state after 2 weeks of the initiation of the experiments. In Chapter 5, it is argued that the steady-state value of the anodic current density is a function not only of the kinetics of the anodic dissolution reactions, but also of the rate of solid-state transport of the elements in the alloy and saturation concentration values of vacancies at the metal-film interface. Understanding the dissolution process is highly relevant to envision possibilities in the evolution of Alloy 22 dissolution that could compromise its long-term performance, and factor these possibilities into the uncertainty of total system performance assessments of the proposed repository. The steady-state value of the dissolution rate is discussed in Sections 5.2.4 and 5.3.

4 MEASUREMENTS OF PASSIVE CORROSION RATES

The uniform corrosion rate of Alloy 22 under passive conditions was measured using anodic passive current density and polarization resistance methods. Tests were conducted using a computer controlled potentiostat and the resolution of the current measurement was determined to be 1.25×10^{-10} A/cm^2 [1.16×10^{-7} A/ft^2]. Smooth cylindrical specimens measuring 6.3 mm [0.25 in] in diameter and 48 mm [1.89 in] long with an exposed surface area of 8 cm^2 [1.24 in^2] were used in most of the tests. Long-term potentiostatic tests were also conducted using larger specimens with a surface area of 72 cm^2 [11.2 in^2]. Tests were conducted in 2-L [0.53-gal] test cells at 20 and 95 °C [68 and 203 °F] in N_2-deaerated solutions. Test cells were fitted with a water-cooled Allihn-type condenser and a water trap to minimize solution loss at elevated temperatures and air intrusion. A saturated calomel electrode was used as a reference electrode in all experiments. The saturated calomel electrode was connected to the solution through a water-cooled Luggin probe with a porous silica tip to maintain the reference electrode at room temperature. A platinum flag was used as a counter electrode. All solutions were deaerated with high-purity nitrogen (99.999 percent) for at least 24 hours prior to the start of the tests.

4.1 Potentiostatic Anodic Passive Current Density Measurements

The anodic passive current density was measured on specimens maintained under potentiostatic conditions. The specimens were held at potentials above the corrosion potential in the deaerated solutions. The composition of the test solutions used in short-term potentiostatic tests was 0.028 to 4.0 M NaCl at various pH's (Dunn and Brossia, 2002; Brossia, et al., 2001). Additional potentiostatic anodic current density tests were conducted in solutions containing 0.028 M NaCl with and without the addition of either 0.052 M NaF or 0.021 M Na_2SO_4. At the conclusion of the test, the specimens were reweighed and examined microscopically for signs of corrosion. Initial short term tests were conducted for 48 hours (Dunn and Brossia, 2002; Brossia, et al., 2001). The short-term tests were performed using a range of potentials, temperatures, and chloride concentrations. Longer tests were conducted using potentiostatic holds at 100 mV$_{SCE}$, which is above the corrosion potential and below the potential for transpassive dissolution, at temperatures ranging from 95 to 25 °C [203 to 77 °F] to obtain the temperature dependence of the passive dissolution rate. Corrosion rates were calculated using Eq. (3-8) and an equivalent weight of 26.04 based on the assumption of congruent dissolution of the major alloying elements as Ni^{2+}, Cr^{3+}, Mo^{3+}, Fe^{2+}, and W^{4+} (ASTM International, 2001c).

Short-term measurements, conducted at potentials in the range of -200 to approximately 400 mV$_{SCE}$, exhibited current densities characteristic of passive dissolution, with values lower than 10^{-7} A/cm^2 [9.3×10^{-5} A/ft^2]. In addition, the current densities measured were almost independent of potential, chloride ion (Cl^-) concentration, and pH. For potentials in the range -200 to 200 mV$_{SCE}$, in either 0.028 and 4.0 M Cl^- with pH of 2.7 to 8.0, the anodic current density was between 8×10^{-9} and 4×10^{-8} A/cm^2 [7.4×10^{-6} and 3.7×10^{-5} A/ft^2] at 95 °C [203 °F], corresponding to corrosion rates of approximately 8×10^{-5} to 4×10^{-4} mm/yr [3.1×10^{-6} to 1.6×10^{-5} in/yr] (Dunn and Brossia, 2002; Brossia, et al., 2001). Slightly higher passive current densities were observed for welded specimens, typically between two and four times greater than the corrosion rates measured for the mill annealed material

(Dunn, et al., 2000b). The passive current density decreased to 2 × 10^{-9} A/cm^2 [1.9 × 10^{-6} A/ft^2] when the temperature decreased to 20 °C [68 °F] (Dunn and Brossia, 2002; Brossia, et al., 2001).

It should be noted that the passive current density measured in short-term tests was obtained after polarization for 48 hours, however, the measured current density in many cases steadily decreased with time. The anodic current obtained in 0.028 M NaCl at 95 °C [203 °F] for 48 hours is shown in Figure 4-1. The specimen was maintained at a potential of 200 mV$_{SCE}$. At the start of the test, the anodic current density was 2.5 × 10^{-8} A/cm^2 [2.3 × 10^{-5} A/ft^2]. The anodic current density varied between 6.0 × 10^{-8} and 1.5 × 10^{-9} A/cm^2 [5.6 × 10^{-5} and 1.4 × 10^{-6} A/ft^2] for the 48-hour test. Extended tests were conducted to observe the evolution of the anodic current for longer periods. Figure 4-2 shows the measured anodic current density for a 72 cm^2 [11.2 in^2] Alloy 22 specimen in 0.028 M NaCl at temperatures ranging from 95 to 25 °C [203 to 77 °F]. The specimen was maintained at a potential of 100 mV$_{SCE}$. The anodic current density was observed to decrease continually with time, while the temperature was maintained at 95 °C [203 °F]. At the beginning of the test, the anodic current density was 2 × 10^{-8} A/cm^2 [1.9 × 10^{-5} A/ft^2]. As the temperature was decreased, the anodic current decreased. At 25 °C [77 °F], the anodic current density was typically less than 10^{-9} A/cm^2 [9.3 × 10^{-7} A/ft^2]. It is apparent from Figure 4-2 there is significant measurement noise even with the implementation of procedures to reduce electrical noise and the use of isolation transformers.

Similar measurements were also conducted using a solution containing 0.028 M NaCl and 0.052 M NaF (Figure 4-3). Initially, the anodic current density was also near 2 × 10^{-8} A/cm^2 [1.9 × 10^{-5} A/ft^2] and continually decreased with time while the temperature was maintained at 95 °C [203 °F]. A decrease in anodic current density was observed immediately after the temperature was decreased to 80 °C [176 °F]. The anodic current density and the noise increased with time. No appreciable decrease in the anodic current density was observed after the temperature was decreased to 60 and 40 °C [140 and 104 °F]; however, the current density decreased to 2 × 10^{-9} A/cm^2 [1.9 × 10^{-6} A/ft^2] when the temperature was decreased to 25 °C [77 °F].

A comparison with the anodic current density at 95 °C [203 °F] for three solutions is shown in Figure 4-4. In these tests, the initial anodic current density is near 2 × 10^{-8} A/cm^2 [1.9 × 10^{-5} A/ft^2] and decreases for the extended test period. At 200 hours, the highest anodic current density in these tests was observed for the 0.028 M NaCl solution {approximately 1.1 × 10^{-8} A/cm^2 [1.02 × 10^{-5} A/ft^2]}. A slightly lower value of 9 × 10^{-9} A/cm^2 [8.4 × 10^{-6} A/ft^2] was recorded after 200 hours in the 0.028 M NaCl solution with the addition of 0.052 M NaF. In the solution containing 0.028 M NaCl + 0.021 M Na_2SO_4, the anodic current density after 200 hours was approximately 7 × 10^{-9} A/cm^2 [6.5 × 10^{-6} A/ft^2]. From Figure 4-4, it is apparent that the test conducted in the 0.028 M NaCl + 0.021 M Na_2SO_4 solution had significant scatter in the data for a period spanning 50 to 150 hours. No conditions were identified that would lead to the large deviation in measured anodic current density for this time period.

From anodic current densities, the calculated corrosion rates for Alloy 22 varied from approximately 2 × 10^{-4} mm/yr [8 × 10^{-6} in/yr], based on the initial anodic current densities measured at 95 °C [203 °F] in 0.028 molar NaCl, to 7 × 10^{-5} mm/yr [3 × 10^{-6} in/yr], based on the anodic current density measured after 200 hours in 0.028 molar NaCl + 0.021 molar Na_2SO_4. It should be noted that these corrosion rate calculations are based on the mean

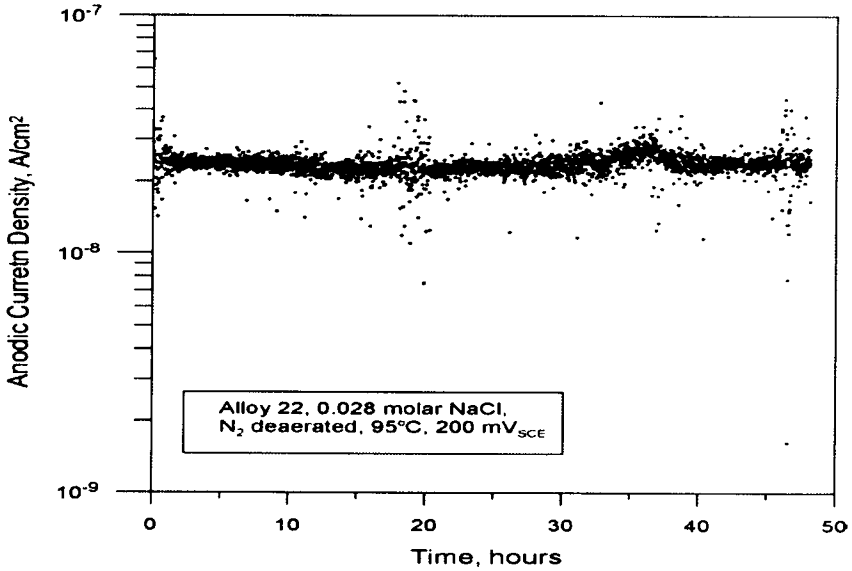

Figure 4-1. Anodic Current for Alloy 22 Measured For 48 Hours in Deaerated 0.028 M NaCl at a Potential of 200 mV$_{SCE}$ and at 95 °C [203 °F]

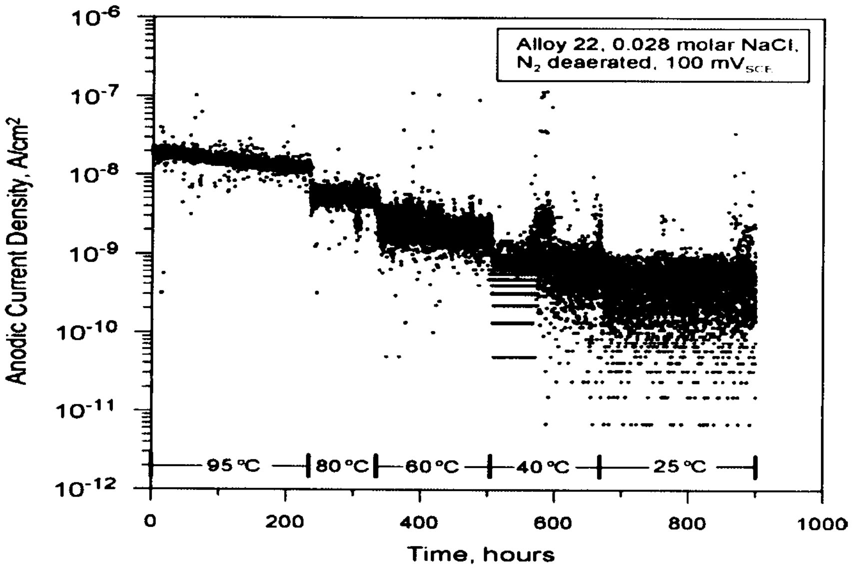

Figure 4-2. Measured Anodic Current Density for an Alloy 22 Specimen Maintained at 100 mV$_{SCE}$ in Deaerated 0.028 M NaCl

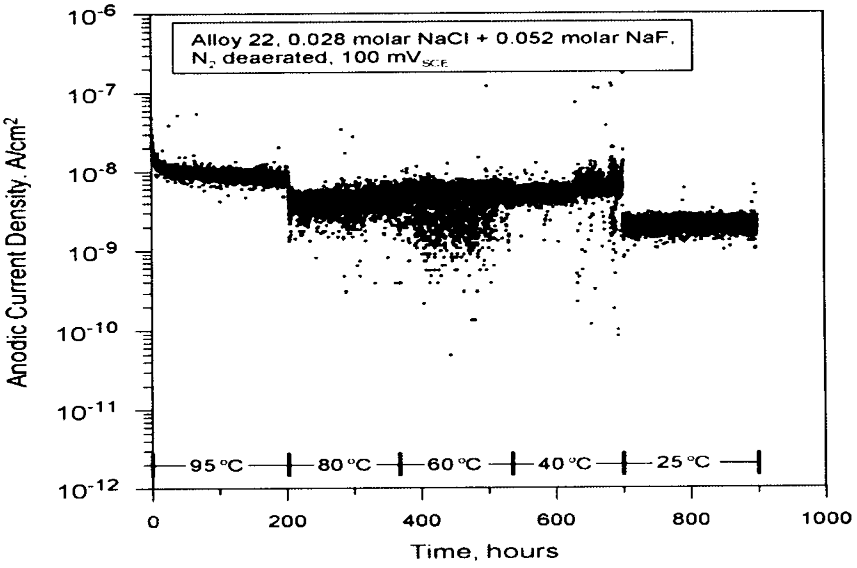

Figure 4-3. Measured Anodic Current Density for an Alloy 22 Specimen Maintained at 100 mV$_{SCE}$ in Deaerated 0.028 M NaCl + 0.052 M NaF

current density and the range of corrosion rates that can be calculated based on the range of anodic current densities measured for a relatively short period of time (i.e., a few hours) can, at a minimum, vary by a factor of two. At 25 °C [77 °F], a mean corrosion rate of approximately 7×10^{-6} mm/yr [3×10^{-7} in/yr] can be calculated from the anodic current density measured in 0.028 M NaCl (Figure 4-2). In comparison, the corrosion rate calculated from the anodic current density measured in the 0.028 M NaCl + 0.052 M NaF solution was 2×10^{-5} mm/yr [8×10^{-7} in/yr] (Figure 4-3). In general, mean values of the anodic current density decreased with decreasing temperature. At 40 and 20 °C [104 and 68 °F] in 0.028 M NaCl, the lowest values of the anodic current density approached the resolution limit of the instrument and the net current was often cathodic.

4.2 Polarization Resistance

Polarization resistance measurements were conducted by measuring the current density while scanning the potential of the test specimens in the anodic direction over the range −15 to +15 mV or −15 to +60 mV, with respect to the corrosion potential. Tests were conducted in a deaerated 0.028 M Cl^- solution. The glass frit used to deaerate the test solution was initially placed in solution to sparge the solution with high-purity nitrogen gas that was passed through an oxygen scrubber prior to the test cell. Prior to conducting measurements, the frit was elevated above the solution level to prevent agitation of the solution. Isolation transformers were used to reduce electrical noise, and the test cell was placed into a Faraday cage. The value of the polarization resistance, R_p, was obtained by fitting a straight line to the data in the range −5 to +5 mV with respect to the corrosion potential.

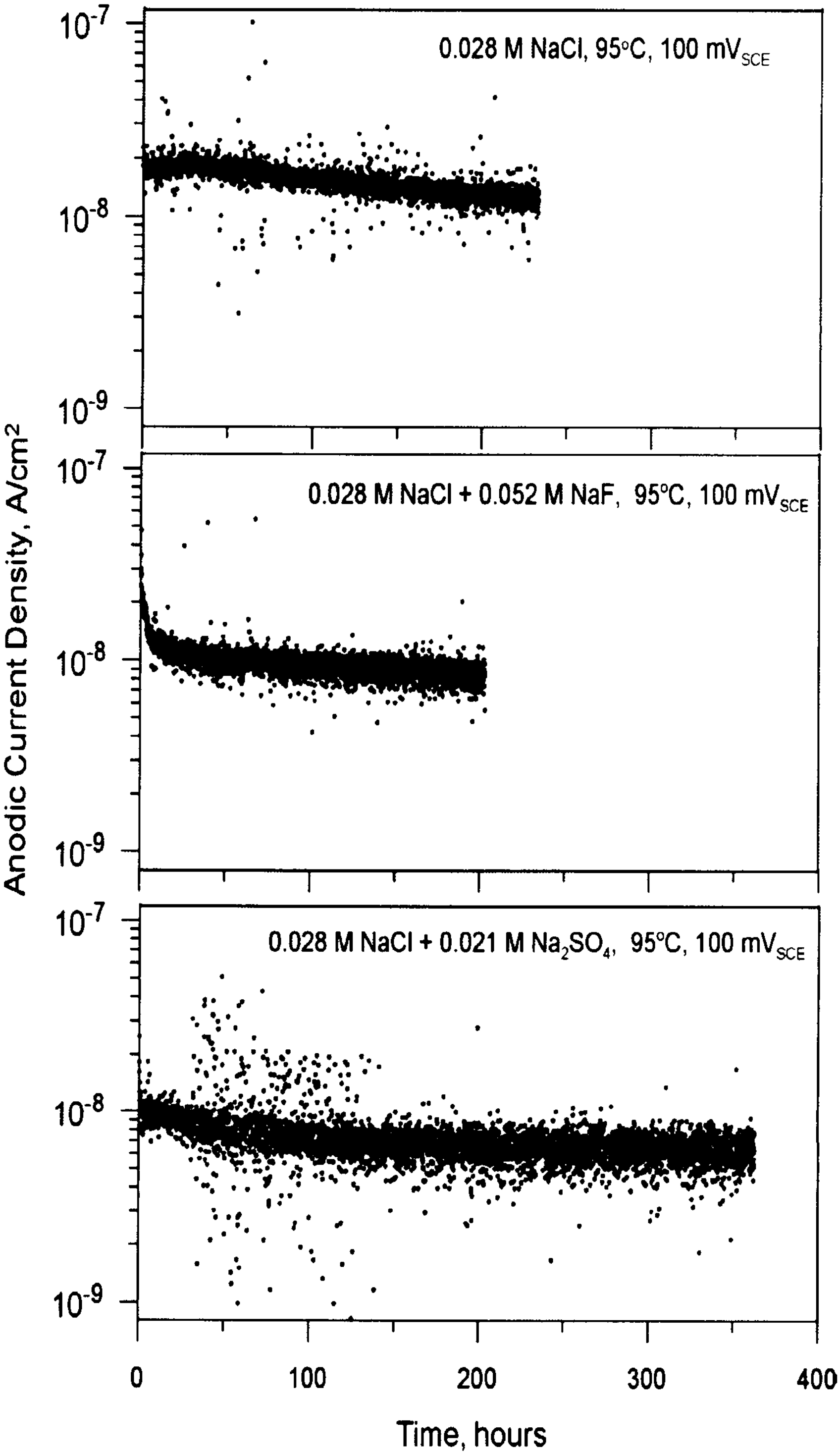

Figure 4-4. Measured Anodic Current Density for an Alloy 22 Specimen Maintained at 100 mV_{SCE} in Deaerated Solutions at 95 °C [203 °F]

The corrosion current density was calculated using Eq. (4-1)

$$I_{\text{corr}} = \frac{\beta_c}{2.303\,R_p} \tag{4-1}$$

which derived from Eq. (3-5) assuming a value of "infinity" for the anodic Tafel slope, β_a (Epelboin, et al. 1981) and a value of 0.120 V/decade of current for the cathodic Tafel slope, β_c. The corrosion rate was then calculated by using Eq. (3-8). An alternate method of calculating the corrosion rate was also used. This method, described by Oldham and Mansfeld (1973), was implemented by calculating the slope of the polarization curve, in the anodic region, at a potential at least 30 mV anodic to the corrosion potential and then extrapolating the anodic current density at the corrosion potential. The scan rate was varied from to 0.001 to 1.0 mV/s. The slower scan rates are required to avoid the effects of capacitance charging of the oxide layer (Silverman, 2000). The faster scan rates, within the range investigated, were used to determine the maximum scan rate that can be used and still avoid interference from the effect of oxide capacitance charging.

An example of a potential versus current density plot from which the polarization resistance was determined is shown in Figure 4-5. The corrosion potential was $-0.464\ V_{SCE}$ and the scan was conducted from -15 to +15 mV with respect to the corrosion potential using a scan rate of 0.001 mV/s. The potential versus current density for a region -5 to +5 mV, with respect to the corrosion potential, is shown in Figure 4-6. The calculated polarization resistance for this condition was 3.6×10^{6} ohm cm^2 [5.6×10^{5} ohm in^2]. The calculated corrosion current density was 1.4×10^{-8} A/cm^2 [1.3×10^{-5} A/ft^2], and the corrosion rate was determined to be 1.4×10^{-4} mm/yr [5.5×10^{-6} in/yr]. This corrosion rate is comparable to the corrosion rate obtained using the anodic passive current density measured at a potential of 0.1 V_{SCE}. It is apparent from Figure 4-6, however, that there is significant scatter in the data even though efforts were made to reduce the noise of the system. The best fit line has an R^2 value of 0.029, which is a result of the scatter in the data.

A comparison of the polarization resistance values for Alloy 22 in deaerated 0.028 M NaCl as a function of scan rate is shown in Figure 4-7. For scan rates of 0.01 mV/s or less, the polarization resistance does not appear dependent on scan rate, suggesting no significant effects of capacitive charging. The polarization resistance decreases by more than one order of magnitude when the scan rate is increased to 0.1 mV/s and continued to decrease as the scan rate increased. Corresponding corrosion rates as a function of scan rate are shown in Figure 4-8. Using the polarization resistance obtained from the data spanning -5 to +5 mV, with respect to the corrosion potential, the corrosion rate is between 10^{-4} and 3×10^{-4} mm/yr [4×10^{-6} and 10^{-5} in/yr] for scan rates of 0.0005 to 0.01 mV/s. In contrast, corrosion rates ranging from 6×10^{-3} to 4×10^{-2} mm/yr [2×10^{-4} to 1.6×10^{-3} in/yr] were calculated from the polarization resistance when the scan rate was 0.1 to 1.0 mV/s. Corrosion rates for Alloy 22 obtained by a linear regression to the polarization data 30 to 40 mV anodic to the corrosion potential, were similar to the corrosion rates obtained from the polarization resistance method, except at low scan rates. A similar scan rate dependence for both methods, polarization resistance and linear regression, is also apparent from Figure 4-8.

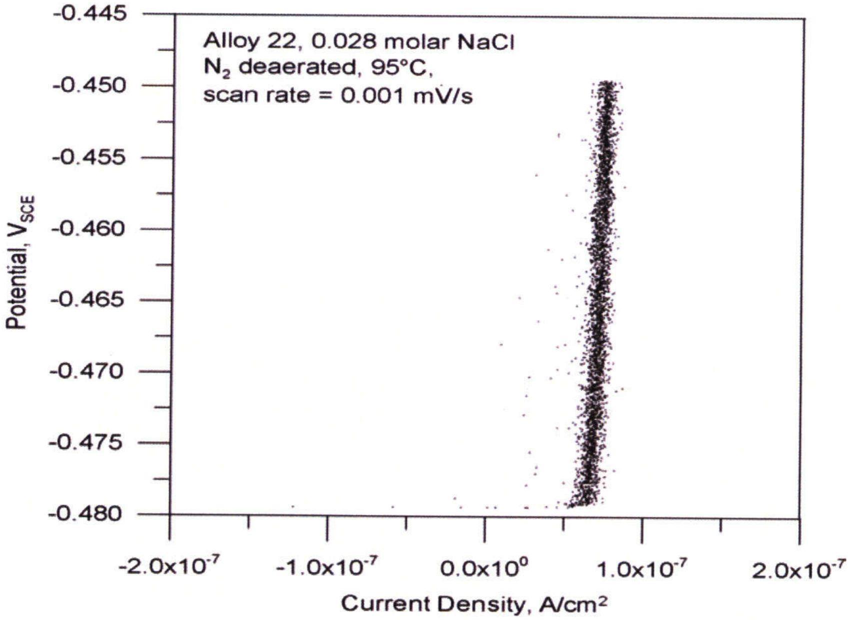

Figure 4-5. Potential Versus Current Density for Alloy 22 in Deaerated 0.028 M NaCl at 95 °C [203 °F] Obtained Using a Scan Rate of 0.001 mV/s

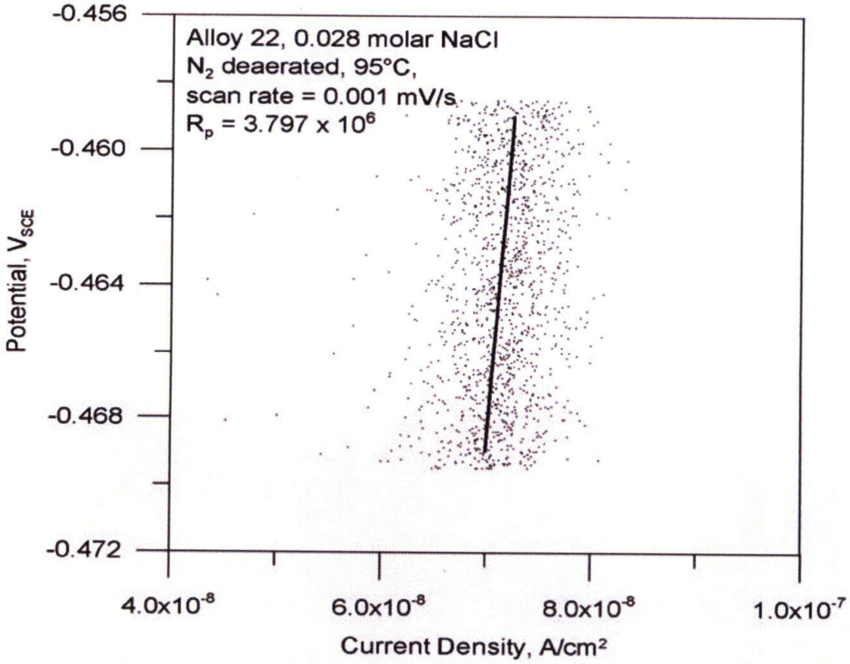

Figure 4-6. Polarization Resistance Determined from Potential Versus Current Density for Alloy 22 in Deaerated 0.028 M NaCl at 95 °C [203 °F] Obtained Using a Scan Rate of 0.001 mV/s; Only Points Within 5 mV of the Corrosion Potential Were Used To Determine Polarization Resistance

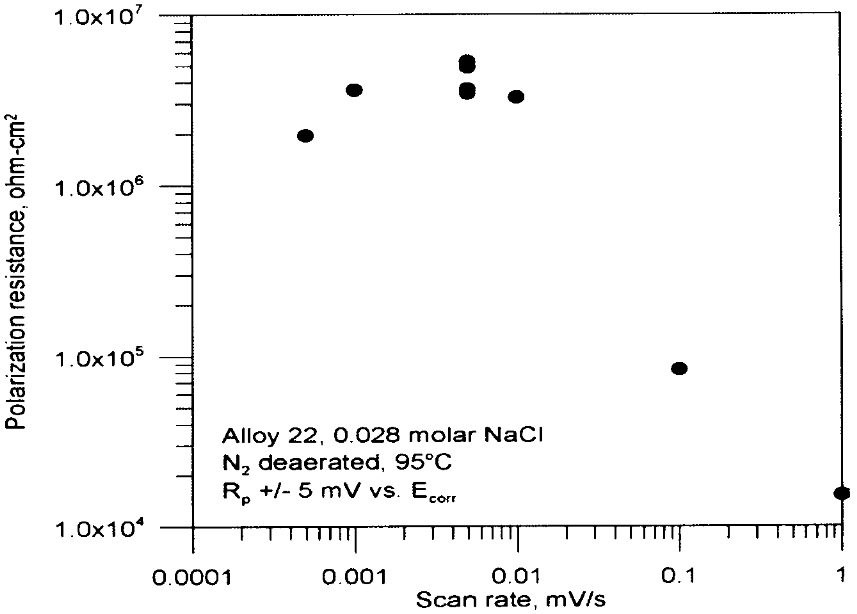

Figure 4-7. Polarization Resistance as a Function of Scan Rate for Alloy 22 in Deaerated 0.028 M NaCl at 95 °C [203 °F]

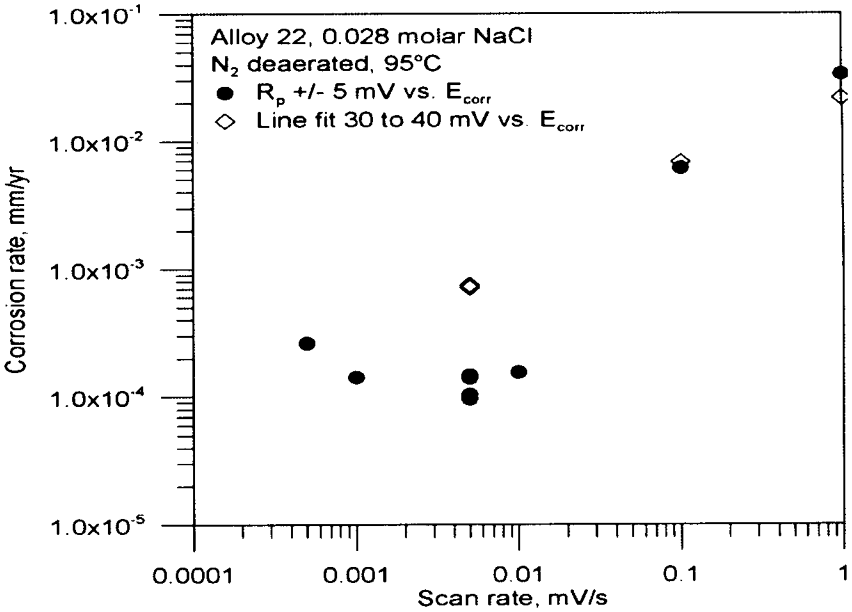

Figure 4-8. Corrosion Rates for Alloy 22 in Deaerated 0.028 M NaCl at 95 °C [203 °F] Determined Using Polarization Resistance and Linear Regression Methods

Decreasing the temperature from 95 to 80 °C [203 to 176 °F] decreased the corrosion rate (determined from polarization resistance data) from 1.4×10^{-4} to 8.0×10^{-5} mm/yr [5.5×10^{-6} to 3.1×10^{-6} in/yr]. When the temperature was decreased to 60 °C [140 °F], the polarization resistance was -5.8×10^{-8} ohm cm^2 [-9×10^{-9} ohm in^2] corresponding to a negative corrosion rate of -8.8×10^{-7} mm/yr [-3.5×10^{-8} in/yr]. Clearly, the negative corrosion rate is not a valid measurement; however, it should be reiterated that with all polarization resistance data, poor fit statistics result from the scatter in the data, implying a significant uncertainty in the polarization resistance.

4.3 Derivation of the Apparent Activation Energy

Data in Figure 4-2 were used to estimate the apparent activation energy (corresponding to an Alloy 22 specimen maintained at 100 mV$_{SCE}$ in deaerated 0.028 M NaCl). Median values and 5th- and 95th-percentile envelopes were computed for the passive current density as a function of time and are included into Figure 4-9(a). The median, 5th- and 95th-percentile statistics were computed by dividing the time domain into 100 intervals for each temperature and computing the statistics with the points contained in each interval (approximately 40 points per interval). Figure 4-9(b) contains the same median curves as those in Figure 4-9(a), but with the time axis shifted so that the time of temperature transition coincides with the origin for all the different temperatures. Figure 4-9(b) is intended to facilitate the visualization of the effect of the temperature on the passive current density.

For each temperature, a unique value of the passive current density was selected to allow the estimation of an apparent activation energy. This unique value was derived by computing an average of the last few points (five were selected) of the median curves [i.e., those curves in Figure 4-10(b)] before the transition of the system to a new temperature. The five points so derived (one for each temperature) were plotted as a logarithm of the current density versus the inverse of the temperature representation [see Figure 4-10(a)]. The dependence of the passive current density on the temperature is of an Arrhenius form:

$$I = I_o e^{-\frac{E_a}{RT}} \tag{4-2}$$

where

I — passive current density
I_o — reference current density
T — absolute temperature
E_a — apparent activation energy
R — ideal gas constant

To derive a confidence intervals for the apparent activation energy, E_a, and the reference current density, I_o, of the Arrhenius expression, Eq. (4-2), the following approach was implemented. All possible subsets, with at least 2 points, of the set of 5 points in Figure 4-10(a) were determined (a set of 5 elements has a total of 26 subsets with at least 2 elements). Values of I_0 and E_a were computed for each of the 26 subsets via a linear fit. The discrete cumulative distribution function of the set of 26 values of the activation energy is included in Figure 4-10(b). Figure 4-10(b) also displays a normal cumulative distribution function fit (derived via least-squares) to the set of 26 points. From the continuous normal distribution, it is derived a mean apparent activation energy of 44.7 kJ mol^{-1} [10.7 kcal mol^{-1}] with a standard

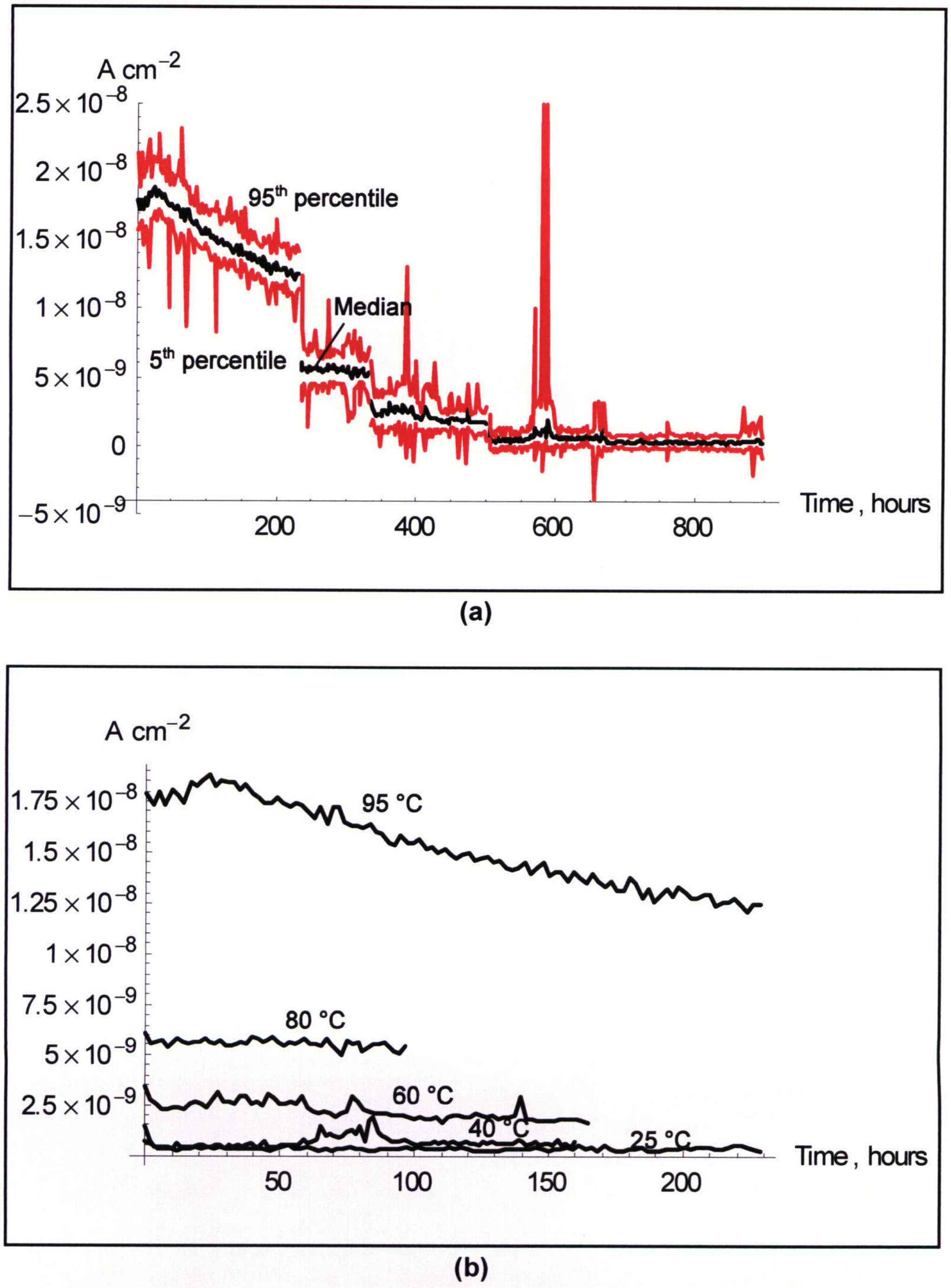

Figure 4-9. Current Density Versus Time for the 1,000-ppm [0.028-M] Chloride Electrolyte System. The Temperature Was Decreased at Defined Times in the Order 95, 80, 60, 40, and 25 °C [203, 176, 140, 104, and 77 °F]. (a) Envelope Lines: 5th- and 95th-Percentile Bounds (Bounds Computed from Sets of ~40 Adjacent Points). Middle Line: 50th Percentile Line. (b) Same Median Lines as Those in (a), But with the Time Axis Shifted So the Time of Temperature Transition Coincides with the Origin. The Representation in (b) Is Intended to Enhance the Visualization of the Effect of the Temperature on the Passive Current Density.

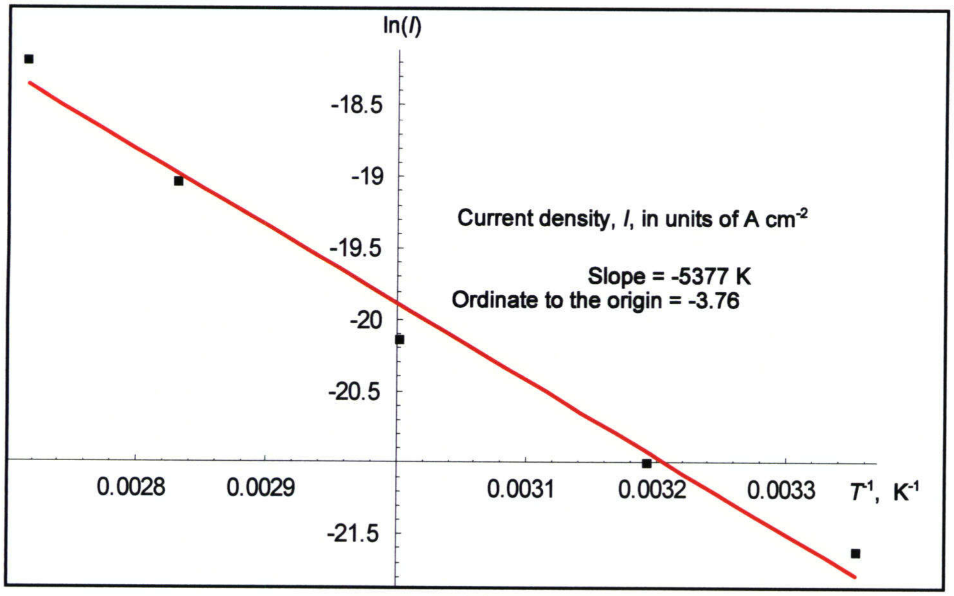
ln(*I*)
-18.5
-19
-19.5
-20
-20.5
-21.5
0.0028
0.0029
0.0031
0.0032
0.0033
T^{-1}, K^{-1}
Current density, *I*, in units of A cm^{-2}
Slope = -5377 K
Ordinate to the origin = -3.76

(a)

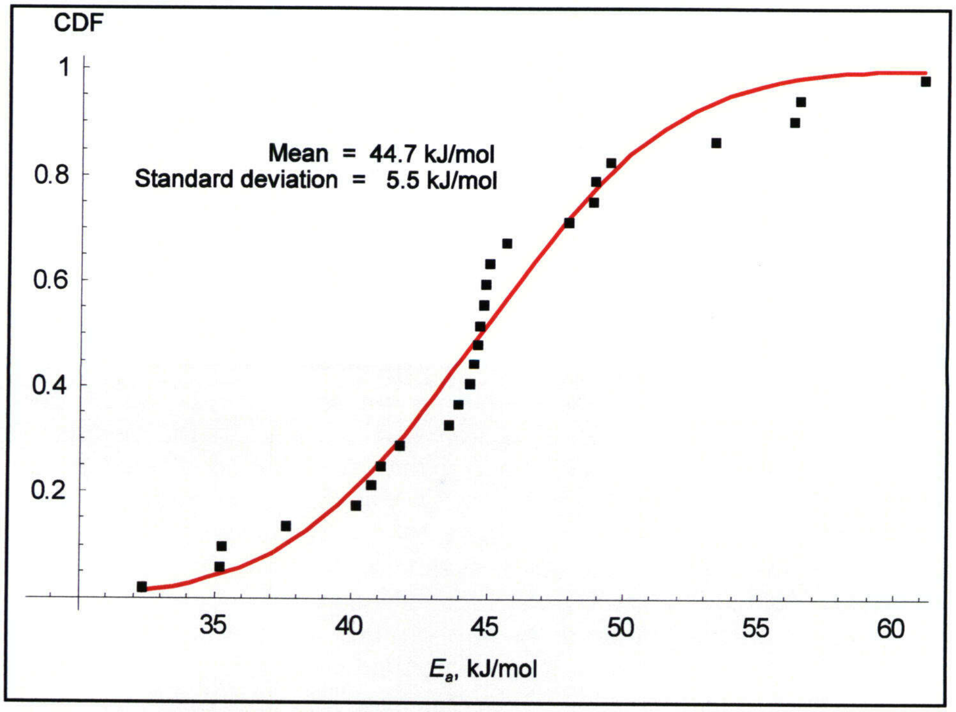
CDF
1
0.8
0.6
0.4
0.2
35
40
45
50
55
60
E_a, kJ/mol
Mean = 44.7 kJ/mol
Standard deviation = 5.5 kJ/mol

(b)

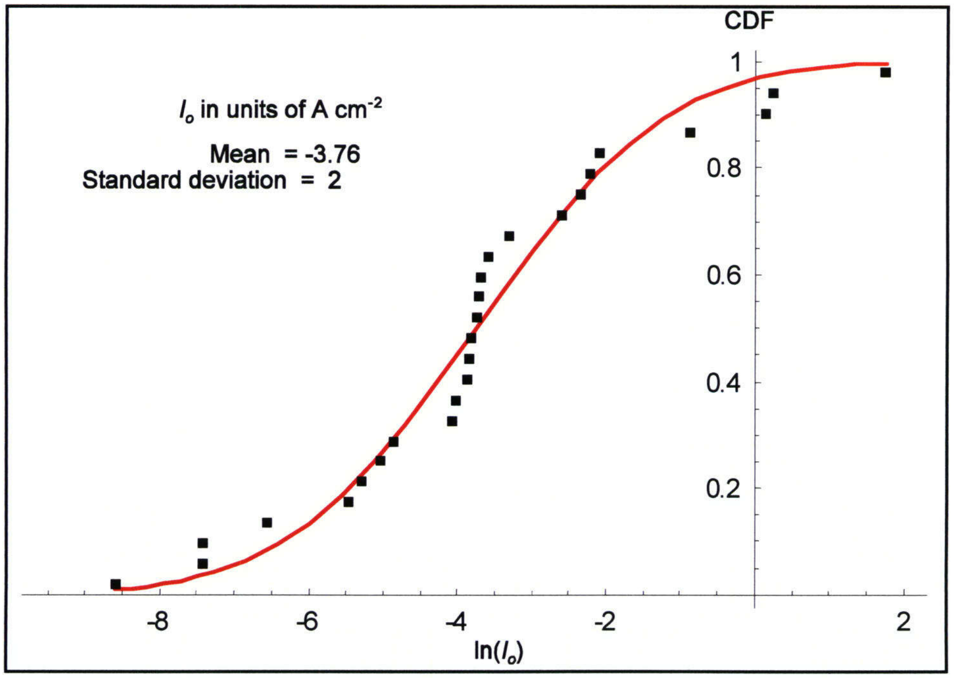

(c)

Figure 4-10. (a) Logarithm of the Passive Current Density Versus the Inverse of the Temperature. The Five Points Were Selected as an Average of the Last Few Points for Each Line in Figure 4-10(b). The Continuous Line Is the Best Linear Fit. (b) Cumulative Distribution Function for the Set of All Possible values of E_a That Can Be Computed with the Data Points in (a). (c) Cumulative Distribution Function for the Set of All values of $\ln(I_o)$ That Can Be Computed with the Data Points in (a). Values of the Mean and Standard Deviation of the best Continuous Distribution Fits are Indicated in Plots (b) and (c).

deviation of 5.5 kJ mol^{-1} [1.3 kcal mol^{-1}] over the temperature range of 25 to 95 °C [77 to 203 °C]. Figure 4-10(c) shows a normal cumulative distribution function superposed to a discrete cumulative distribution function for $\ln(I_o)$. The mean and standard deviation of the normal distribution are -3.76 and 2, respectively if I_o is expressed in units of A cm^{-2}. The relatively narrow confidence interval for E_a is the result of the use of the median values of current density [see Figure 4-9 (b)] as opposed to the use of the actual scatter data. Use of the complete experimental data would result in broader standard deviations, but similar values of the mean apparent activation energy. The use of the median current densities was preferred because it offered a clean approach to the derivation of the mean and standard deviation of E_a and $\ln(I_o)$, and also because it allowed a clear identification of a linear trend of the logarithm of the current density versus the inverse of the temperature. For performance assessments, it is recommended to use the formula in Eq. (4-3) to compute an estimator of the median current density as a function of temperature

$$I = 0.023\,e^{-\frac{44.7\,\text{kJ mol}^{-1}}{RT}}\ \text{A cm}^{-2} \tag{4-3}$$

The median current density can be transformed into a median corrosion rate with the use of Eq. (3-8). It must be born in mind the existence of variability around median values. Note that the value of the apparent activation energy, 44.7 kJ mol^{-1} [10.7 kcal mol^{-1}], is typical of activation controlled ion-transfer reactions (Heusler, 1973). The apparent activation energy is related to the activation energy of the rate constants of the fundamental charge transfer reactions controlling the passive dissolution of the alloy (see Section 5.1).

In related studies for Alloy 22, using potentiostatic polarization experiments to determine the apparent activation energy, activation energies of 32 kJ mol^{-1} [7.6 kcal mol^{-1}], 36 kJ mol^{-1} [8.6 kcal mol^{-1}], and 66 kJ mol^{-1} [15.8 kcal mol^{-1}] were derived (Bechtel SAIC Company, 2001). It must be noted that to determine a precise temperature dependence, it is necessary to allow the system to evolve toward steady state, which could be a lengthy process depending on the temperature. At temperatures of 100 °C [226 °F], it can take more than 2 weeks for steady state to be established. If steady state is not achieved, the estimated apparent activation energy will be a function of the time at which the passive current density is measured. The high estimated value of 66 kJ mol^{-1} [15.8 kcal mol^{-1}] in Bechtel SAIC Company (2001) could have been caused by the use of nonsteady state current densities and of nondeaerated solutions, which impede the separation of the anodic from the cathodic processes (tests were performed on air-aged Alloy 22 crevice specimens at pH levels of 2.75 and 7.75 and temperatures of 80, 85, and 95 °C [176, 185, and 203 °F], with nondeaerated aqueous environment containing LiCl, Na_2SO_4, and $NaNO_3$, with [Cl^-] versus [SO_4^{2-}] + [NO_3^-] ratios of 10 to 1 and 100 to 1). It is recommended, therefore, to verify the reproducibility of the apparent activation energy by varying the temperature from low to high and by using other independent electrochemical tests.

5 MODEL FOR THE PASSIVE DISSOLUTION OF NICKEL-CHROMIUM-MOLYBDENUM ALLOYS

A mechanistic model for the passive dissolution of nickel-chromium-molybdenum alloys, of which Alloy 22 is a particular case, was developed. Numerical results of the model are discussed as well as implications to long-term dissolution of Alloy 22. Other possible mechanisms to explain the experimental data are discussed also.

5.1 Model Development

The proposed model is intended to describe the passive dissolution of nickel-chromium-molybdenum alloys. The model is based on the Point Defect Model (Macdonald, 1992), which was formulated to develop a mechanistic understanding of passivity and passivity breakdown of metals in low temperature aqueous systems. The passive dissolution of Alloy 22 is assumed controlled by the formation of a protective chromium-oxide-rich film as an inner layer on the metal surface. The outer layer is believed not responsible for the passive behavior, because precipitated oxides are usually porous allowing electrolyte transport (Evans, 1978). The conduction through the chromium-oxide film is assumed to occur mainly by interstitial cations, oxygen vacancies, or by both carriers (see Appendix A for a justification of this assumption). We assume that the chromium-oxide film, lacking high proportions of molybdenum, contains chromium, nickel, and molybdenum as interstitial defects, nickel as a substitutional defect, and oxygen and chromium vacancies. The assumption of low content of molybdenum in the inner oxide layer is supported by experimental studies using Auger electron spectroscopy on alloys such as Alloy C-4 (Ni-16Cr-16Mo) (Lorang, et al., 1990) and other alloy types (Lumsden and Staehle, 1976) and also by recent studies that have found molybdenum only in the secondary layer of the oxide (Waste Package Materials Peer Review Panel, 2002). It is possible, however, that molybdenum exists as a substitutional defect in the primary layer. Because the contribution of molybdenum to the passive current density in Alloy 22 is small compared with the contributions of nickel and chromium, and because of the negligible content of molybdenum in the oxide layer, the conduction mode through the film assumed for molybdenum is not significant with respect to model computations of passive dissolution.

We extended the fundamental charge-transfer reactions at the metal-film and film-solution interfaces used to study binary alloys (Zhang and Macdonald, 1998) to ternary systems, including reactions for the injection of interstitial species to the oxide lattice at the metal-film interface. At the metal-film interface, the following reactions are postulated to describe the dissolution process

$$\mathrm{Cr} \xrightarrow{k_1^{\mathrm{Cr}}} \mathrm{Cr}_i^{\chi+} + \mathrm{V}_m + \chi e^- \qquad (5\text{-}1)$$

$$\mathrm{Mo} \xrightarrow{k_1^{\mathrm{Mo}}} \mathrm{Mo}_i^{\xi} + \mathrm{V}_m + \xi e^- \qquad (5\text{-}3)$$

$$\mathrm{Ni} \xrightarrow{k_1^{\mathrm{Ni}}} \mathrm{Ni}_i^{\delta} + \mathrm{V}_m + \delta e^- \qquad (5\text{-}2)$$

$$\mathrm{Cr} + \mathrm{V}_{\mathrm{Cr}}^{\chi-} \xrightarrow{k_2^{\mathrm{Cr}}} \mathrm{Cr}_{\mathrm{Cr}} + \mathrm{V}_m + \chi\, e^- \qquad (5\text{-}4)$$

$$\mathrm{Cr} \xrightarrow{k_3^{\mathrm{Cr}}} \mathrm{Cr}_{\mathrm{Cr}} + \frac{\chi}{2}\mathrm{V}_{\mathrm{o}}^{2+} + \chi e^- \qquad (5\text{-}6)$$

$$Ni + V_{Cr}^{\chi-} \xrightarrow{k_2^{Ni}} Ni_{Cr}^{\delta-\chi} + V_m + \delta e^- \qquad (5\text{-}5)$$

$$Ni \xrightarrow{k_3^{Ni}} Ni_{Cr}^{\delta-\chi} + \frac{\chi}{2} V_o^{2+} + \delta e^- \qquad (5\text{-}7)$$

where

χ, δ, ξ — oxidation states of chromium, nickel, and molybdenum in the oxide film
Cr_{Cr} — chromium in the chromium oxide lattice
$Ni_{Cr}^{\delta-\chi}$ — substitutional nickel in the chromium oxide lattice
$Cr_i^{\chi+}$ — chromium interstitial in the oxide
$Ni_i^{\delta+}$ — nickel interstitial in the oxide
$Mo_i^{\xi+}$ — molybdenum interstitial in the oxide
V_o^{2+} — oxygen vacancy in the oxide film
$V_{Cr}^{\chi-}$ — cation vacancy in the oxide film
V_m — metal vacancy in the alloy
e^- — electrons released by the charge transfer reactions
k — rate constants (subscripts and superscripts are used to differentiate among the different reactions and species)

At the film-solution interface, the reactions envisioned are

$$Cr_i^{\chi+} \xrightarrow{k_4^{Cr}} Cr^{\chi+} \qquad (5\text{-}8)$$

$$Ni_i^{\delta+} \xrightarrow{k_4^{Ni}} Ni^{\delta+} \qquad (5\text{-}9)$$

$$Mo_i^{\xi+} \xrightarrow{k_4^{Mo}} Mo^{\xi+} \qquad (5\text{-}10)$$

$$Cr_{Cr} \xrightarrow{k_5^{Cr}} Cr^{\chi+} + V_{Cr}^{\chi-} \qquad (5\text{-}11)$$

$$Cr_{Cr} \xrightarrow{k_5^{Cr}} Cr^{\chi+} + V_{Cr}^{\chi-} \qquad (5\text{-}12)$$

$$V_o^{2+} + H_2O \xrightarrow{k_6} O_O + 2H^+ \qquad (5\text{-}13)$$

$$\left[Cr_{1-y}Ni_yO_{\chi/2}\right]^{y(\delta-\chi)} + \chi H^+ \xrightarrow{k_7} (1-y)Cr^{\chi+} + yNi^{\delta+} + \frac{\chi}{2}H_2O \qquad (5\text{-}14)$$

where

$Cr^{\chi+}$ — chromium ion in solution
$Ni^{\delta+}$ — nickel ion in solution
$Mo^{\xi+}$ — molybdenum ion in solution
H^+ — hydrogen ion in solution
O_O — oxygen in the oxide lattice
H_2O — water molecule
$[Cr_{1-y}Ni_yO_{\chi/2}]^{y(\delta-\xi)}$ — stoichiometric composition of the oxide in proximity with the film-solution interface

and

$$y = \frac{[\mathrm{Ni}]}{[\mathrm{Ni}] + [\mathrm{Cr}]} \qquad (5\text{-}15)$$

The symbol y represents the fraction of nickel cations at the film-solution interface (i.e., where the concentrations, $[X]$, are computed at the film-solution interface). By invoking charge balance at the metal-film interface, an expression for the current density is derived (see also Appendix A for additional derivation details)

$$I \approx F\left[\chi\, a_{\mathrm{Cr}}\left(k_1^{\mathrm{Cr}} + k_3^{\mathrm{Cr}}\right) + \delta\, a_{\mathrm{Ni}}\left(k_1^{\mathrm{Ni}} + k_3^{\mathrm{Ni}}\right) + \xi\, a_{\mathrm{Mo}}\, k_1^{\mathrm{Mo}}\right] \qquad (5\text{-}16)$$

The current density, I, is a linear combination of a_{Cr}, a_{Ni}, and a_{Mo} (the alloy atomic fractions at the metal-film interface). In deriving Eq. (5-16), the rate of charge transport of cation vacancies (associated to the k_2 kinetic parameters) through the oxide film was assumed to be negligible with respect to the rate of interstitial and oxygen vacancy transport through the oxide (these latter rates were associated to the k_1 and k_3 kinetic parameters). See Appendix A for a more detailed derivation of Eq. (5-16) and additional explanation of why charge transfer through the oxide via cation vacancies is believed negligible with respect to charge transfer via cation interstitials and oxygen vacancies. The electrochemical heterogeneous reactions at the interfaces were assumed to be the rate-limiting processes as opposed to charge transport through the film. In other words, charge transport through the film was assumed to be sufficiently fast, which is an appropriate assumption for the action of a high field in a thin oxide film (nanometers thick). Consistent with the Point Defect Model, the rate constants k_1 and k_3 are functions of the local potential drop at the metal-film interface. Using the formalism of the Point Defect Model, (assuming a steady oxide film) the metal-film potential drop can be shown to be a constant if the oxidation state of the metal atoms in the film is the same as the oxidation state of the ions in solution (see Appendix A for a detailed derivation of this statement). Therefore, because the rate constants k_1 and k_3 are independent of the applied potential, Eq. (5-16) predicts a passive current density independent of the applied potential. This conclusion ceases to be valid at high applied potentials, in the regime of transpassive dissolution, where chromium can undergo a change in oxidation state from Cr(III) in the film to Cr(VI) in solution.

Equation (5-16) is consistent with experimental results indicating that the passive current density for Alloy 22 is independent of the applied potential over a wide range (up to the potential for transpassive dissolution) and also independent of environmental conditions such as pH and chloride concentration (Dunn, et al., 1999, 2000a). In Section 4.3, it was discussed that the logarithm of the current is proportional to the inverse of the absolute temperature. From the proportionality constant, we computed an apparent activation energy of 44.7 kJ mol^{-1} [10.7 kcal mol^{-1}]. This apparent activation energy is associated with the activation energy of the rate constants of the fundamental charge transfer reactions (i.e., k_1^A and k_2^A; A=Ni, Cr, Mo). The value 44.7 kJ mol^{-1} [10.7 kcal mol^{-1}] is typical of activation controlled ion-transfer reactions (Heusler, 1973).

Computing the current density as a linear combination of partial reaction rates, with the alloying element concentrations as linear coefficients, has been proposed by other authors (Steigerwald and Greene, 1962; Kirchheim, et al., 1989). The partial reaction rates are usually estimated from single-metal passive current densities. Deviations from the linear relationship have been observed and rationalized by Kirchheim, et al. (1989) by suggesting that surface concentrations differ from bulk alloy concentrations. Steigerwald and Greene (1962) explained the deviations as electrochemical coupling between alloying elements. According to these authors, alloys with elements not displaying strong electrochemical coupling will satisfy the linear relationship. They postulate that the electrochemical behavior of elements in heterogeneous alloys is not affected by the alloy mixture, but for homogeneous alloys (i.e., solid solutions), electrochemical coupling influences the magnitude of the passive current density. Steigerwald and Greene (1962) proposed two different equations to estimate the passive current density of alloys from passive current densities of single metals for heterogeneous and homogeneous alloys. The heterogeneous alloy equation is consistent with the linear relationship derived from the Point Defect Model. It is also possible that deviations observed by Steigerwald and Greene (1962) and by Kirchheim, et al. (1989) are caused by different mechanisms of charge transport through the oxide in alloys and single-metal systems. For example, nickel-cation vacancies are the predominant charge carriers in nickel oxide (Macdonald, 1992). On the other hand, transport of nickel cations through Cr_2O_3 (formed on nickel-chromium alloys of high chromium content) possibly occurs as interstitials. Thus, the passive current density measured on nickel would yield no information on the partial kinetic rates associated with nickel dissolution in nickel-chromium alloys of high chromium content. On the other hand, it is valid to use the chromium passive current density to estimate kinetic rates associated with the dissolution of chromium in nickel-chromium alloys, because the transport of chromium cations is similar in the single-metal and alloy systems.

Based on the observation that the passive current density decreases with increasing chromium content in nickel-chromium alloys (Tikkanen and Hyvärinen, 1969), it can be concluded that

$$k_1^{\mathrm{Cr}} + k_3^{\mathrm{Cr}} < k_1^{\mathrm{Ni}} + k_3^{\mathrm{Ni}} \tag{5-17}$$

Equation (5-17) implies that in the relatively short term, preferential dissolution of nickel with respect to chromium occurs through the chromium-rich passive oxide film. This theoretical observation is consistent with the short-term results reported by Cavanaugh, et al. (1983). Kirchheim, et al. (1989) observed transient preferential dissolution in iron-chromium alloys, however, these authors reported congruent dissolution after steady state was achieved. The evolution toward congruent dissolution is treated in Section 5.2.3. Under steady-state constraints, assuming the rate constants k_2^{Ni} and k_2^{Cr} are negligible, the ratio y can be computed equivalent to

$$y \approx \frac{a_{\mathrm{Ni}}\, k_3^{\mathrm{Ni}}}{a_{\mathrm{Cr}}\, k_3^{\mathrm{Cr}} + a_{\mathrm{Ni}}\, k_3^{\mathrm{Ni}}} \tag{5-18}$$

Because by hypothesis, $y << 1$, if $k_3^{Ni} > 0$ then, $k_3^{Cr} > k_3^{Ni}$. The inequality $k_3^{Cr} > k_3^{Ni}$ arises from the requirement of the film to be predominantly composed of Cr_2O_3. It is also feasible that $k_3^{Ni} = 0$ and $k_3^{Cr} \geq 0$. The cases $k_3^{Ni} = 0$ and $k_3^{Cr} > 0$ are associated with a film of Cr_2O_3 with no nickel content. The case $k_3^{Cr} = k_3^{Ni} = 0$ corresponds to a film with no formation and dissolution of the film (i.e., necessarily $k_7 = 0$). Equation (5-18) is meaningless in this instance. The case $k_3^{Cr} > 0$ corresponds to a Cr_2O_3 film that exists in a metastable state, with continuous film formation at the metal-film interface and film dissolution at the film-solution interface.

Because, in general, $k_3^{Cr} \geq k_3^{Ni}$ (requirement necessary to have $y<<1$), the inequality in Eq. (5-17) implies that $k_1^{Ni} > k_1^{Cr}$. Therefore, the rate of nickel interstitial transport through the oxide film is predominant over the rate of chromium interstitial transport. In general, we believe interstitial transport through the film is predominant over oxygen vacancy transport, although both modes are potential contributors to the overall film conductivity. The topic of the predominance of interstitial transport is addressed in Section 5.4.1.

Some implications of the model are discussed as follows. If interstitials are the dominant means of charge transport through the film, according to the postulated fundamental charge transfer reactions at the metal-film interface, injection of interstitials into the film is accompanied by the creation of vacancies in the alloy. These vacancies are usually neglected in descriptions of passivity using the Point Defect Model because it is assumed they annihilate at imperfections in the metal. Vacancies can be destroyed at interfacial misfit and misorientation dislocations (Rapp, 2001). Although the annihilation is feasible, in this report it is proposed the accumulation of vacancies at the metal-film interface could be responsible for the observed decrease of the passive current density, under potentiostatic conditions, within 2 weeks and possibly longer, as shown in Figure 4-4.

Vacancy injection as a result of the oxidation process has been inferred for high-temperature gaseous systems {~1,000 °C [1,832 °F]}. In the 1950s and 1960s it was suggested that the loss of adhesion between scale and particular steels was caused by condensation of vacancies at the interface injected by the oxidation process. Dunnington, et al. (1952) and Tylecote and Mitchell (1960) were able to maintain scale adhesion for longer periods by drilling holes in steel specimens near the metal surface to act as artificial vacancy sinks. Hancock and Fletcher (1966) noted grain boundary voids in nickel after oxidation, which they attributed to the condensation of vacancies injected by the oxidation process. Stringer (1966) suggested that the improvement in adhesion of Cr_2O_3 scales after rare-earth additions was because these additions acted as vacancy sinks in the system. Stringer (1977) suggested that in any system in which metal dissolution proceeds by transport of cation vacancies through the film, it is necessary to accommodate the reducing metal volume by losing contact between metal and oxide, plastic flowing of the oxide to maintain contact with the shrinking metal, or forming a void within the metal. According to Stringer (1977), vacancy injection provides a reasonable mechanism for these processes to occur.

At lower temperatures, vacancy injection is a feasible phenomenon as well. For example, Berghezan, et al. (1961) and Dobson and Smallman (1966) used the concept of vacancy injection to explain the growth of dislocation loops in zinc. The oxidation of zinc at room temperature occurs by creating interstitial-vacancy pairs (like the proposed model for Alloy 22) at the oxide-metal interface, with subsequent transport of interstitials toward the film-environment interface and diffusion of vacancies away from the interface to be absorbed by dislocation loops and other vacancy sinks in the metal.

For the particular case of nickel-chromium alloys, the conclusion of vacancy injection on the basis of the Point Defect Model is consistent with studies of nickel-chromium alloys of both high and low chromium content (Shida, et al., 1981; Stott, et al., 1981; Douglass, 1968) and nickel (Hales and Hill, 1972) oxidized in air at high temperatures {>1,000 °C [1, 832 °F]}. It must be born in mind that our passive dissolution model for nickel-chromium-molybdenum alloys is based on models to study low temperature aqueous systems. Vacancy injection should be evaluated further in regard to potential implications for long-term extrapolation.

5.2 Finite Difference Model

Constitutive equations and mass conservation equations for the transport of vacancies and atoms in the alloy were developed. Boundary conditions, allowing the one-dimensional integration of the differential form of the mass conservation equation, are presented. This section is concluded with a comparison of the computed passive current density as a function of time to experimental data.

5.2.1 Model Implementation

The congruent dissolution assumption is commonly found in developing passivity models (e.g., Kirchheim, et al., 1989, 1990; Steigerwald and Greene, 1962). Furthermore, for those models incorporating a description of the transport of charged species within the film and atoms within the alloy, it is commonplace to assume the rate of the ejection of cations from the metal into the film—a rate determined by the interfacial kinetics—is equal to the cation transport rate from the bulk of the alloy to the interface—a rate controlled by solid-state diffusion (e.g., Zhang and Macdonald, 1998). Equating kinetically controlled rates to transport-controlled rates is valid only under steady-state conditions. Thus these models cannot tell whether steady-state occurs and if it does occur, then what is the magnitude of the steady-state current density (i.e., current densities are usually an input to these models rather than an output).

We assume that standard rate constants are consistent with nickel dissolving preferentially with respect to chromium and molybdenum, at least during short periods. This assumption is derived from a theoretical requirement and seems consistent with experiments by Cavanaugh, et al. (1983). The validity of this assumption requires additional experimental support. However, we do not require the kinetic and diffusive rates to be equivalent, and, thus, the model can be used to gain additional insight on the magnitude of the steady-state passive anodic current density.

The passive oxide film is assumed at steady state (i.e., constant thickness and composition) at all times. This assumption is valid because the time constant of the solid-state transport process is much larger than the time constant associated with the kinetic processes leading to the formation of the oxide film. It may be argued that films continue growing during extended periods; however, the main mechanisms for the extended growth of films at low temperatures are possibly dissolution and precipitation. Precipitated oxides are not necessarily protective

(Evans, 1978) and are believed not responsible for the phenomenon of passivity. The oxide layer in immediate contact with the metal, a protective chromium oxide film, is considered the main responsible for the phenomenon of passivity. This inner oxide forms immediately after the exposition of the alloy to the environment and reaches a constant thickness.

The vacancy mechanism is well established as the dominant process of diffusion in alloys (Shewmon, 1963). The constitutive equation describing the coupled diffusion process is

$$J_A = -\frac{D_A}{c_v^o}(c_v \nabla c_A - c_A \nabla c_v) = -J_v \tag{5-19}$$

where

J_A — flux of specie *A*, mol cm^{-2} s^{-1} [mol in^{-2} s^{-1}]
J_v — flux of vacancies, mol cm^{-2} s^{-1} [mol in^{-2} s^{-1}]
D_A — diffusion coefficient of specie *A*, mol cm^2 s^{-1} [mol in^2 s^{-1}]
c_v^o — equilibrium concentration of vacancies at a reference temperature, mol/cm^3 [mol/in^3]
c_A — concentration of specie *A*, mol cm^{-3} [mol in^{-3}]
c_v — concentration of vacancies, mol cm^{-3} [mol in^{-3}]

According to the constitutive Eq. (5-19) (i) the flow of vacancies is in the opposite direction to the flow of solid-state components; (ii) solid-state diffusion is enhanced by the presence of vacancies; (iii) solid state diffusion can occur in the absence of solid-state concentration gradients, but in the presence of vacancy concentration gradients, and (iv) in the absence of vacancy concentration gradients, a constitutive equation equivalent to Fick's law arises. Equivalent constitutive equations have been used elsewhere to describe the diffusion of vacancies in silicon crystals (e.g., Bracht, 2000).

For the ternary nickel-chromium-molybdenum alloy, the vacancy flux is described by

$$J_v = -J_{\mathrm{Ni}} - J_{\mathrm{Cr}} - J_{\mathrm{Mo}} \tag{5-20}$$

where $J_{\mathrm{Ni,Cr,Mo}}$ are defined as in Eq. (5-19) replacing the subscript *A* by Ni, Cr, or Mo. Combining Eqs. (5-19) and (5-20), one gets

$$J_v = -\frac{\nabla c_v}{c_v^o}(D_{\mathrm{Ni}}c_{\mathrm{Ni}} + D_{\mathrm{Cr}}c_{\mathrm{Cr}} + D_{\mathrm{Mo}}c_{\mathrm{Mo}}) + \frac{c_v}{c_v^o}(D_{\mathrm{Ni}}\nabla c_{\mathrm{Ni}} + D_{\mathrm{Cr}}\nabla c_{\mathrm{Cr}} + D_{\mathrm{Mo}}\nabla c_{\mathrm{Mo}}) \tag{5-21}$$

For the sake of mathematical simplicity, it is assumed that all diffusion coefficients are the same—equal to *D*. This assumption is consistent with experimental diffusion coefficients for nickel-chromium alloys determined at high temperatures and other binary and ternary alloys (Brandes and Brook, 1992). If it is assumed the number of sites per unit of volume in the lattice is a constant (Zhang and Macdonald, 1998); i.e.,

$$c_{\mathrm{Ni}} + c_{\mathrm{Cr}} + c_{\mathrm{Mo}} + c_v = c_T \tag{5-22}$$

(c_T is a constant), the constitutive equation for the transport of vacancies reduces to

$$J_v = -\left(D \frac{c_T}{c_v^o} \right) \nabla c_v = -D_{\mathrm{eff}} \nabla c_v \tag{5-23}$$

This constitutive equation has been used elsewhere (Gibbs and Hales, 1977) to estimate vacancy concentrations above an equilibrium value. Note that Eq. (5-23) is equivalent to Fick's law, and also that the effective diffusion coefficient, D_{eff} is greater than the solid state diffusion coefficient, D, by several orders of magnitude. For example, if the concentration of vacancies at 100 °C [212 °F] (taken as reference temperature) is approximately 10^{15} cm^{-3} [1.6×10^{16} in^{-3}] {~10^{-9} mol/cm^3 [1.6×10^{-8} mol/in^3]} and c_T is approximately equal to 0.1 mol/cm^3, the ratio c_T / c_v^o is approximately 10^8. Thus, the transport of atoms in a crystal is greatly enhanced by the presence of vacancies and vacancy gradients.

Mass conservation requires that

$$\frac{\partial c_v}{\partial t} = -\nabla \cdot J_v = D_{\mathrm{eff}} \nabla^2 c_v \tag{5-24}$$

Equation (5-24) has wider validity than dictated by the set of assumptions used to derive it. For example, without assuming a constant number of lattice sites and that the diffusion coefficients for the alloy elements are the same, but only assuming the vacancy concentration is small compared with the atom concentrations (i.e., $c_v << c_{\mathrm{Ni,Cr,Mo}}$), it can be derived that

$$\frac{\partial c_v}{\partial t} = -\nabla \cdot J_v \approx \frac{1}{c_v^o} \sum_{A=\mathrm{Ni,Cr,Mo}} D_A c_A \nabla^2 c_v = D_{\mathrm{eff}} \nabla^2 c_v \tag{5-25}$$

The effective diffusion coefficient, D_{eff}, is nearly constant if the concentration of vacancies is small. Additional details on the derivation of the constitutive equations for the mass transport problem are provided in Appendix B.

5.2.2 Boundary Conditions

From the mass conservation model reported elsewhere (Pensado, et al., 2000; Cragnolino, et al., 2001), the velocity of the metal-film boundary is, in general, negligible for a variety of estimates of rate constants consistent with experimental passive current densities. The velocity of the metal-film boundary is controlled by the rate constants k_3^{Ni} and k_3^{Cr}. For the sake of mathematical simplicity, it is considered that $k_3^{\mathrm{Ni}} = k_3^{\mathrm{Cr}} = 0$, which is equivalent to the postulate that charge transport through the film is entirely by interstitials without any contribution by oxygen vacancies. Additional thermodynamic arguments are provided in Section 5.4.1 in favor of interstitial conduction. We modeled the system as a one-dimensional system. The transport direction, x, is oriented in the direction of the propagation of the corrosion front, perpendicular to the alloy surface exposed to the electrolyte. At the metal-film interface, the rate of injection of vacancies into the alloy, r_v, is

$$r_v = \frac{1}{c_T}(k_1^{\mathrm{Ni}} c_{\mathrm{Ni}} + k_1^{\mathrm{Cr}} c_{\mathrm{Cr}} + k_1^{\mathrm{Mo}} c_{\mathrm{Mo}})\Big|_{x=0} \tag{5-26}$$

where the concentrations c_{Ni}, c_{Cr}, and c_{Mo} are computed at the metal-film interface ($x = 0$). As vacancies are injected into the alloy, the atom concentrations c_{Ni}, c_{Cr}, and c_{Mo} decrease, causing a subsequent decrease in the rate of vacancy injection at the metal-film interface and of the passive current density measured by an external circuit. The rate of injection of vacancies is defined by the alloy element concentrations at $x = 0$. Although Eq. (5-24) is an uncoupled equation, the boundary condition expressed as Eq. (5-26) is coupled to the transport of the alloy elements. Thus, the complete coupled diffusion problem for the determination of element concentrations as a function of position and time must be addressed.

The initial concentration of vacancies is equal to the equilibrium concentration $[c_v(x,t = 0) = c_v^o \cong 0)]$, and the initial element concentration is determined by the alloy composition $[c_A(x,t = 0) = c_A^o$, A = Ni, Cr, or Mo]. The mass conservation equation, Eq. (5-24), the initial conditions, and the boundary condition at $x = 0$ define a complete system of equations that can be solved numerically. From the standpoint of the characteristic distance associated with a solid-state diffusion process, the alloy can be considered a semiinfinite medium. To make the problem computationally tractable, only a small region of the alloy, close to the metal-film interface, was considered. In the numerical approach, a thin slab of the alloy of thickness L was considered. At $x = 0$, the metal-film interface, vacancies are injected as a result of the oxidation process. At $x = L$ deep into the alloy, a free boundary is constructed. Concentrations at the free boundary, of vacancies or atoms, are determined by diffusion equations, just as the concentrations at any other point $0 < x < L$. Detailed counting of the vacancies in the system at any arbitrary time allows the computation of the vacancy concentration as a function of the position. Because $x = L$ is a free boundary, the numerical results are independent of the magnitude of L, provided that enough spatial discretization is incorporated in the computations. The approach to the numerical solution is detailed in Appendix B.

5.2.3 Numerical Results

In Figure 5-1, numerical results are compared to experimental current densities in various electrolytes at 95 °C [203 °F]. The simulated curves are shown as the middle lines passing through the experimental scatter data. The envelope lines for the scatter data are the 5th and 95th percentiles of the current density. The confidence intervals were computed by dividing the time domain into 100 intervals and computing statistics (mean time, 5th, and 95th percentiles of the current density) with the points contained in each interval (approximately 40 points per interval). The parameters used in generating the simulated curves in Figure 5-1 are included in Table 5-1. The method to derive the rate constants and finite difference constants is briefly

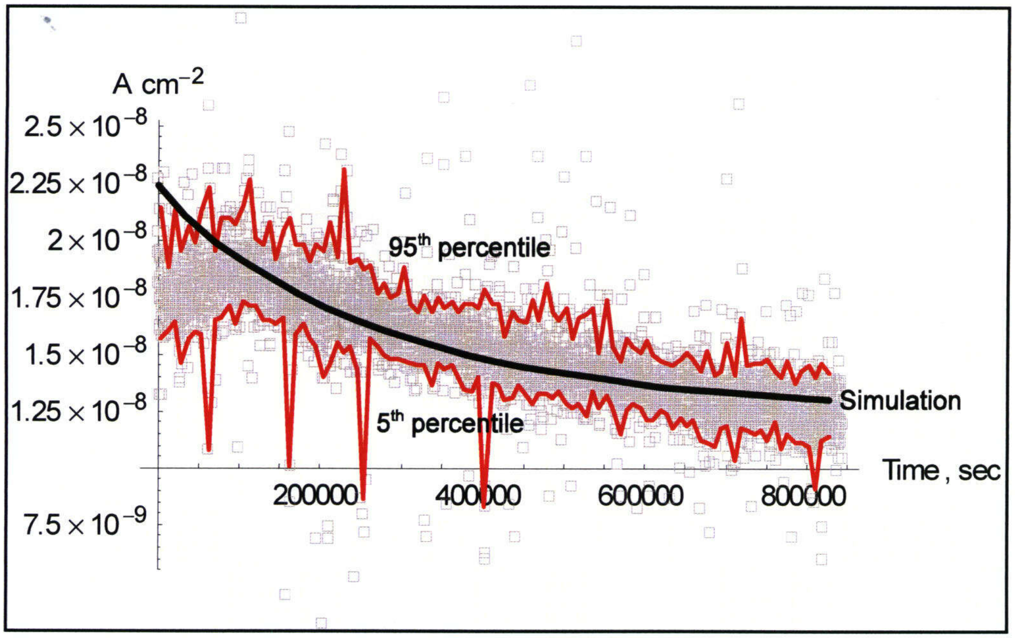
A cm^{-2}
2.5 × 10^{-8}
2.25 × 10^{-8}
2 × 10^{-8}
1.75 × 10^{-8}
1.5 × 10^{-8}
1.25 × 10^{-8}
7.5 × 10^{-9}
95th percentile
5th percentile
Simulation
200000
400000
600000
800000
Time , sec

(a)

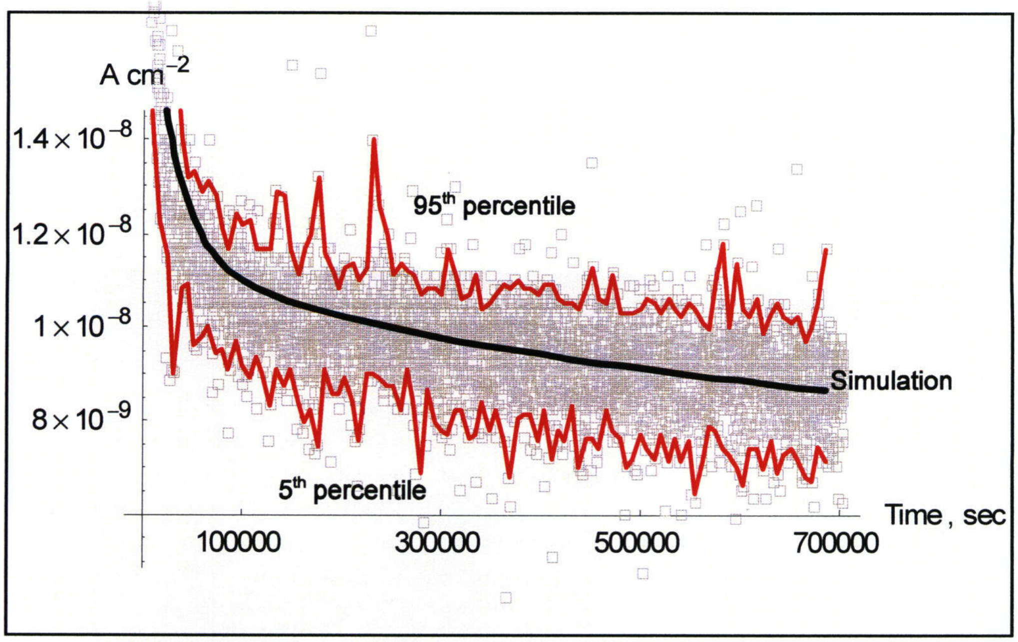
A cm^{-2}
1.4 × 10^{-8}
1.2 × 10^{-8}
1 × 10^{-8}
8 × 10^{-9}
95th percentile
5th percentile
Simulation
100000
300000
500000
700000
Time , sec

(b)

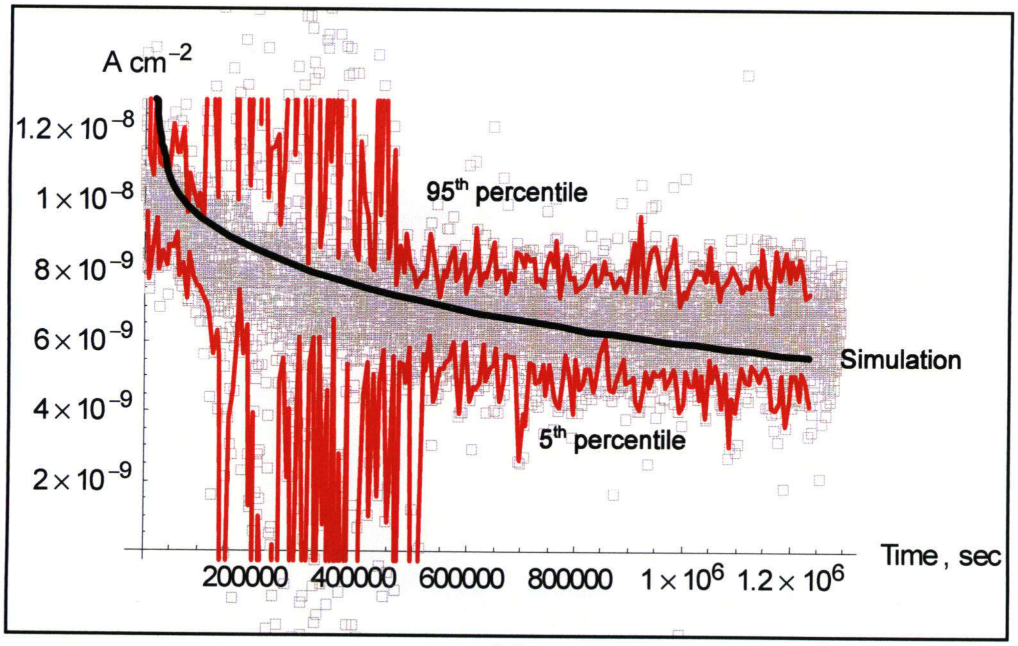

(c)

Figure 5-1. Anodic Passive Current Density Versus Time in Chloride and Chloride Plus Fluoride Electrolytes. Envelope Lines: 5th- and 95th-Percentile Bounds (Bounds Computed from Sets of ~40 Adjacent Points). Middle Lines: Results From the Finite Difference Simulations. Scatter Data: Current Densities at 95 °C [203 °F]. (a) 100 ppm (0.028 M) Cl^-, (b) 0.028 M Cl^- and 0.052 M fluoride, (c) 1,000 ppm Cl^- + 1,000 ppm SO_4^{2-}. See Table 5-1 for the Parameters Employed in the Finite Difference Simulations.

explained. It was assumed that $k_1^{\mathrm{Mo}} = 0.5\,(k_1^{\mathrm{Cr}} + k_1^{\mathrm{Ni}})$ to obtain results consistent with those reported by Cavanaugh, et al. (1983). The value of k_1^{Cr} was selected arbitrarily with the only condition that a current density computed as $\chi\, F k_1^{\mathrm{Cr}}$ (χ = 3 and F is Faraday's constant) be approximately 10^{-9} to 10^{-8} A/cm^2 [6.45×10^{-9} to 6.45×10^{-8} A/in^2], which is a reasonable value for the passive current density for the dissolution of chromium (e.g., Kirchheim, et al., 1989).

The value of k_1^{Ni} was computed by solving the equation

$$F\,\left(\chi\, a_{\mathrm{Cr}}\, k_1^{\mathrm{Cr}} + \delta\, a_{\mathrm{Ni}}\, k_1^{\mathrm{Ni}} + \xi\, a_{\mathrm{Mo}}\, k_1^{\mathrm{Mo}}\right) = I_o \qquad (5\text{-}27)$$

where the atomic fractions a_{Ni}, a_{Cr}, a_{Mo} were derived from the initial concentrations in Table 5-1, the oxidation states χ, δ, and ξ were assumed equal to 3, 2, and 6, and I_o was a selected value of the current density at t = 0 (consistent with the experimental data). The inequality in the rate constants expressed in Eq. (5-17) and other inequalities presented in the paragraph following Eq. (5-18) were used as discriminating criteria for the adequate selection of the values of the rate constants.

Table 5-1. Parameters Used in Generating the Simulated Curves in Figure 5-1.

Parameter	Figure 5-1(a)	Figure 5-1(b)	Figure 5-1(c)	Description of Parameter
k_1^{Ni} [mol/(s cm^2)]	1.35×10^{-13}	1.19×10^{13}	1.19×10^{-13}	Rate of injection of nickel interstitials
k_1^{Cr} [mol/(s cm^2)]	2.07×10^{-14}	2.07×10^{-14}	2.07×10^{-14}	Rate of injection of chromium interstitials
k_1^{Mo} [mol/(s cm^2)]	7.8×10^{-14}	6.97×10^{-14}	6.97×10^{-14}	Rate of Injection of molybdenum Interstitials
D_{eff} [cm^2/s]	4.78×10^{-17}	6.34×10^{-19}	1.88×10^{-19}	Effective diffusion coefficient for vacancy transport in the bulk of the alloy
Δx [cm]	9.55×10^{-8}	9.1×10^{-9}	5.4×10^{-9}	Characteristic distance of the finite difference computations. It can also be interpreted as the interface thickness

Common Parameters

$c_{Ni}(t = 0) = 0.086$ mol/cm^3 $c_{Cr}(t = 0) = 0.036$ mol/cm^3 $c_{Mo}(t = 0) = 0.012$ mol/cm^3 $c_V(t = 0) = 0$	Initial concentrations
$\lambda = D_{eff}\, \Delta t/(\Delta x^2) = 0.5$	Dimensionless parameter of the finite difference diffusion equation; see Appendix B.

Note: English equivalents are not provided because this table contains only values used in the numerical simulations.

As explained in Appendix B, simulations having identical values of the parameter λ (defined in Table 5-1) and the ratio $D_{eff}/\Delta x$ yield identical concentrations. An adequate value of the ratio $D_{eff}/\Delta x$ was selected by trial and error, and λ was maintained invariant equal to 0.5 (value selected to guarantee convergence). The magnitude of the effective diffusion coefficient, D_{eff}, and the spatial time step, Δx, were proportionally adjusted to obtain an adequate reproduction of the experimental time scale. This last step is the mathematical equivalent to stretching the time scale until the simulated current density resembles the experimental data. It was requested that the resulting values of the effective diffusion coefficient, D_{eff}, and the spatial step, Δx, would make physical sense. Δx can be interpreted as the "thickness" of the metal-film interface, which should be Angstroms or fraction of Angstrom thick. It is acknowledged that the parameters reported in Table 5-1 are not the only selections consistent with the experimental data. This is a positive aspect, because it is possible to construct a theory consistent not only with passive current densities but also with the evolution of the alloy concentration profile as a function of time. At this time, only incomplete information is available and unique determination of rate constants and diffusion coefficients is not possible.

Figure 5-1 notes that experimental current densities display a small but steady monotonic decrease in time, with the exception of the current density in Figure 5-1(c), which seems to have achieved steady state at the end of the experiment. The decrease in time is explained as due to the accumulation of vacancies at the metal-film interface. The model does not account for initial oxide formation and stabilization of the system. It is thus surprising the good agreement between the simulation and the experimental data in Figure 5-1(b) for times less than 10^5 seconds. The early divergence between simulated currents and experimental data at times less than 10^5 seconds for Figures 2(a) and (b) was expected.

The model does not incorporate any vacancy annihilation process; however, it is anticipated the existence of a saturation concentration value above which vacancies are annihilated. The saturation concentration value could be a function of the vacancy sink density and temperature. Decrease in the current density stops when the saturation concentration is reached. Additional vacancies injected into the system are destroyed with the subsequent volume contraction and displacement of the metal-film boundary with respect to a fixed reference frame. Therefore, the model ceases to be valid when the vacancy saturation value is reached. In Figure 5-1(c), it is apparent that after approximately 6×10^5 seconds, the average current density ceases to decrease; however, the simulated current density continues decreasing (i.e., the breaking point of the validity of the model is reached). It could be arguably concluded the vacancy concentration reaches saturation after roughly 6×10^5 seconds at 95 °C [203 °F].

The model can also be used to estimate concentration profiles within the bulk of the alloy until the vacancy saturation value is reached and also to judge whether or not nonstoichiometric dissolution can be sustained for relatively extended periods. Figure 5-2 includes concentration profiles at two different times for the case (b) in Figure 5-1. Concentration profiles for cases (a) and (c) in Figure 5-1 are similar and not included in this report. In Figure 5-2, the position $x = 0$ defines the metal-film interface. Vacancies are injected at the metal-film interface and move into the alloy, thus, the vacancy concentration decreases for increasing values of the position coordinate. The relative enrichment of chromium at the interface is the result of the assumption of the initial preferential dissolution of nickel with respect to chromium. (The extent of the initial noncongruency in the dissolution is controlled by the selected values of k_1^{Ni}, k_1^{Cr}, and k_1^{Mo} in the finite difference simulations. Note that in Table 5-1, $k_1^{\mathrm{Ni}} > k_1^{\mathrm{Cr}}$ and $k_1^{\mathrm{Ni}} > k_1^{\mathrm{Mo}}$.) Nickel, chromium, and molybdenum atoms are transported to the interface in approximately similar proportions to the composition of the bulk alloy, resulting in excess chromium atoms with respect to nickel. In other words, the proportion of nickel to chromium atoms injected into the oxide as interstitials is greater than the proportion of nickel to chromium atoms arriving at the metal-film interface by vacancy-enhanced diffusion at any given time-step, causing the interface to become rich in chromium and depleted of nickel. As a result of the relative enrichment of chromium at the interface, chromium dissolution is enhanced, while the rate of nickel dissolution is decreased causing the system to display stoichiometric dissolution in the relative long term. Figures 5-3 and 5-4 provide support to the statement of long-term stoichiometric dissolution.

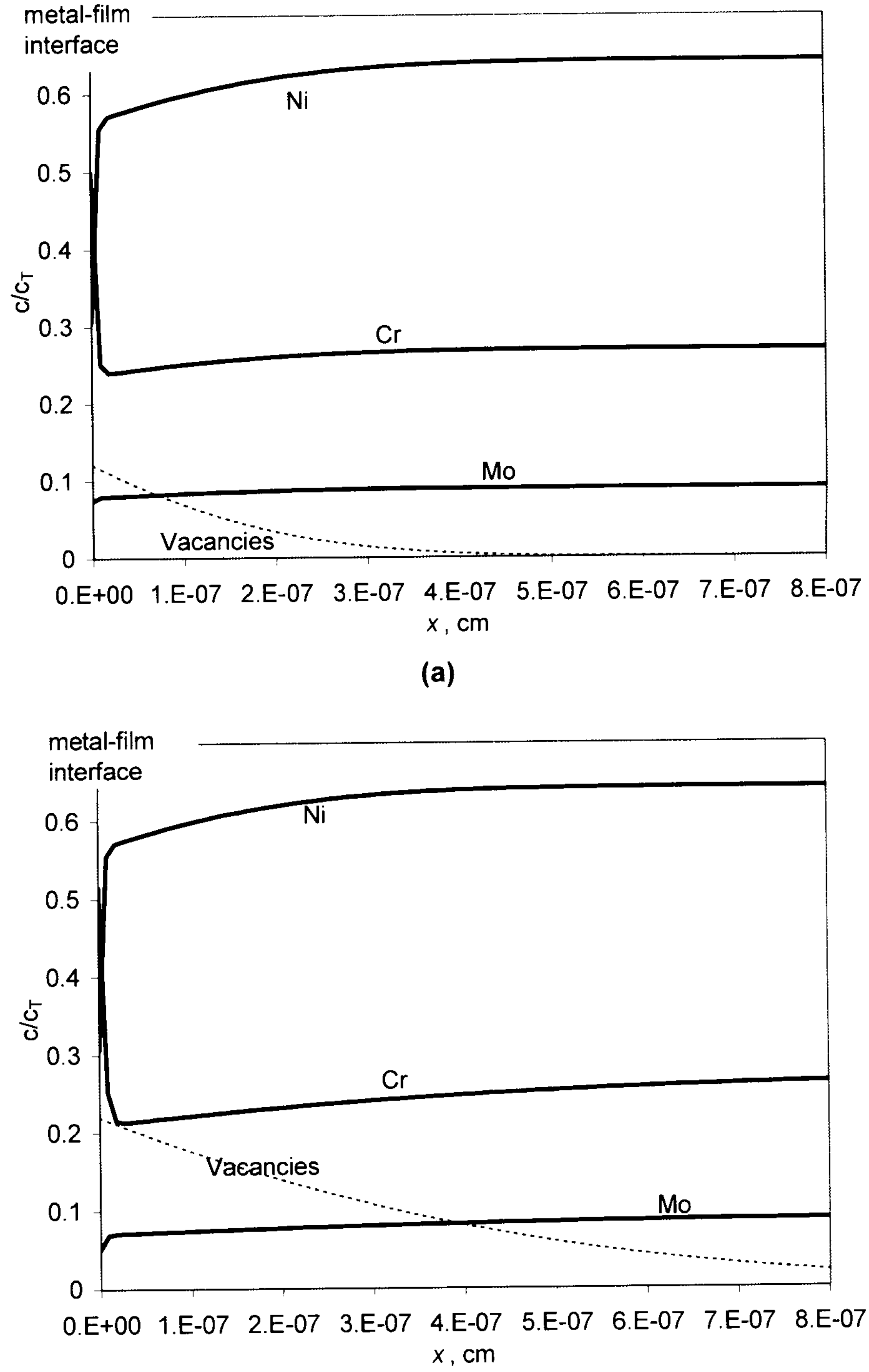

(a)

(b)

Figure 5-2. Atomic Concentration Profile [Same Simulation as in Figure 5-1(b)] (a) Concentration Profile at Time = 39,000 Seconds; (b) Concentration Profile at Time = 230,000 Seconds

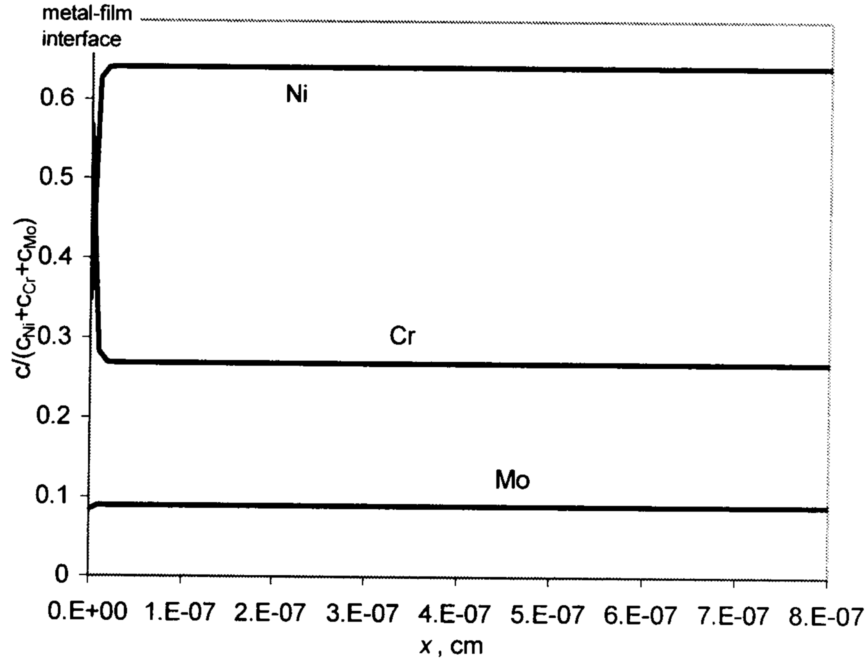

(a)

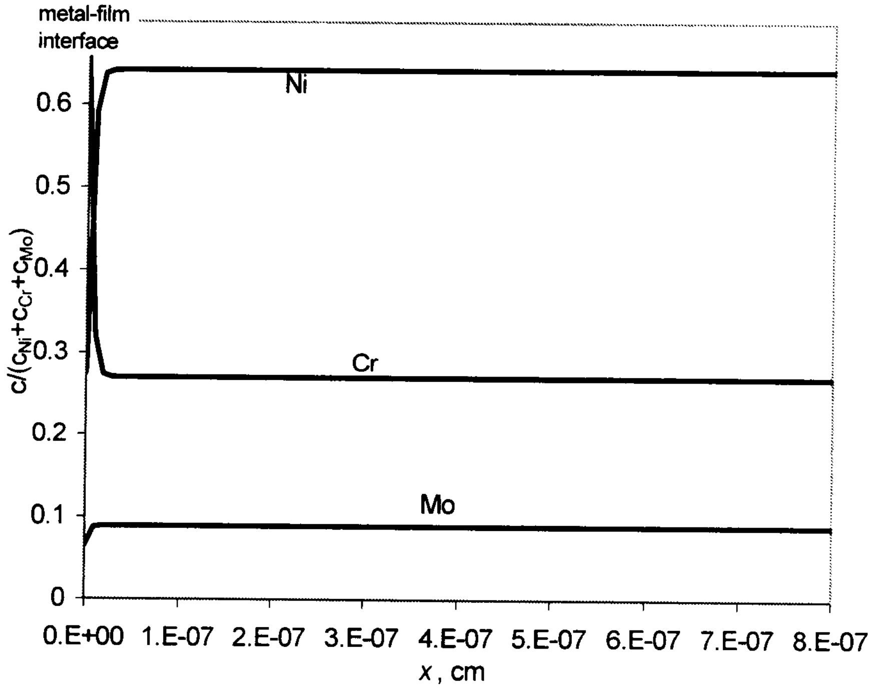

(b)

Figure 5-3. Fractional Concentration Profile or Atomic Fraction [Same Simulation as in Figure 5-1(b)]. (a) Time = 340,000 Seconds, (b) Time = 230,000 Seconds

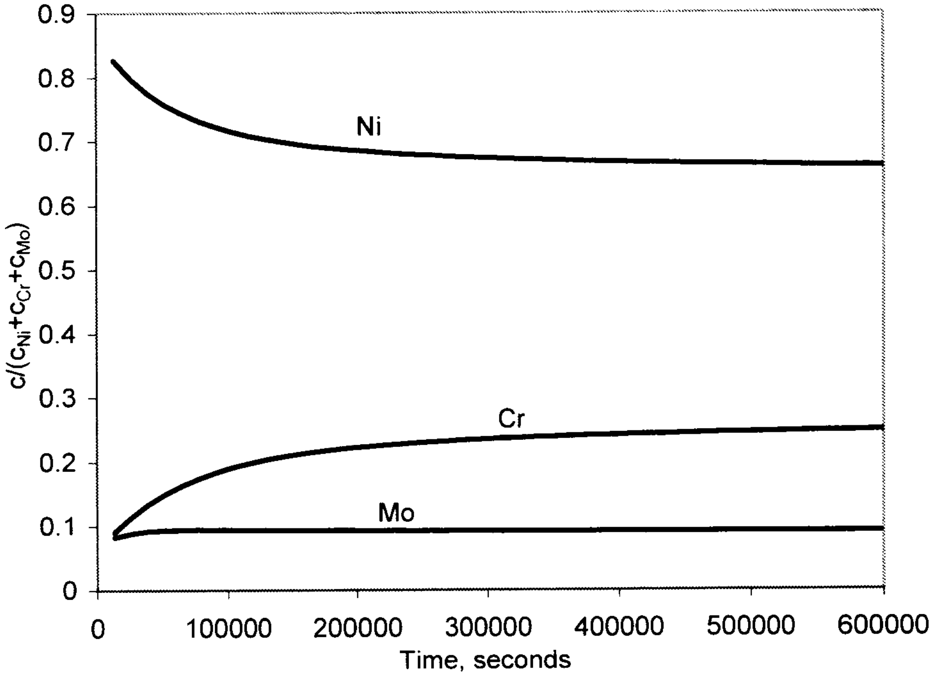

Figure 5-4. Cumulative Amount of Ions Ejected from the Alloy as a Function of Time

In Figure 5-3, atomic fractions as functions of the spatial coordinate at two different times are displayed. Deviations from the bulk fraction occur only at the metal-oxide interface. The relative enrichment of chromium with respect to nickel results from the assumption that the rate constant for nickel dissolution is higher than the rate constant for chromium dissolution (see Table 5-1). Because, in general, the atomic fraction does not significantly deviate from bulk values, it follows that dissolution becomes stoichiometric as time elapses. To prove this assertion, Figure 5-4 includes the cumulative amount of ions ejected from the alloy as a function of time (the solubility of some ions is small, thus, it would be incorrect to refer to the ions ejected from the alloy as ions in solution). The cumulative fractions tend toward the stoichiometric values dictated by the initial alloy composition as time proceeds. Initially, an excess of nickel to chromium ions in the system compared with bulk alloy values is produced. This result is consistent with results by Cavanaugh, et al. (1983) reporting preferential dissolution of nickel with respect to chromium for Alloy C-276 (Ni-16Cr-16Mo-4W-5Fe, which is an alloy similar to Alloy 22) in chloride solution for samples dissolving during short periods. Figure 5-3 is also consistent with observations by Kirchheim, et al. (1989) of transient preferential dissolution in iron-chromium alloys, but the establishment of congruent dissolution after reaching steady state. It is concluded that the dissolution process is regulated by solid-state transport in the alloy. It must be noted that the conclusion of evolution toward stoichiometric dissolution is dependent on the assumption that the diffusion coefficients for the various elements in the alloy are similar. This assumption is consistent with experimental diffusion coefficients for nickel-chromium alloys at high temperatures (Brandes and Brook, 1992). Nonetheless, it is necessary to perform numerical experiments to study the dependence of this conclusion on the selection of the diffusion coefficients. Our transport model of diffusion enhanced by vacancies should be extended to handle the case of dissimilar diffusion coefficients.

No experimental data are available on the evolution of concentration profiles as functions of time. For the Hastelloy C-4 alloy (Ni-16Mo-16Cr), it has been reported an enrichment of nickel with respect to chromium after 2 hours of polarizing the alloy sample in the passive regime at room temperature in sodium-chloride solution (Lorang, et al., 1990). Similarly, enrichment of nickel with respect to chromium has been reported in nickel-chromium-iron alloys polarized in the passive regime at room temperature in borate solution for 2 hours (Boudin, et al., 1994). Both studies addressed the period of initial oxide formation, and the local depletion of chromium was explained as a result of the higher oxygen affinity of chromium. Chromium oxidizes preferentially, forming a chromium oxide film. After the formation of the oxide film, nickel presumably dissolves preferentially with respect to chromium leading to the relative enrichment of chromium presented in Figure 5-3. It is necessary to measure concentration profiles of alloy samples dissolving in passive conditions for extended periods. The evolution in time of concentration profiles would yield additional information on the mechanism of passive dissolution. It is acknowledged that it is challenging to unequivocally identify the location of an oxide-film interface, while at the same time measuring a concentration profile. The following section discusses implications of the model on the long-term extrapolation of passive behavior.

5.3 Discussion On Long-Term Extrapolation

An important question to address is whether mechanisms exist leading to an increase in corrosion rates that could compromise the performance of Alloy 22 as container material. The central assumptions in current approaches to long-term extrapolation have been discussed in Section 3.5. We have argued that the alloy dissolution process results in the injection of defects in the alloy (in the form of vacancies), which can be used to account for the transitory decrease in the passive current density well after formation of the chromium oxide film. The conclusion of vacancy injection agrees with high-temperature studies on the oxidation of alloys (Gibbs and Hales, 1977). At high temperatures {~1,000 °C [1,832 °F]}, the injection of vacancies during oxidation has been used to explain changes in mechanical properties in nickel-chromium alloys. For example, Hancock (1977) noted that mechanical properties such as reduction in creep-rupture life and reduction in tensile ductility are importantly influenced by high-temperature oxidation, but not affected by subjecting nickel-chromium alloys to high temperatures in an inert gas. The change in the mechanical properties was suggested by Hancock (1977) to be due to the injection of vacancies during the oxidation process.

Besides the potential effect on the mechanical properties, the injection of vacancies causes the oxide film to lose its adhesion to the metal substrate. Film spalling could occur periodically, leading to temporary free-alloy dissolution until the establishment of a new oxide film. The composition and properties of the oxide layer formed after film spalling will depend on the local composition of the alloy in the neighborhood of the metal-film interface. Chromium oxide may form again given the relative chromium enrichment at the interface (resulting from the assumption that the kinetic rate constant for nickel dissolution is greater than the corresponding rate constants for chromium and molybdenum). Independently of the content of molybdenum at the metal-film interface, MoO_4^{2-} ions would be available at the film-solution interface to inhibit potential chloride attack on the oxide (Sugimoto and Sawada, 1976). Formation of chromium oxide cannot be guaranteed, however, if the rate constant for chromium dissolution is in excess of the corresponding rate constant for nickel. In that case, a less protective nickel oxide film could temporarily develop on the surface. We argued that the numerical results reported in Figure 5-4 are consistent with experimental observations by Cavanaugh, et al. (1983) and by

Kirchheim, et al. (1989); therefore, it is appropriate to assume that the kinetic rate constant for nickel dissolution is in excess of the rate constant for chromium dissolution, and chromium oxide could be the oxide film that forms after film spalling, if it occurs.

Passive dissolution is not a coherent phenomenon. There is stochastic variability in the dissolution rate, which is evidenced in the variability of the current densities in this report. The stochastic variability of the passive dissolution and the possible long-term instability of the oxide film could potentially result in roughening of the corroding surface area as time elapses. Surface roughening has been observed for Alloy 22 (Bedrossian and Farmer, 1999). Therefore, the assumption of planar dissolution used in long-term extrapolation may not be valid. If roughening occurs, there will be points on the corroded surface lying ahead of the average corrosion front. Variability of the corrosion rates has been partially addressed by U.S. Department of Energy by splitting the surface of the waste package into patches and assigning a different corrosion rate to each patch. The variability in the corrosion rates assigned to waste package patches derives from averages from multiple weight loss coupon samples; on the other hand, the spatial variability potentially leading to surface roughening is of a much smaller (microscopic or atomic) scale.

A modeling tool is not available to estimate the penetration rate of a surface that roughens with time. Possibly, dissolution models from percolation theory could be used for that purpose. In studying dealloying problems, Sieradzki, et al. (1989) developed a model based on percolation theory to simulate the morphology of structures developed after dealloying. Dealloying and the formation of porous structures are commonplace for binary alloys composed of a reactive element (e.g., magnesium, aluminum, manganese, or zinc) and a noble element (e.g., gold, silver, copper, or nickel) and polarized at a potential such that the reactive component actively dissolves, but the noble component does not (Min and Li, 1994). For these alloy systems, a dealloying threshold exists, defined as the lowest atomic fraction of the reactive element below which the reactive element cannot be selectively dissolved from the bulk of the alloy (Sieradzki, et al., 1989). These alloy systems develop into porous structures under active dissolution (i.e., for potentials above a critical potential) and free dissolution (i.e., without the presence of a protective oxide layer), which differs from the system portrayed in this report. The percolation model ideas of the Sieradzki, et al. (1989) have been used by other authors to describe the morphology of the corrosion front underneath an oxide.[1] Percolation models rely on rather simple rules for the dissolution process. These rules determine changes in the location of atoms, or clusters of atoms, from one time-step to the next. Probabilities of transition are included in the evolution rules and are addressed by Monte Carlo analyses. Also, the coordination number (i.e., the number of neighbors and the type) is a factor considered in the formulation of transition rules. Phenomenological expressions, such as Tafel kinetics or Arrhenius equations, are introduced to construct a model consistent with empirical data. The evolution of the morphology is usually presented as a function of a dimensionless computer time, representing the number of Monte Carlo iterations. To map the computer time to a real time, it is necessary to calibrate the model to experimental data, which is challenging, not only because it is difficult to decide when two morphologies are equivalent, but also because it is

---

[1] Roux, F., J. Stafiej, A. Chaussé, and J.P. Badiali. "Numerical Simulations of Simple Processes Associated with Corrosion, Diffusion, and Formation of a Passive Layer." Proceedings from the International Workshop on Prediction of Long-Term Corrosion Behavior in Nuclear Waste Systems, St. Paul Lez Durance, France, November 26–30, 2001. Accepted for publication. 2002.

necessary to experimentally track the evolution of the morphology as a function of time, not to mention the variety of parameters that must be correctly estimated for accurate predictions. Additional challenges to develop a percolation model for the long-term passive dissolution problem are the incorporation of a description of an oxide film that could detach from the alloy surface as defects are injected into the alloy, and the description of free local dissolution in the case of film spalling and reformation of a new oxide film, all of which depend on the local alloy composition at the interface. Percolation models have been used to present feasible morphologies consistent with particular dissolution mechanisms rather than used for estimating the time it would take for a system to evolve toward a particular state. It is the opinion of the authors that this latter objective is rather difficult to achieve.

Despite the difficulty in developing accurate predictive models, simplified models can still provide a reasonable estimate of the failure time of an alloy component dissolving under passive conditions. The main implication of the Point Defect Model is that defects are injected into the alloy causing the oxide film to become unstable. The passive current density decreases in time until reaching a value, I_o, controlled by a vacancy concentration saturation value. Additional vacancies injected into the alloy are destroyed with a subsequent contraction in the volume of the alloy, possibly in a continuous manner. By assuming that the oxide maintains contact with the metal substrate at all times by, for example, plastic flow, the passive dissolution model indicates that dissolution becomes stoichiometric as time elapses. If CR is the corrosion rate associated with the limiting value of an average current density, I_o, the time it would take for the average corrosion front to penetrate a distance, d, is computed as $t_o = d/CR$. In a rough surface, points of the corrosion front lie ahead and behind the average front. If the coefficient of variation of the corrosion rate (defined as the ratio of the standard deviation and the mean) is small (less than 0.1), the penetration time of the average corrosion front, t_o, is an adequate definition for the time to failure. Coefficients of variation for the passive current densities at the end of the experiments in Figure 5-1 are less than 10 percent.

On the other hand, after enough metal volume contraction, stress could develop in the oxide finally causing film spalling. Dissolution will be temporarily nonstoichiometric, but a new protective chromium oxide film should immediately form after spalling, forcing the system to display again stoichiometric dissolution as time elapses. The main anticipated outcome of this process is roughening of the surface, more pronounced than roughening solely caused by the stochastic variability of the corrosion rate (caused by heterogeneity in the surface and thermal and quantum mechanical fluctuations). In this case, the corrosion front will penetrate the thickness in a time less than t_o. In total system performance assessments, if the distribution of corrosion rates is biased in the positive direction, then possibly the effect of spalling on the time to failure is presumably within the uncertainty in the failure time computed by the Monte Carlo analyses.

Other possibility to explicitly account for the effect of spalling on the time to failure is by the introduction of an adjustment factor, f, as $t = f\,d/CR$. Using engineering judgement, the factor f could be in the range 0.5 to 0.7, but we acknowledge that there is not sufficient information to support this range of values. Possible approaches to derive values of f include (i)studying a high-temperature analog and computing how much the theoretical penetration time (i.e., $t_o = d/CR$) deviates from a direct penetration time from visual inspection and (ii) studying an analog with a high known dissolution rate and determining the time for the corrosion front to penetrate a thin foil of material and repeat the approach for foils of different thickness.

5.4 Other Possible Interpretations

In this section, other possible interpretations of the experimental data are discussed, as well as alternative mechanisms to enhanced dissolution. The first possibility is whether the injection of vacancies into the alloy is a necessary consequence of the dissolution process. Next, the possibility for the experimental decrease in the passive current density with time caused by secondary oxide thickening is discussed. Finally, the possibility of enhanced dissolution by mechanisms such as nonstroichiometric dissolution, transpassive dissolution, and sulfur segregation is discussed.

5.4.1 Oxygen Vacancies Versus Cation Interstitials

The injection of defects or vacancies at the metal-film interface results from the hypothesis that interstitials are the predominant charge carriers through the oxide film. It has been discussed that the passive current density versus potential for Alloy 22 is characteristic of a process for which cation interstitials or oxygen vacancies are the predominant charge carriers through the oxide film (see Appendix A). Cation vacancies have been disregarded because they would imply a passive current density that is a function of the applied potential. It is possible that oxygen vacancies, and not interstitials, are the main charge carriers through the film. Oxygen vacancies are injected at the metal-film interface via the reactions

$$\mathrm{Cr} \xrightarrow{k_3^{\mathrm{Cr}}} \mathrm{Cr_{Cr}} + \frac{\chi}{2}\mathrm{V}_o^{2+} + \chi e' \tag{5-28}$$

$$\mathrm{Ni} \xrightarrow{k_3^{\mathrm{Ni}}} \mathrm{Ni}_{\mathrm{Cr}}^{\delta-\chi} + \frac{\chi}{2}\mathrm{V}_o^{2+} + \delta e' \tag{5-29}$$

Reactions represented in Eqs. (5-28) and (5-29) cause film growth at the metal-film interface. To control the thickness of the oxide film, the Point Defect Model postulates that the oxide film dissolves at the metal-electrolyte interface by the following reaction

$$[\mathrm{Cr}_{1-y}\mathrm{Ni}_y\mathrm{O}_{\chi/2}]^{y(\delta-\chi)} + \chi\mathrm{H}^+ \xrightarrow{k_7} (1-y)\mathrm{Cr}^{\chi+} + y\mathrm{Ni}^{\delta+} + \frac{\chi}{2}\mathrm{H_2O} \tag{5-30}$$

Under steady-state conditions, the rate of formation of the film equals the rate of film dissolution, which in mathematical form can be expressed as

$$a_{\mathrm{Cr}}k_3^{\mathrm{Cr}} + a_{\mathrm{Ni}}k_3^{\mathrm{Ni}} = k_7(1-y)^{1-y}y^y\left(a_{\mathrm{H}^\cdot}\right)^n \tag{5-31}$$

If the rate of film dissolution at the metal-film interface is different from zero (i.e., $k_7 \neq 0$), then the oxide film would exist in a metastable state, continuously forming and dissolving. Thermodynamic data suggest, however, that chromium oxide is a stable phase (see Section 2.1). Therefore, the rate of spontaneous dissolution of the oxide may be negligible (i.e., the rate constant, k_7, may be small), and the rates of oxygen vacancy injection, k_3^{Cr} and k_3^{Ni}, may be negligible as well. Consequently, the predominant charge carriers through the oxide layer, consistent with the thermodynamic stability of chromium oxide and the experimental requirement of the passive current density to be independent of the applied potential, are cation interstitials. It is recognized, however, that bulk thermodynamic properties (i.e., free energies of formation) used to construct stability diagrams in Section 2.1 are for thick, bulk oxides, which may be significantly different from the thin surface oxide films (MacDougall and Graham, 1995). Thus, the conclusion of predominant interstitial conduction may need to be revisited if thin film oxide thermodynamics are significantly different from bulk oxide thermodynamics.

5.4.2 Growth of the Secondary Oxide Layer

The second question to address is whether the temporary decrease in the passive current density can be explained as a function of oxide layer growth. At room temperature, metals such as iron, nickel, and chromium develop oxide layers that achieve a steady-state thickness in minutes (see, for example, Fehlner and Graham, 1995). The temperature must be increased to several hundreds of degrees centigrade to note a monotonic increase of the oxide thickness as a function of time. Thus, in the passive dissolution model, it is assumed the primary oxide layer in contact with the metal substrate is always at the steady-state thickness. It cannot be ruled out however, that a secondary oxide layer also develops offering protection against metal dissolution. This secondary barrier could be a porous layer with a porosity that possibly decreases as a function of time causing the passive current density to also decrease as a function of time (Evans, 1978). It would be useful to design experiments to track the thickness of the oxide layer as a function of time. In case the thickness increases or the porosity decreases, these changes could be correlated to the temporary decrease in the current density. If the secondary oxide layer is a precipitated oxide, there is no evident mechanism limiting its thickness. Thus, an explanation should be developed to why the current density seems to reach a steady-state value (a monotonic decrease of the current density would be expected because of the increasing protection of the secondary oxide layer). For example, there could exist a minimum limiting porosity independent of the thickness of the secondary oxide layer. It is definitely important to elaborate mechanisms of passive dissolution and test them experimentally to be in a more advantageous position to evaluate long-term consequences of the dissolution process.

Regardless of whether changes in the primary and secondary oxide layers are responsible for the decays in the current density, numerous authors agree that any oxidation process in which the metal dissolves via the transport of cations through the oxide results in the injection of vacancies into the alloy (see, for example, the compilation of papers on the subject of vacancies by Smallman and Harris, 1977). If vacancies are readily annihilated, a volume change must be accommodated by the system, which could result in the long-term instability of the protective passive oxide film (Gibbs and Hales, 1977). It is not envisioned that frequent rupture of the oxide layer will result in catastrophic failure. Instead, we believe that the main outcome of a film-rupture process is surface roughening (See Section 5.3).

5.4.3 Nonstoichiometric Dissolution

Another point deserving special attention is stoichiometric dissolution. In the passive dissolution model, stoichiometric dissolution is the result of a process regulated by solid-state diffusion. Solid-state diffusion forces the dissolution process to become stoichiometric, assuming the atoms of the different elements in the alloy diffuse at similar rates. This assumption is consistent with diffusion coefficient data for nickel-chromium alloys at high temperatures (Brandes and Brook, 1992). Also, there is some natural analog evidence, via the analysis of meteoritic iron-nickel alloys, that long-term dissolution proceeds in stoichiometric form (Sridhar and Cragnolino, 2002).

Experimental deviations from stoichiometry in the dissolution process would indicate the presence of high-diffusion paths in the alloy, such as grain boundaries, favoring transport of one alloy element over the others. It could also indicate that the alloy slowly evolves into the complex morphologies characteristic of the phenomenon of dealloying (Sieradzki, et al., 1989). One envisioned consequence of nonstoichiometric dissolution is the alteration in time of mechanical properties. Although there is no evidence that long-term dissolution is nonstoichiometric; it is desirable to gather experimental data in this regard, either from natural analog or from controlled conditions, to decide whether nonstoichiometric dissolution deserves special attention. The challenge in designing an experimental technique tracking the concentration of ions in solution is acknowledged, given the slow rate of passive dissolution and the low solubility of corrosion products that finally precipitate on the walls of experimental systems (Dunn, et al., 2001). The importance of the verification of stoichiometric dissolution to provide additional support on the validity of assumptions behind long-term extrapolation is evident.

5.4.4 Transpassive Dissolution

Other possible mechanisms for enhanced dissolution are an increase in the corrosion potential beyond the transpassive potential and sulfur-enhanced oxidation (Waste Package Materials Peer Review Panel, 2002). Recent studies on the modeling of fluid chemistry inside a waste package accounting for waste form dissolution and inner waste package corrosion[2] indicate that the redox potential could be highly sensitive to changes in the environment. In the presence of oxygen, the redox potential could swing from −250 mV_{SHE} to +600 mV_{SHE} (assuming the presence of corrosion products in the solution arising from the dissolution of Type 316L SS) and produce Cr(VI) complexes attributed to transpassive dissolution. Similar shifts in the redox potential could occur at the surface of the corroding Alloy 22. The magnitude of this shift will depend on the composition, pH, and Eh of the groundwater and the concentrations of corroding species in the solution contacting the waste package. At this time, simulation data are not available to allow evaluation of these shifts for Alloy 22. Because of the susceptibility of Type 316L SS to stress corrosion cracking and to localized corrosion, in particular crevice corrosion, the dissolution rate of Type 316L SS could be orders of magnitude higher than the general corrosion dissolution rate of Alloy 22 (Cragnolino, et al., 1999). Therefore, the concentration of corroding species in solution from the dissolution of Alloy 22 is much lower than anticipated for the solution inside the waste package. Moreover, the solution contacting the outside of the waste package is not enclosed to allow corrosion species to concentrate with time. In other words, corrosion products may wash away because there is no evident mechanism to hold these products near the surface of Alloy 22. Although transpassive dissolution cannot be ruled out from the model computations, it is considered unlikely because of the significant concentration of oxidizing species in solution required to reach high redox

---

[2] Jain, V. and N. Sridhar. "Modeling Fluid Chemistry Inside a Waste Package Due to Waste Form and Waste Package Corrosion." Symposium on Ceramic Science and Technology for the Nuclear Industry, St. Louis, Missouri, April 28–May 1, 2002. Ceramic Transactions Vol. 139. Westerville, Ohio: American Ceramic Society. Accepted for publication. 2002.

potentials and also because the transition to transpassive dissolution is determined by the corrosion potential and not by the redox potential.

5.4.5 Sulfur Segregation

Another potential mechanism resulting in increase of corrosion rates is sulfur-enhanced dissolution. If reduced sulfur species are present in the electrolyte or environment, a critical adsorbed sulfur coverage greater than 0.7–0.8 can inhibit the formation of a passivating oxide film on nickel (Marcus, 1995). Below this surface coverage on nickel, a nickel oxide layer forms but is contaminated with sulfur. The passive current density for the sulfur-contaminated nickel system is up to four times greater than a reference system in the absence of sulfur (Marcus, 1995). Sulfides can form from sulfur impurities in the metal by anodic segregation. Anodic segregation is known to affect nickel, nickel-iron alloys (Marcus, et al., 1984a,b; Marcus and Olefjord, 1986), Alloy 600 (Ni-16Cr-6Fe) (Marcus and Grimal, 1990), and austenitic stainless steels (Elbiache and Marcus, 1992). Anodic sulfur segregation results from the preferential dissolution of the metal and the accumulation of sulfur at the surface. In the case of nickel, the segregated sulfur is a precursor to the formation of nickel sulfide, which is not a protective film, and prevents the formation of nickel oxide. The anodic segregation rate is proportional to the sulfur content of the material and to the rate of anodic dissolution of the metal (Marcus, 1995). Enhanced dissolution rates, in case of the presence of sulfur at the metal surface are the result of a catalytic process, in which the metal dissolves preferentially with respect to sulfur. In other words, the sulfur remains at the surface during the enhanced dissolution process. If the oxide layer is already formed on nickel or nickel-iron alloys containing sulfur as impurity, anodic dissolution can result in segregation of sulfur at the metal-oxide interface, weakening the adhesion of the oxide, and potentially resulting in localized corrosion if the oxide layer breaks.

With respect to alloy additions, molybdenum and chromium are known to counteract the detrimental effect of sulfur in nickel (Marcus, 1995). The presence of molybdenum in nickel-molybdenum alloys counteracts the effect of sulfur possibly by the formation of soluble molybdenum-sulfur compounds. By forming these compounds, molybdenum forces sulfur to dissolve at a rate proportional to the rate of molybdenum dissolution, decreasing the extent of segregation at the surface (Marcus, 1995). The mechanism by which chromium counteracts the detrimental effect of sulfur is different. Chromium has a low affinity for sulfur, but a high affinity for oxygen, while the reverse is true for nickel. Thus, for the particular case of nickel-chromium alloys, the formation of Cr_2O_3 competes with the formation of Ni_3S_2. Formation of a protective Cr_2O_3 film suppresses the effect of Ni_3S_2. The presence of chromium allows the metal surface to be passivated in conditions where the passivation would not be possible if there was no chromium. In the discussion of the composition of the oxide film in Section 2.1, it was noted that above a critical chromium content (~15 wt%), the predominant oxide forming on the nickel-chromium alloys is chromium oxide. Below the critical chromium content, nickel oxide is the predominant oxide layer forming on the nickel-chromium alloys (Boudin, et al., 1994). Similarly, there should exist a critical chromium content above which a protective chromium oxide layer forms (with nickel sulfide islands) or passivity is inhibited if the chromium content is too low.

Alloy 22 contains molybdenum, chromium, and a low amount of sulfur because of the electroslay remelting process. If sulfur segregation occurs, nickel sulfide islands will develop in the protective chromium oxide film. These formations could degrade the adhesion or stability of the film. If the oxide ruptures, reformation of a chromium oxide film may occur, given the predominance of chromium at the metal-oxide interface. Also, the presence of molybdenum in the alloy may facilitate the dissolution of sulfur, reducing the extent of sulfide segregation at the interface.

An alloy with 100 ppm of atoms sulfur dissolving at a rate of 1 μm/yr [3.9×10^{-5} in/yr] could accumulate a monolayer of sulfur on the surface in 500 years if 100 percent of the sulfur atoms is retained at the surface (Waste Package Materials Peer Review Panel, 2002) and also if the evolving surface is planar (if roughening occurs, the surface area increases requiring more sulfur to complete a monolayer coverage). The presence of molybdenum in an alloy may enhance the rate of sulfur dissolution and delay the time to develop a monolayer coverage. If sulfur segregation causes detachment from the oxide and catalytic enhanced dissolution of nickel from the alloy, a key question to address is how long this enhanced dissolution can be sustained. From the model results we argued that preferential dissolution of one alloy element cannot be sustained for extended periods unless there is a fast solid-state transport path of the preferentially dissolving component. Fast solid-state transport of nickel sustained for extended periods does not seem possible. Preferential dissolution of nickel results in enrichment of chromium at the surface, promoting the reformation of a protective chromium oxide layer at a later stage. A possibility to maintain preferential dissolution of nickel for extended periods is a fast localized penetration of the corrosion front (following, for example, a connected network of nickel in the alloy) resulting in complex morphologies (such as those produced during dealloying) or surface roughening. Because the extent of the corroding surface area will increase as the complex morphology develops, the surface coverage of sulfur will decrease, also allowing reformation of a protective chromium oxide film. Therefore, it is not anticipated that the sulfur-enhanced dissolution process, if it occurs, can be sustained for extended periods. Nonetheless, sulfur-enhanced dissolution is another source of uncertainty in the evolution of the morphology of the corrosion front that should be accounted for by the uncertainty in the estimates of the failure time by general corrosion.

6 SUMMARY

In this report, the long-term passive behavior of Alloy 22 was analyzed. The passivity of Alloy 22 is determined by the formation of a protective oxide film. Based on thermodynamic data it was suggested this oxide film is most likely to be composed of Cr_2O_3. Other feasible phases are $Ni[OH]_2$ and $NiMoO_4$. Data reported in the literature (Waste Package Materials Peer Review Panel, 2002) are consistent with the notion that the surface film is composed of a bilayered structure, with chromium-nickel- and nickel-molybdenum-rich oxides. The chromium oxide-rich inner layer may have a predominant role in the passivity of Alloy 22, and secondary outer layers formed by dissolution and precipitation are presumably minor contributors to passivity.

Models for oxide growth were reviewed and the challenge in developing discriminating criteria to identify the growth law applicable to a metal or alloy in an aqueous environment was highlighted. Currently, models for long-term prediction of passive dissolution are not available mainly because extrapolation of passive dissolution is of much less importance to most industrial applications than determining factors controlling passivity and passivity breakdown.

Traditional methods to measure corrosion rates rely on either direct weight loss or indirect calculation of corrosion rates using electrochemical data and Faraday's law. Weight loss measurements are appropriate for systems where loss of metal can be accurately determined in a short period. This method inherently assumes that the corrosion rate is uniform and constant during the exposure interval. For passive metals with low corrosion rates, the time necessary to perform an immersion test can be lengthy, and arbitrarily reducing the test time increases measurement uncertainty. In addition, confounding effects such as the formation of oxide films and the accumulation of corrosion products and deposits introduce additional uncertainty in the corrosion rate measurements. Electrochemical methods, such as anodic passive current density measurements, polarization resistance, and electrochemical impedance can be used to measure corrosion rates in a nearly continuous manner. In addition, the resolution of electrochemical methods is, in general, higher than that of gravimetric methods. The disadvantages of the electrochemical methods are the extensive instrumentation needs, which is a significant concern for long-term monitoring of corrosion rates, and the general difficulty of separating reactions associated with the dissolution of the alloy to those that are not. For extremely low corrosion rates, typical of passive nickel-chromium-molybdenum alloys, the instrument resolution sets a limit or threshold to the validity of electrochemical methods.

Passive corrosion rates of Alloy 22 were measured using both potentiostatic anodic passive current density and polarization resistance methods. Corrosion rates derived from both methods compare well for 95 °C [203 °F] data and resulted in rates approximately 5×10^{-4} mm/yr [2×10^{-5} in/yr]. However, there is significant uncertainty (noted by poor fit statistics) in the corrosion rate by the polarization resistance method. Also, the polarization resistance and derived corrosion rate were found to depend on the scan rate; thus, adequate selection of the scan rate is important.

Passive corrosion rates were independent of the composition of the solution. The potentiostatic anodic passive current density at 95 °C [203 °F] noticeably decreased as a function of time. A decrease is not evident at lower temperatures. At temperatures of 60 °C [140 °F] and lower, the anodic passive current density was near the resolution limit of the instrumentation, and accurate measurement of the passive corrosion rates was not possible. From median values of the potentiostatic anodic passive current density data, it was noted that the dependence of the current density on the temperature is of an Arrhenius form. The apparent activation energy of the Arrhenius expression was computed to be 44.7 kJ mol^{-1} [10.7 kcal mol^{-1}] with a standard deviation of 5.5 kJ mol^{-1} [1.3 kcal mol^{-1}] over the temperature range of 25 to 95 °C. The apparent activation energy is related to the activation energy of the rate constants of fundamental charge transfer reactions controlling the alloy dissolution.

A model was formulated for the passive dissolution of nickel-chromium-molybdenum alloys (of which Alloy 22 is a particular example) based on the Point Defect Model, which was formulated to develop a mechanistic understanding of passivity and passivity breakdown of metals in low temperature aqueous systems. Based on the model, we argued that the dominant species transporting charge through the oxide film are interstitials and oxygen vacancies. When oxygen vacancies are the dominant charge carriers, the oxide film is metastable. Consequently, oxygen vacancy transport is at odds with the thermodynamic stability of chromium oxide (for environmental conditions of relevance to the proposed repository system), and it was, therefore, concluded that the dominant charge carriers should be cation interstitials. However, most thermodynamic data correspond to bulk oxides that may not be representative of the thin oxides (nanometers thick) controlling the dissolution behavior. Dissolution of the alloy in the form of interstitials causes the creation of vacancies in the alloy. The hypothesis of vacancy creation as a result of the dissolution process agrees with conclusions by other authors for high-temperature systems [e.g., see the compilation of papers on vacancies by Smallman and Harris (1977)]. In particular, for nickel and nickel-chromium alloys, the concept of vacancy injection or vacancy creation by the dissolution process has been used to explain the creation of voids at high temperatures {>1, 000 °C [1,832 °F]} at the metal-film interface, in the bulk of the alloy, and at grain boundaries (Hancock and Fletcher, 1966; Douglass, 1968; Hales and Hill, 1972; Shida, et al., 1981; Stott, et al., 1981). Hancock (1977) used the concept of vacancy injection during high-temperature oxidation to explain changes in mechanical properties of nickel-chromium alloys. There are relatively few systems where vacancy injection has been reported at low temperatures, zinc being one of them (Berghezan, et al.,1961; Dobson and Smallman, 1966).

The model predicts that if vacancies are created in the alloy and accumulate at the metal-film interface, the passive current density will decrease as a function of time. Therefore, the model is consistent with the experimental data—a decreasing trend in the passive current density in various solutions was noted in 2-week experiments under potentiostatic control at 95 °C [203 °F]. Adequate goodness of fit was obtained between experimental data and simulated current densities for particular selections of rate constants and finite difference parameters. It was thus concluded that the experimental data are consistent with the hypotheses of predominant interstitial cation conduction and vacancy injection at the metal-film interface. It was suggested that steady state in the anodic current density occurs after reaching a saturation value of the vacancy concentration at the metal-film interface. It is acknowledged that the proposed model for the passive dissolution of the alloy ceases to be valid after reaching this saturation concentration.

The model was used to address the question of whether or not dissolution is stoichiometric. We argued that dissolution can be nonstoichiometric during a short term, but in the long term, it evolves toward stoichiometry, which is consistent with observations reported in the literature for similar alloy systems (Cavanaugh, et al., 1983; Kirchheim, et al.,1989). The conclusion of congruent or stoichiometric dissolution depends on the assumption that diffusion coefficients for the atoms of the alloy elements are similar, which is also an assumption consistent with the literature of solid state diffusion (Brandes and Brook, 1992).

The main implication of the phenomenon of vacancy injection is the long-term instability of the oxide film, recognized by other authors (Gibbs and Hales, 1977; Stringer, 1977). It is not anticipated that periodic spalling of the film will significantly accelerate the rate of penetration of the corrosion front because a protective chromium oxide could form again in case of spalling. The main envisioned consequence of the possible long-term instability of the oxide film is the evolution of the surface into a rough morphology. The effect of periodic spalling and surface roughening is presumably within the uncertainty in the time to waste package failure computed by current performance assessments. Otherwise, it is recommended, from engineering judgement, to introduce an adjustment factor in the range of 0.5 to 0.7 into the equation for calculating the failure time of the waste package.

Other alternatives and interpretations that also could be consistent with the electrochemical data were considered and discussed. Also, possibilities leading to enhanced alloy dissolution rates were presented, such as transpassive dissolution and anodic sulfur segregation. We argued that transpassive dissolution is unlikely to arise given the significant concentration of oxidizing species in the solution necessary to cause the corrosion potential to exceed a critical potential for transpassivity. Sulfur-enhanced dissolution and sulfur segregation, according to information in the literature, seem to affect predominantly the dissolution of nickel in nickel-chromium and nickel-chromium-molybdenum alloys. It was noted that Alloy 22 contains a low sulfur content because of the electroslay remelting process used to produce it. In alloys containing chromium, it appears that the stability of Cr_2O_3 precludes the dissolution rate enhancement caused by anodic segregation of sulfur. Because the model indicates that preferential dissolution of one alloy component during extended periods is not possible, it is concluded that preferential dissolution of nickel via sulfur-enhanced dissolution cannot be sustained for extended periods in nickel-chromium-molybdenum alloys.

6.1 Recommended Future Work

It is recommended to continue using electrochemical methods to determine passive corrosion rates, such as polarization resistance and potentiostatic anodic current density. It also is recommended to verify the reproducibility of the apparent activation energy. Potential effects of solution composition on the corrosion rate should be explored by using higher chloride concentrations and solutions with ionic species possibly present in the groundwater of the proposed repository, eventually extending the measurements to temperatures higher than 95 °C [203 °F]. Evaluation of electrochemical impedance spectroscopy should be performed, because this method may provide better resolution, especially at low temperatures, and may be a suitable monitoring technique. Longer-term (> 2 weeks) potentiostatic anodic current density tests should be completed to determine the time when systems achieve steady state at 95 °C [203 °F].

It is important to explore analytical techniques that identify the relative location of chromium, nickel, and molybdenum in the oxide. It has been reported in the literature that the inner oxide is chromium-nickel rich, while the outer oxide is nickel-molybdenum rich, and it is relevant to corroborate these findings. It is recommended to study the composition of the oxide, using, for example, x-ray photoelectron spectroscopy, and to study changes in the oxide composition as a function of the applied potential and time. Possibly the chromium content of the oxide is linearly dependent on the applied potential and is independent of the polarization direction. This follows from the fact that the thickness of passive oxide films is, in general, proportional to the applied potential. Because the outer oxide possibly forms by dissolution and precipitation, we suggest that the nickel and molybdenum contents in the overall oxide are independent of the applied potential, but may increase as functions of time. Presumably, the outer barrier oxide layer will thicken as time elapses, increasing the content of nickel and molybdenum. We recognize that chromium may be present in the overall oxide not only as a phase formed from solid-state electrochemical reactions in the inner oxide but also as a precipitated phase in the outer oxide layer. Determination of the content and location of chromium, nickel, and molybdenum in the overall oxide film as functions of the applied potential and time may yield relevant information on the role of the inner and outer oxides in the phenomenon of passivity, as well as on the alloy dissolution mechanism.

It is important to correlate changes in thickness in the oxide film to the temporary decrease in the passive current density reported in Chapters 4 and 5. If there is correspondence between the time of stabilization of the oxide film and the time the current density ceases to decrease, the two phenomena may be correlated, and the ideas concerning vacancy accumulation at the metal-film interface may need to be revised. It may be possible to use ellipsometry to study the variation in film thickness as a function of time.

It is relevant to determine the concentration profiles in the alloy close to the oxide and to study changes in the concentration profile as a function of time. Information available in the literature is, in general, restricted to a short period after the formation of the oxide for nickel-chromium alloys. It is desirable to detect a possible enrichment of chromium at the interface as a function of time to corroborate model predictions or yield additional information to refine the proposed alloy dissolution mechanisms.

Additional insights on the role of the oxide films and passive dissolution could be gained by studying thin films. It has been mentioned that thermodynamic properties of bulk materials could differ from thermodynamic properties of thin oxides. Also, the relationships are unclear among the electronic properties of the oxide film on Alloy 22, its protective role, and the passive current density versus voltage dependence. In the model for dissolution of nickel-chromium-molybdenum alloys, we assumed that kinetic rates of the fundamental charge transfer reactions at the metal-film interface control the rate of dissolution. This assumption should be tested as well as the assumption of predominant charge transport via cation interstitials. It may be possible that the rate of charge transfer through the oxide plays a predominant role in the passivity for nickel-chromium-molybdenum alloys.

The passive dissolution model should be extended to incorporate dissimilar diffusion coefficients and analyze the dependence of the conclusion of stoichiometric dissolution on the hypothesis of similarity of diffusion for the atoms of the alloy elements. Concepts such as vacancy saturation and vacancy annihilation should be incorporated to extend the range of validity of the model. It is recommended to study percolation models to identify if they could provide a modeling tool to address the problem of film spalling and surface roughening.

Finally, it is recommended to design an experimental technique to support the selection of an adjustment factor (intended to account for uncertainties related to film spalling and surface roughening) to the failure time of the waste package computed by total system performance assessments.

7 REFERENCES

ASTM International. "Standard Test Method for Conducting Corrosion Coupon Tests in Plant Equipment." *ASTM G–4: Annual Book of Standards. Volume 3.02: Wear and Erosion—Metal Corrosion.* West Conshohocken, Pennsylvania: ASTM International. 2001a.

———. "Standard Practice for Laboratory Immersion Corrosion Testing of Materials." *ASTM G–31: Annual Book of Standards. Volume 3.02: Wear and Erosion—Metal Corrosion.* West Conshohocken, Pennsylvania: ASTM International. 2001b.

———. "Standard Practice for Calculation of Corrosion Rates and Related Information from Electrochemical Measurements." *ASTM G102–89: Annual Book of Standards. Volume 3.02: Wear and Erosion—Metal Corrosion.* West Conshohocken, Pennsylvania: ASTM International. 2001c.

———. "Standard Practice for Verification of Algorithm and Equipment for Electrochemical Impedance Measurements." *ASTM G106: Annual Book of Standards. Volume 3.02: Wear and Erosion—Metal Corrosion.* West Conshohocken, Pennsylvania: ASTM International. 2001d.

Bechtel SAIC Company. "FY01 Supplemental Science and Performance Analyses—Volume 1: Scientific Bases and Analyses." TDR–MGR–MD–000007. Rev. 00 ICN 01. Las Vegas, Nevada: Bechtel SAIC Company. 2001.

Bedrossian, P.J. and J.C. Farmer. "Pit Initiation and Evolution on Stainless Steels and Ni-Based Alloys." Abstracts of the Materials Research Society Conference, Scientific Basis for Nuclear Waste Management XXIII. Boston, Massachusetts, November 29–December 3, 1999. Paper No. QQ14.11. Warrendale Pennsylvania: Materials Research Society. p. 753. 1999.

Berghezan, A., A. Fourdeux, and S. Amelinckx. "Transmission Electron Microscopy Studies of Dislocations and Stacking Faults in a Hexagonal Metal: Zinc." *Acta Metallurgica.* Vol. 9. p. 464. 1961.

Bond, A.P. and H.H. Uhlig. "Corrosion Behavior and Passivity of Nickel-Chromium and Cobalt-Chromium Alloys." *Journal of Electrochemical Society.* Vol. 107. pp. 448–493. 1970.

Boudin, S., J-L. Vignes, G. Lorang, M. DaCunha Belo, G. Blondiaux, S.M. Mikhailov, J.P. Jacobs, and H.H. Brongersma. "Analytical and Electrochemical Study of Passive Films Formed on Nickel-Chromium Alloys: Influence of the Chromium Bulk Concentration." *Surface and Interface Analysis.* Vol. 22. pp. 462–466. 1994.

Bracht, H. "Diffusion Mechanisms and Intrinsic Point-Defect Properties in Silicon." *MRS Bulletin.* Vol. 25, No. 6. pp. 22–27. 2000.

Brandes, E.A. and G.B. Brook, eds. *Smithells Metals Reference Book.* Oxford, England: Butterworth-Heinemann, Ltd. pp. 13-52 through 13-53. 1992.

Brossia, C.S., L. Browning, D.S. Dunn, O.C. Moghissi, O. Pensado, and L. Yang. "Effect of Environment on the Corrosion of Waste Package Materials and Drip Shield Materials." CNWRA 2001-003. San Antonio, Texas: CNWRA. 2001.

Burstein, G.T. and A.J. Davenport. "The Current-Time Relationship During Anodic Oxide Film Growth Under High Electric Field." *Journal of Electrochemical Society.* Vol. 136. pp. 936–941. 1989.

Cabrera, N. and N.F. Mott. "Theory of the Oxidation of Metals." *Reports on Progress in Physics.* Vol. 12, No. 163. 1948–49.

Cavanaugh, M.A, J.A. Kargol, J. Nickerson, and N.F. Fiore. "The Anodic Dissolution of a Ni-Base Superalloy." *Corrosion.* Vol. 39. pp. 144–159. 1983.

Cragnolino, G.A., D.S. Dunn, Y.-M. Pan, and O. Pensado. "Corrosion Processes Affecting the Performance of Alloy 22 as a High-Level Radioactive Waste Container Material." Scientific Basis for Nuclear Waste Management XXIV. K.P. Hart and G.R. Lumpkin, eds. Symposium Proceedings 663. Warrendale, Pennsylvania: Materials Research Society. 2001.

Cragnolino, G.A., D.S. Dunn, C.S. Brossia, V. Jain, and K.S. Chan. "Assessment of Performance Issues Related to Alternative Engineered Barrier System Materials and Design Options." CNWRA 99-003. San Antonio, Texas: CNWRA. 1999.

CRWMS M&O. "Repository Safety Strategy: Plan to Prepare the Postclosure Safety Case to Support Yucca Mountain Site Recommendation and Licensing Considerations." TDR–WIS/RL–000001. Rev. 04 ICN 01. Las Vegas, Nevada: CRWMS M&O. 2000.

Dawson, J.L., G.E. Thompson, and M.B.H. Ahmadun. "Evolution of Electrochemical Impedance During Sealing of Porous Anodic Films on Aluminum." *ASTM STP–1188: Electrochemical Impedance—Analysis and Interpretation.* J.R. Scully, D.C. Silverman, and M.W. Kendig, eds. Philadelphia, Pennsylvania: ASTM International. pp. 255–275. 1993.

Dobson, P.S. and R.E. Smallman. "The Climb of Dislocation Loops in Zinc." *Proceedings of the Royal Society of London, Series A.* Vol. A–293. pp. 423. 1966.

Douglass, D.L. "The Oxidation Mechanism of Dilute Ni-Cr Alloys." *Corrosion Science.* Vol. 8. pp. 665–678. 1968.

Dunn, D.S. and C.S. Brossia. "Assessment of Passive and Localized Corrosion Processes for Alloy 22 as a High-Level Nuclear Waste Container Material." Proceedings of the Corrosion 2002 Conference. Paper No. 548. Houston, Texas: NACE International. 2002.

Dunn, D.S., C.S. Brossia, and O. Pensado. "Long-Term Dissolution Behavior of Alloy 22: Experiments and Modeling." Proceedings of the Corrosion 2001 Conference. Paper No. 01125. Houston, Texas: NACE International. 2001.

Dunn, D.S, Y.-M. Pan, and G.A Cragnolino. "Stress Corrosion Cracking, Passive, and Localized Corrosion of Alloy 22 High-Level Radioactive Waste Containers." Proceedings of the Corrosion 2000 Conference. Paper No. 00206. Houston, Texas: NACE International. 2000a.

Dunn, D.S., G.A. Cragnolino, and N. Sridhar. "Passive Dissolution and Localized Corrosion of Alloy 22 High-Level Waste Container Weldments." Scientific Basis for Nuclear Waste Management XXIII. R.W. Smith and D.W. Shoesmith, eds. Symposium Proceedings 608. Pittsburgh, Pennsylvania: Materials Research Society. pp. 89–94. 2000b.

Dunn, D.S., Y.-M. Pan, and G.A. Cragnolino. "Effects of Environmental Factors on the Aqueous Corrosion of High-Level Radioactive Waste Containers—Experimental Results and Models." CNWRA Report 99-004. San Antonio, Texas: CNWRA. 1999.

Dunnington, B.W., F.H. Beck, and M.G. Fontana. "The Mechanism of Scale Formation on Iron at High Temperature." *Corrosion*. Vol. 8. p. 2t. 1952.

Elbiache, A. and P. Marcus. "The Role of Molybdenum in the Dissolution and the Passivation of Stainless Steels with Adsorbed Sulphur." *Corrosion Science*. Vol. 33, No. 2. pp. 261–269. 1992.

Epelboin, I., C. Gabrielli, M. Keddam, and H. Takenouti. "Alternating-Current Impedance Measurements Applied to Corrosion Studies and Corrosion-Rate Determination." *ASTM 727: Electrochemical Corrosion Testing*. F. Mansfeld and U. Bertocci, eds. Philadelphia, Pennsylvania: ASTM International. pp. 150–166. 1981.

Evans, T.E. "Growth of Surface Oxide Films on Metals and Alloys by Dissolution and Precipitation Processes." *Passivity of Metals*. R.P. Frankenthal and J. Kruger, eds. Princeton, New Jersey: The Electrochemical Society. pp. 410–412. 1978.

Evans, U.R. *The Corrosion and Oxidation of Metals: First Supplementary Volume*. New York City, New York: St. Martin's Press. pp. 297–309. 1968.

———. *The Corrosion and Oxidation of Metals: Scientific Principles and Practical Applications*. New York City, New York: St. Martin's Press. pp. 845–849. 1960.

Fehlner, F.P. *Low-Temperature Oxidation: The Role of Vitreous Oxides*. New York City, New York: John Wiley and Sons. p. 4. 1986.

Fehlner, F.P. and M.J. Graham. "Thin Oxide Film Formation on Metals." *Corrosion Mechanisms in Theory and Practice*. P. Marcus and J. Oudar, eds. New York City, New York: Marcel Dekker. pp. 123–142. 1995.

Fletcher, S. "Tables of Degenerate Electrical Networks for Use in the Equivalent-Circuit Analyses of Electrochemical Systems." *Journal of the Electrochemical Society*. Vol. 141. pp. 1,823–1,826. 1994.

Gabrielli, C. "Use and Applications of Electrochemical Impedance Techniques." Technical Hampshire, England: Schlumberger Technologies Instruments Division. 1990.

———. "Identification of Electrochemical Processes by Frequency Response Analyses." Technical Report No. 004/83. Hampshire, England: Schlumberger Technologies Instruments Division. 1984.

Gibbs, G.B. and R. Hales. "Influence of Metal Lattice Vacancies on the Oxidation of High Temperature Materials." Proceedings of the Metals Society Point Defect Behavior and Diffusional Processes Conference, University of Bristol, London, United Kingdom, September 13–16, 1976. R.E. Smallman and J.E. Harris, eds. Vacancies 76. London, United Kingdom: The Metals Society. pp. 201–207. 1977.

Hales, R. and A.C. Hill. "The Role of Metal Lattice Vacancies in the High Temperature Oxidation of Nickel." *Corrosion Science*. Vol. 12. pp. 843–853. 1972.

Hancock, P. "Influence of Vacancies Produced by Oxidation on the Mechanical Properties of Nickel and Nickel-Chromium Alloys." Proceedings of the Metals Society Point Defect Behavior and Diffusional Processes Conference, University of Bristol, London, United Kingdom, September 13–16, 1976. R.E. Smallman and J.E. Harris, eds. Vacancies 76. London, United Kingdom: The Metals Society. pp. 215–222. 1977.

Hancock, P. and R. Fletcher. "The Oxidation of Nickel in the Temperature Range of 700–1,000 °C." *Metallurgie*. Vol. 6. pp. 1–9. 1966.

Heusler, K.E. "Influence of Temperature and Pressure on the Kinetics of Electrode Processes." *High Temperature High Pressure Electrochemistry in Aqueous Solutions*. Conference held at the University of Surrey, England, January 7-12, 1973. R.W. Staehle, D. de G. Jones, and J.E. Slater, eds. Houston, Texas: NACE. Vol. NACE-4, pp. 387-399. 1976.

Kirchheim, R., B. Heine, S. Hofmann, and H. Hofsäss. "Compositional Changes of Passive Films Due to Different Transport Rates and Preferential Dissolution." *Corrosion Science*. Vol. 31. pp. 573–578. 1990.

Kirchheim, R., B. Heine, H. Fischmeister, S. Hofmann, H. Knote, and U. Stollz. "The Passivity of Iron-Chromium Alloys." *Corrosion Science*. Vol. 29. pp. 899–917. 1989.

Lorang, G., N. Jallerat, K. Vu Quang, and J-P. Langeron. "AES Depth Profiling of Passive Overlayers Formed on Nickel Alloys." *Surface and Interface Analysis*. Vol. 16. pp. 325–330. 1990.

Lumsden, J.B. and R.W. Staehle. "Composition of Protective Films Formed on Iron and Stainless Steels." *Surface Analysis Techniques for Metallurgical Applications: A Symposium*. Philadelphia, Pennsylvania: ASTM International. pp. 39–51. 1976.

Macdonald, D.D. "The Point Defect Model for the Passive State." *Journal of Electrochemical Society*. Vol. 139. pp. 3,434–3,449. 1992.

Macdonald, D.D. and M. Urquidi-Macdonald. "Theory of Steady-State Passive Films." *Journal of Electrochemical Society*. Vol. 137. pp. 2,395–2,402. 1990.

Macdonald, D.D., M.A. Rifaie, and G.R. Engelhardt. "New Rate Laws for the Growth and Reduction of Passive Films." *Journal of Electrochemical Society.* Vol. 148. pp. B343–B347. 2001.

Macdonald, D.D., S.R. Biaggio, and H. Song. "Steady-State Passive Films." *Journal of Electrochemical Society.* Vol. 139. pp. 171–177. 1992.

MacDougall, B. and M.J. Graham. "Growth and Stability of Passive Films." *Corrosion Mechanisms in Theory and Practice.* P. Marcus and J. Oudar, eds. New York City, New York: Marcel Dekker. pp. 143–173. 1995.

Mansfeld, F. "Polarization Resistance Measurements—Experimental Procedure and Evaluation of Test Data." *Electrochemical Techniques for Corrosion.* R. Baboian, ed. Houston, Texas: NACE International. pp. 18–26. 1977.

———. "Simultaneous Determination of Instantaneous Corrosion Rates and Tafel Slopes from Polarization Resistance Measurements." *Journal of the Electrochemical Society.* Vol. 120, No. 4. pp. 515–518. 1973.

Marcus, P. "Sulfur-Assisted Corrosion Mechanisms and the Role of Alloyed Elements." *Corrosion Mechanisms in Theory and Practice.* P. Marcus and I. Olefjord, eds. New York City, New York: Macel Dekker. p. 239. 1995.

Marcus, P. and J.M. Grimal. "The Antagonistic Roles of Chromium and Sulphur in the Passivation of Ni-Cr-Fe Alloys Studies by XPS and Radiochemical Techniques." *Corrosion Science.* Vol. 31. pp. 377–382. 1990.

Marcus, P. and I. Olefjord. "The Dissolution and Passivation of a Single-Crystal $Ni_{50}Fe_{50}$ Alloy and the Influence of Sulfur Studied by Electron Spectroscopy for Chemical Analysis." *Corrosion Science.* Vol. 42. p. 91. 1986.

Marcus, P., I. Olefjord, and J. Oudar. "The Influence of Sulphur on the Dissolution and the Passivation of a Nickel-Iron Alloy II: Surface Analysis by ESCA." *Corrosion Science.* Vol. 24. pp. 269–278. 1984a.

Marcus, P., A. Teissier, and J. Oudar. "The Influence of Sulphur on the Dissolution and the Passivation of a Nickel-Iron Alloy I: Measurements." *Corrosion Science.* Vol. 24. pp. 259–268. 1984b.

Min, U.-S. and J.C.M. Li. "The Microstructure and Dealloying Kinetics of a Cu-Mn Alloy." *Journal of Materials Research.* Vol. 9. pp. 2,878–2,883. 1994.

Mott, N.F. "The Theory of the Formation of Protective Films on Metals—III." *Transactions of the Faraday Society.* Vol. 43. p. 429. 1947.

NRC. NUREG–1804. "Yucca Mountain Review Plan—Draft Report for Comment." Rev. 2. Washington, DC: NRC. March 2002.

Oldham, K.B. and F. Mansfeld. "Corrosion Rates from Polarization Curve: A New Method." *Corrosion Science.* Vol. 13. pp. 813–819. 1973.

OLI Systems, Inc. "Corrosion Analyzer Software." Version 6.4. Morris Plains, New Jersey: OLI Systems, Inc. 2001.

Oltra, R. and M. Keddam. "Application of Impedance Technique to Localized Corrosion." *Corrosion Science.* Vol. 28, No. 1. pp. 1–18. 1988.
Pensado, O., D.S. Dunn, and G.A. Cragnolino. "Modeling of the Passive Film on Nickel-Chromium-Molybdenum Alloys." Symposium on Corrosion of Metals and Alloys. 2000 Spring Meeting of the Materials Research Society, San Francisco, California, April 24–28, 1999. San Francisco, California: Materials Research Society. 2000.

Rapp, R.A. "Long-Term Extrapolation of Passive Behavior." Proceedings from the International Workshop on Long-Term Extrapolation of Passive Behavior, Arlington, Virginia, July 19–20, 2001. A.A. Sagüés and C.A. Di Bella, eds. Arlington, Virginia: U.S. Nuclear Waste Technical Review Board. 2001.

Sagüés, A.A. and C.A. Di Bella, eds. Proceedings from the International Workshop on Long-Term Extrapolation of Passive Behavior Conference, Arlington, Virginia, July 19–20, 2001. Arlington, Virginia: U.S. Nuclear Waste Technical Review Board. 2001.

Shewmon, P.G. *Diffusion in Solids.* New York City, New York: McGraw-Hill Company. p. 45. 1963.

Schueller, G.R.T. and S.R. Taylor. "Equivalent Circuit Modeling of Aluminum/Polymer Laminates Using Electrochemical Impedance Spectroscopy." *ASTM STP–1188: Electrochemical Impedance—Analysis and Interpretation.* J.R. Scully, D.C. Silverman, and M.W. Kendig, eds. Philadelphia, Pennsylvania: ASTM International. pp. 328–343. 1993.

Scully, J.R. "Electrochemical Corrosion Tests and Standards: Application and Interpretation." R. Boboian, ed. Philadelphia, Pennsylvania: ASTM International. pp. 75–90. 1995.

———. "Characterization of the Corrosion of Aluminum Thin Films Using Electrochemical Impedance Methods." *ASTM STP–1188: Electrochemical Impedance—Analysis and Interpretation.* J.R. Scully, D.C. Silverman, and M.W. Kendig, eds. Philadelphia, Pennsylvania: ASTM International. pp. 276–296. 1993.

Shida, Y., G.C. Wood, F.H. Stott, D.P. Whittle, and B.D. Bastow. "Intergranular Oxidation and Internal Void Formation in Ni-40% Cr Alloys." *Corrosion Science.* Vol. 21, No. 8. pp. 581–597. 1981.

Sieradzki, K., R.R. Coderman, K. Shukla, and R.C. Newman. "Computer Simulations of Corrosion: Selective Dissolution of Binary Alloys." *Philosophical Magazine.* Vol. 159. pp. 713–746. 1989.

Silverman, D.C. "Practical Corrosion Prediction Using Electrochemical Techniques." *Uhlig's Corrosion Handbook.* 2nd Edition. R.W. Revie, ed. New York City, New York: John Wiley and Sons. pp. 1,197–1,225. 2000.

Silverman, D.C. "Tutorial on Cyclic Potentiodynamic Polarization Technique." Proceedings of the Corrosion '98 Conference. Paper No. 299. Houston, Texas: NACE International. 1998.

Silverman, D.C. "On Ambiguities in Modeling Electrochemical Impedance Spectra Using Circuit Analogs." *Corrosion.* Vol. 47, No. 2. pp. 87–89. 1991.

Smallman, R.E. and J.E. Harris, eds. Proceedings of the Metals Society Point Defect Behavior and Diffusional Processes Conference, University of Bristol, London, United Kingdom, September 13–16, 1976. Vacancies 76. London, United Kingdom: The Metals Society. 1977.

Sridhar, N. and G.A. Cragnolino. "Evaluation of Analogs for the Performance Assessment of High-Level Waste Container Materials." CNWRA 2002-02. San Antonio, Texas: CNWRA. 2002.

Steigerwald, R.F. and N.D. Greene. "The Anodic Dissolution of Binary Alloys." *Journal of Electrochemical Society.* Vol. 109. pp. 1,026–1,034. 1962.

Stern, M. and E.D. Weisert. "Experimental Observations of the Relation Between Polarization Resistance and Corrosion Rate." Proceedings of ASTM International. Vol. 59. Philadelphia, Pennsylvania: ASTM International. pp. 1,280–1,291, 1959.

Stern, M. and A.L. Geary. "Electrochemical Polarization I: A Theoretical Analyses of the Shape of Polarization Curves." *Journal of the Electrochemical Society.* Vol. 104, No. 1. pp. 56–63. 1957.

Stott, F.H., G.C. Wood, Y. Shida, D.P. Whittle, and B.D. Bastow. "The Development of Internal and Intergranular Oxides in Nickel-Chromium-Aluminum Alloys at High Temperature." *Corrosion Science.* Vol. 21, No. 8. pp. 599–624. 1981.

Stringer, J. "High-Temperature Oxidation of Metals." Proceedings of the Metals Society Point Defect Behavior and Diffusional Processes Conference, University of Bristol, London, United Kingdom, September 13–16, 1976. R.E. Smallman and J.E. Harris, eds. Vacancies 76. London, United Kingdom: The Metals Society. pp. 201-207. 1977.

———. "Effect of Alloying on Oxidation—Quantitative Treatments." *Metallurgical Reviews (Supplement to Institute of Metals Journal).* Vol. 11. pp. 113–128. 1966.

Sugimoto, K. and Y. Sawada. "The Role of Molybdenum in Austenitic Stainless Steels in the Inhibition of Pitting in Neutral Halide Solutions." *Corrosion.* Vol. 32. pp. 347–352. 1976.

Tikkanen, M.H. and O. Hyvärinen. "Passivity of Nickel-Chromium Alloys." *Acta Polytechnica Scandinavica.* Vol. 85. pp. 1–17. 1969.

Tylecote, R.F. and T.E. Mitchell. "Marker Movements in the Oxidation of Iron and Some Other Metals." *Journal of Iron Steel Institute.* Vol. 196. p. 445. 1960.

Verwey, E.J.W. "Electrolytic Conduction of a Solid Insulator at High Voltages—Formation of the Anodic Oxide Film on Aluminum." *Physica.* Vol. 2. p. 1,059. 1935.

Waste Package Materials Performance Peer Review Panel. "Final Report to the Waste Package Materials Performance Peer Review Panel." Las Vegas, Nevada: DOE. 2002.

Wolfram Research, Inc. *The Mathematica Book.* 4th Edition. Champaign, Illinois: Wolfram Media and Cambridge University Press. 1999.

Zhang, L. and D.D. Macdonald. "Segregation of Alloying Elements in Passive Systems II: Numerical Simulation." *Electrochimica Acta.* Vol. 43. pp. 2,673–2,685. 1998.

Zhang, L., D.D. Macdonald, E. Sikora, and J. Sikora. "On the Kinetics of Anodic Oxide Films." *Journal of Electrochemical Society.* Vol. 145. pp. 898–905. 1998.

APPENDIX A

DERIVATION OF THE POTENTIAL DEPENDENCE OF THE PASSIVE CURRENT DENSITY

DERIVATION OF THE POTENTIAL DEPENDENCE OF THE PASSIVE CURRENT DENSITY

This appendix justifies the statement that the passive current density is independent of the applied potential if the rate of charge transport through the oxide film via cation vacancies is negligible with respect to the rate of charge transport via oxygen vacancies and cation interstitials.

In the original Point Defect Model (Macdonald, 1992), it is proposed that for a passive metal, *M*, forming an oxide of stoichiometric composition, $MO_{\chi/2}$, the fundamental charge transfer reactions controlling the dissolution of the metal at the metal-film interface are (an additional reaction with respect to the original model has been added to account for interstitial dissolution)

$$M \xrightarrow{k_1} M_i^{\chi+} + V_m + \chi e^- \tag{A–1}$$

$$M + V_m^{\chi-} \xrightarrow{k_2} M_M + V_m + \chi e^- \tag{A–2}$$

$$M \xrightarrow{k_3} M_M + \frac{\chi}{2} V_O^{2+} + \chi e^- \tag{A–3}$$

where

χ — oxidation state of the metal
$M_i^{\chi+}$ — cation interstitial in the oxide
V_m — vacancy in the metal
e — electron
$V_M^{\chi-}$ — cation vacancy in the oxide
M_M — metal in the oxide lattice
V_O^{2+} — oxygen vacancy in the oxide
k_p — rate constant, $p = 1,2,3,\ldots 7$

On the other hand, at the film-solution interface the fundamental charge transfer reactions are

$$M_i^{\chi+} \xrightarrow{k_4} M^{\delta+} + (\delta - \chi)e^- \tag{A–4}$$

$$M_M \xrightarrow{k_5} M^{\delta+} + V_M^{\chi-} + (\delta - \chi)e^- \tag{A–5}$$

$$V_O^{2+} + \mathrm{H_2O} \xrightarrow{k_6} \mathrm{O_O} + 2\mathrm{H}^+ \tag{A–6}$$

$$MO_{\chi/2} + \chi\mathrm{H}^+ \xrightarrow{k_7} M^{\delta+} + \frac{\chi}{2}\mathrm{H_2O} + (\delta - \chi)e^- \tag{A–7}$$

where

δ — oxidation state of cation in solution
H^+ — hydrogen ion
H_2O — water molecule
O_O — oxygen in the oxide lattice

The reaction in Eq. (A–3) results in the formation of oxide volume, which can be expressed in mathematical form for a one-dimensional system as

$$\frac{dL_+}{dt} = \Omega k_3 \qquad \text{(A–8)}$$

where

Ω — molar volume of the oxide {in units of cm^3/mol [ft^3/mol] assuming that k_3 is in units of mol/(cm^2 s) [mol/ft^{2}s}
L — oxide thickness at time t

On the other hand, the rate of film dissolution is controlled by the reaction in Eq. (A–9)

$$\frac{dL_-}{dt} = -\Omega\left(a_{H^+}\right)^n k_7 \qquad \text{(A–9)}$$

where

a_{H+} — activity of hydrogen ion
n — reaction order with respect to the hydrogen ion activity

Therefore, the expression defining the overall film growth is

$$\frac{dL}{dt} = \Omega k_3 - \Omega\left(a_{H^+}\right)^n k_7 \qquad \text{(A–10)}$$

Under the steady-state condition, $dL/dt = 0$, the rate constants k_3 and k_7 are related as

$$k_3 = \left(a_{H^+}\right)^n k_7 \qquad \text{(A–11)}$$

Equation (A–11) is significant because it can be used to relate the potential drop at the metal-film interface, $\phi_{m/f}$, to the potential drop at the film-solution interface, $\phi_{f/s}$, using the formalism of the Point Defect Model. The Point Defect Model postulates (Macdonald, 1992) that the potential drop at the film-solution interface is proportional to the total applied potential to the system, V, that is,

$$\phi_{f/s} = \alpha V + V_o \qquad \text{(A–12)}$$

where V_o is a constant. The Point Defect Model proposes that the rate constants follow an exponential dependence with respect to the change in potential energy; that is,

$$k_3 = k_3^o e^{\alpha_3 \frac{F}{RT} \chi \phi_{m/f}} \tag{A–13}$$

where

k_3^o — a reference rate constant

α_3 — transfer coefficient, positive and less than one

F — Faraday's constant

R — ideal gas constant

T — absolute temperature

Similarly, for the reaction in Eq. (A–7), the rate constant is defined as

$$k_7 = k_7^o e^{\alpha_7 \frac{F}{RT} (\delta - \chi) \phi_{f/s}} \tag{A–14}$$

where

k_7^0 — a reference rate constant

α_7 — transfer coefficient

From Eq. (A–11), a relationship between the potential drop at the metal-film interface, $\phi_{m/f}$, and the potential drop at the film-solution interface, $\phi_{f/s}$, is derived

$$\phi_{m/f} = \frac{\alpha_7(\delta - \chi)}{\alpha_3 \chi} \phi_{f/s} + \frac{RT}{\alpha_3 \chi F} \ln\left(a_{H^+}^{\,n} \frac{k_7^o}{k_3^o} \right) \tag{A–15}$$

For steady-state conditions, the potential drop at the metal-film interface is proportional to the corresponding drop at the film-solution interface, which is assumed proportional to the total applied potential. Note that if there is no change in the oxidation state of the cation transferred from oxide film to the solution (i.e., $\delta = \chi$), the potential drop at the metal-film interface is independent of the applied potential.

If I is the current density {in units of A/cm^2 [A/ft^2]} vector, conservation of charge requires that

$$\nabla \cdot I = -\frac{\partial \rho}{\partial t} \tag{A–16}$$

where ρ is the charge density {expressed in units of Coulomb/cm^3 [Coulomb/ft^3]}. Under steady-state conditions, the right side of Eq. (A–16) is zero. Therefore, at steady state and for a one-dimensional problem, the current density is independent of the spatial coordinate. For the case $\delta = \chi$, the current density at the metal-film interface (which is the same at any point in the system) is computed as

$$I = \chi F\left(k_1 + k_3\right) + \chi F\, a_{V_M^{\chi'}}\, k_2 \tag{A–17}$$

where $a_{V_M^{\chi'}}$ is the cation-vacancy activity in the proximity of the metal-film interface. Note that if the rate of charge transport via cation vacancies is negligible with respect to the rate of charge transport of cation interstitials or oxygen vacancies (i.e., $k_2 << k_1, k_3$), Eq. (A–17) reduces to

$$I \approx \chi F(k_1 + k_3) \tag{A–18}$$

Likewise k_3, k_1 is dependent on the potential drop at the metal-film interface, $\phi_{m/f}$. The drop $\phi_{m/f}$ has been argued to be independent of the applied potential for the case $\delta = \chi$. Therefore, Eq. (A–18) implies that the current density is independent of the applied potential, if cation interstitials or oxygen vacancies are the predominant charge carriers.

If, on the other hand, cation vacancies are the dominant charge carriers, Eq. (A-17) becomes

$$I \approx \chi F\, a_{V_M^{\chi'}}\, k_2 = \chi F k_5 = \chi F k_5^{\circ} e^{\alpha_5 \frac{F}{RT} \chi \phi_{f/s}} \tag{A–19}$$

where

α_5 — transfer coefficient
k_5^{o} — a reference rate constant

The second equality results from requiring that the rate of cation vacancy creation, from Eq. (A-5), be the same as the rate of cation vacancy annihilation, from Eq. (A-2). The third equality in Eq. (A–19) is the exponential expansion of the rate constant as dictated by the Point Defect Model. Because the potential drop $\phi_{f/s}$ is assumed proportional to the total applied potential, it follows that for systems in which cation vacancies are the predominant charge carriers, the passive current density is an exponential function of the applied potential

A discussion of the more complex alloy system is presented as follows. In developing the model in Chapter 5[1] for the dissolution of nickel-chromium-molybdenum alloys, it was assumed that cations do not experience a change in oxidation state in the transfer from the oxide to the solution. Consistent with arguments in this appendix, it was assumed in Chapter 5[2] that the potential drop at the metal-film interface is independent of the applied potential. Under steady-state conditions, the current density at the metal-film interface is computed as

$$I = F\left[\chi a_{\mathrm{Cr}}\left(k_1^{\mathrm{Cr}} + k_3^{\mathrm{Cr}} + a_{V_{\mathrm{Cr}}^{\chi'}} k_2^{\mathrm{Cr}}\right) + \delta a_{\mathrm{Ni}}\left(k_1^{\mathrm{Ni}} + k_3^{\mathrm{Ni}} + a_{V_{\mathrm{Cr}}^{\chi'}} k_2^{\mathrm{Ni}}\right) + \xi a_{\mathrm{Mo}} k_1^{\mathrm{Mo}}\right] \tag{A–20}$$

where

χ, δ, ξ — oxidation state of chromium, nickel, and molybdenum, respectively

a_M — atomic fraction of element M (= Cr, Ni, Mo)

k_n^M — rate constant, the superscript M (= Cr, Ni, Mo) and subscript n (= 1,2,3) are used to label particular species and reactions. See Chapter 5[3] for additional details in the notation

$a_{V_{\mathrm{Cr}}^{\chi'}}$ — activity of cation vacancies at the metal-film interface

Experimentally it is known that the passive current density for Alloy 22 is independent of the applied potential over a wide range up to the potential for transpassive dissolution (Dunn, et al., 1999, 2000). According to the assumptions in Chapter 5[4], this independence is possible only if the rate of cation vacancy transport is negligible with respect to the rate of interstitial or oxygen vacancy transport (i.e., $a_{V_{\mathrm{Cr}}^{\chi'}} k_2^{\mathrm{Cr}} << k_1^{\mathrm{Cr}}, k_3^{\mathrm{Cr}}$ and $a_{V_{\mathrm{Cr}}^{\chi'}} k_2^{\mathrm{Ni}} << k_1^{\mathrm{Ni}}, k_3^{\mathrm{Ni}}$). In other words, using steady-state constraints, it can be argued (similar to other arguments developed in this appendix) that the terms $a_{V_{\mathrm{Cr}}^{\chi'}} k_2^{\mathrm{Cr}}$ and $a_{V_{\mathrm{Cr}}^{\chi'}} k_2^{\mathrm{Ni}}$ are functions of the applied potential; therefore, these terms should not be important contributors to the current density for the Alloy 22 system. Equation (5-16) follows from this observation. The predominant charge carriers, consistent with the Point Defect Model, should be cation interstitials or oxygen vacancies. Chapter 5[5] provides additional arguments in favor of the interstitial transport mechanism.

---

[1] Pensado, O., D.S. Dunn, G.A. Cragnolino, and V. Jain. "Passive Dissolution of Container Materials, Modeling, and Experiments." San Antonio, Texas: CNWRA. Unpublished report, 2002.

[2] Ibid.

[3] Pensado, O., D.S. Dunn, G.A. Cragnolino, and V. Jain. "Passive Dissolution of Container Materials, Modeling, and Experiments." San Antonio, Texas: CNWRA. Unpublished report, 2002.

[4] Ibid.

[5] Ibid.

REFERENCES

Dunn, D.S, Y.-M. Pan, and G.A, Cragnolino. "Stress Corrosion Cracking, Passive, and Localized Corrosion of Alloy 22 High-Level Radioactive Waste Containers." Proceedings of the Corrosion 2000 Conference. Paper No 00206. Houston, Texas: NACE International. 2000.

Dunn, D.S., Y.-M. Pan, and G.A. Cragnolino. "Effects of Environmental Factors on the Aqueous Corrosion of High-Level Radioactive Waste Containers—Experimental Results and Models." CNWRA Report 99-004. San Antonio, Texas: CNWRA. 1999.

Macdonald, D.D. "The Point Defect Model for the Passive State." *Journal of Electrochemical Society*. Vol. 139. pp. 3,434–3,449. 1992.

APPENDIX B

FINITE DIFFERENCE IMPLEMENTATION OF THE SOLD-STATE DIFFUSION PROBLEM

FINITE DIFFERENCE IMPLEMENTATION OF THE SOLD-STATE DIFFUSION PROBLEM

This appendix provides a detailed discussion of the finite difference implementation of the constitutive equation and mass conservation equation describing the transport of vacancies and atoms in the alloy.

In Chapter 5[1] it was discussed that the constitutive equation for the diffusion of vacancies in the metal is

$$J_v = -\frac{1}{c_v^o}\sum_A D_A c_A \nabla c_v + \frac{c_v}{c_v^o}\sum_A D_A \nabla c_A \qquad \text{(B–1)}$$

where

J_v	—	flux of vacancies
c_A	—	concentration of specie A (A = Ni, Cr, Mo)
D_A	—	diffusion coefficient for element A in the bulk of the alloy
c_v	—	concentration of vacancies in the alloy
c_v^o	—	equilibrium concentration of vacancies at a reference temperature

Mass conservation demands that

$$\frac{\partial c_v}{\partial t} = -\nabla \cdot J_v = \frac{1}{c_v^o}\sum_A D_A c_A \nabla^2 c_v - \frac{c_v}{c_v^o}\sum_A D_A \nabla^2 c_A \qquad \text{(B–2)}$$

If it is assumed that the vacancy concentration is negligible with respect to the atom concentration in the alloy, Eq. (B–2) can be approximated as

$$\frac{\partial c_v}{\partial t} \approx \frac{1}{c_v^o}\sum_A D_A c_A \nabla^2 c_v = D_{\mathrm{eff}} \nabla^2 c_v \qquad \text{(B–3)}$$

The effective diffusion coefficient, D_{eff}, is not constant but nearly constant if the concentration of vacancies is negligible. Without requiring that the concentration of vacancies be negligible, but requesting the diffusion coefficient be similar (i.e., $D_{\mathrm{Ni}} \cong D_{\mathrm{Cr}} \cong D_{\mathrm{Mo}} = D$) and the total sites in the alloy be constant (i.e., $c_{\mathrm{Ni}}+c_{\mathrm{Cr}}+c_{\mathrm{Mo}}+c_v = c_T$), Eq. (A–2) can be simplified, without additional approximations, into

$$\frac{\partial c_v}{\partial t} = -\nabla \cdot J_v = \frac{c_T}{c_v^o} D \nabla^2 c_v = D_{\mathrm{eff}} \nabla^2 c_v \qquad \text{(B–4)}$$

---

[1] Pensado, O., D.S. Dunn, G.A. Cragnolino, and V. Jain. "Passive Dissolution of Container Materials, Modeling, and Experiments." San Antonio, Texas: CNWRA. Unpublished report, 2002.

The effective diffusion coefficient, D_{eff}, is a constant. Results reported in Chapter 5[2] are based on Eq. (B–4). The finite difference equations implemented to integrate a one-dimensional representation of Eq. (B–4) are described next.

Let the timestep and position step of the finite difference implementation be represented as Δt and Δx. Let the dimensionless parameter λ be defined as

$$\lambda = D_{\mathrm{eff}} \frac{\Delta t}{\Delta x^2} \tag{B–5}$$

The parameter, λ, must be less than or equal to 0.5 to guarantee convergence of the finite difference computations. For the sake of simplicity in the notation, concentrations are referred to with two subscripts, $c_{i,j}$. The first subscript, i, tracks the time step and the second subscript, j, tracks the position. Superscripts v (for vacancies), Ni, Cr, and Mo are used to differentiate the particular species being considered (e.g., $c_{i,j}^{v}$ or $c_{i,j}^{\mathrm{Ni}}$). The metal-oxide interface is located at the spatial step $j = 0$. The spatial steps range from $j = 0$ to $j = N$. A free boundary in the metal is constructed at the position step $j = N$. The temporal steps start at $i = 0$ (initial time).

B.1 Finite Difference Equations to Determine Vacancy Concentrations

At the i^{th} timestep, the total vacancies in the system, c_i^{vT}, is defined as

$$c_i^{vT} = \sum_{j=0}^{N} c_{i,j}^{v} \tag{B–6}$$

The total vacancies injected into the system, inj_i, as a result of the alloy dissolution process, between the time steps i and $i + 1$, is computed as

$$inj_i = \frac{\Delta t}{c_T \Delta x} \sum_{A} k_1^A c_{i,0}^A \tag{B–7}$$

The symbol k_1^A (A—Ni, Cr, and Mo) represents rate constants for the reactions in Eqs. (5-1), (5-2), and (5-3) in Chapter 5.[3]

---

[2] Pensado, O., D.S. Dunn, G.A. Cragnolino, and V. Jain. "Passive Dissolution of Container Materials, Modeling, and Experiments." San Antonio, Texas: CNWRA. Unpublished report, 2002.

[3] Ibid.

A free boundary is constructed at the position step $j = N$. A free boundary can release or receive vacancies depending on the concentration gradient and Fick's law. The number of vacancies leaving the system, ej_i, between the time steps i and $i + 1$, is computed as

$$ej_i = \lambda\left(c^v_{i,N-1} - c^v_{i,N}\right) \tag{B–8}$$

If the system between the position step $j = 0$ and $j = N$ was a closed system, all vacancies injected to the system would remain in the system, and, for that particular case, by definition, $ej_i = 0$.

Equations (B–6), (B–7), and (B–8) allow the computation of the total vacancies at the time step $i + 1$ to be

$$c^{vT}_{i+1} = c^{vT}_i + inj_i - ej_i \tag{B–9}$$

Concentrations at positions $j = 1,\ldots,N\text{-}1$, for a new timestep, $i + 1$, are computed from a first-order finite difference representation of Eq. (B–4)

$$c^v_{i+1,j} = c^v_{i,j} + \lambda\left(c^v_{i,j-1} - 2c^v_{i,j} + c^v_{i,j+1}\right) \quad j = 1,\ldots,N-1 \tag{B–10}$$

At the spatial step, $j = N$ (the free boundary), the vacancy concentration is computed according to logarithmic extrapolation

$$c^v_{i+1,N} = \frac{\left(c^v_{i+1,N-1}\right)^2}{c^v_{i+1,N-2}} \tag{B–11}$$

Finally, the concentration of vacancies at the metal-film interface, $j = 0$, at the new timestep, $i + 1$, is computed by requesting conservation of mass

$$c^v_{i+1,0} = c^{vT}_{i+1} - \sum_{k=1}^{N} c^v_{i+1,k} \tag{B–12}$$

Note that from Eq. (B–12), it follows that $c^{vT}_{i+1} = \sum_{j=0}^{N} c^v_{i+1,j}$, which guarantees, by induction, that Eq. (A–6) is valid for all timesteps. Equation (B–7) requires determination of the atom concentrations at the interface. Therefore, the complete coupled diffusion problem must be solved to compute the concentration of vacancies. Note also that finite difference computations of two simulations having the same kinetic parameters will be identical if λ and the ratio, $\Delta t/\Delta x$, are the same for both simulations. In other words, simulations having constant ratios of $\Delta t/\Delta x$ and $D_{eff}/\Delta x$ will yield identical results.

B.2 Finite Difference Equations To Determine Atom Concentrations

Concentrations at a new timestep, $i+1$, for the position steps $j = 1,\ldots,N-1$ are computed as

$$c^A_{i+1,j} = c^A_{i,j} + \left(c^v_{i,j} - c^v_{i+1,j}\right) F^A_{i,j} \quad j = 1,..,N-1 \tag{B–13}$$

The second term on the right side of Eq. (B–13) is the decrease in the concentration caused by the diffusive transport of vacancies. The factor $F^A_{i,j}$ satisfies $F^{\mathrm{Ni}}_{i,j} + F^{\mathrm{Cr}}_{i,j} + F^{\mathrm{Mo}}_{i,j} = 1$ to be consistent with the assumption $c_{\mathrm{Ni}}+c_{\mathrm{Cr}}+c_{\mathrm{Mo}}+c_v= c_T$. This factor is defined later in this appendix. It is straightforward to demonstrate by induction that if $c^{\mathrm{Ni}}_{i,j} + c^{\mathrm{Cr}}_{i,j} + c^{\mathrm{Mo}}_{i,j} + c^v_{i,j} = c_T$, then Eq. (B–13) guarantees that the total number or sites is a constant for any later timestep.

The concentration at the free interface, $j = N$, is computed by logarithmic extrapolation and corrected to enforce that the total number of sites is a constant

$$c^A_{i+1,N} = \left(c_T - c^v_{i+1,N}\right) \frac{\left(c^A_{i+1,N\text{-}1}\right)^2 \Big/ c^A_{i+1,N\text{-}2}}{\sum\limits_B \left(c^B_{i+1,N\text{-}1}\right)^2 \Big/ c^B_{i+1,N\text{-}2}} \tag{B–14}$$

Finally, the concentration at the interface, $j = 0$, is computed as follows

$$c^A_{i+1,0} = \sum_{j=0}^{N} c^A_{i,j} - \frac{c^A_{i,0}}{c_T} k^A_1 \frac{\Delta t}{\Delta x} + ej_i \times F^A_{i,N} - \sum_{j=1}^{N} c^A_{i+1j} \tag{B–15}$$

Equation (B–15) is consistent with the conservation of the mass requirement that the total atoms ejected from the system at the metal-film interface complements the atoms remaining in the system, or, in mathematical representation

$$\sum_{j=0}^{N} c^A_{i+1j} = \sum_{j=0}^{N} c^A_{i,j} - \frac{c^A_{i,0}}{c_T} k^A_1 \frac{\Delta t}{\Delta x} + ej_i \times F^A_{i,N} \tag{B–16}$$

Equation (B–13) through (B–16) are general and independent of the relative magnitude of diffusion coefficients. If it is assumed that the solid-state diffusion coefficients are similar, a simplified expression for the factor $F^A_{i,j}$ can be derived. The constitutive equation for the diffusion of atoms is

$$J_A = -\frac{D}{c^o_v}\left(c_v \nabla c_A - c_A \nabla c_v\right) \tag{B–17}$$

Let $J^{A\,\mathrm{in}}_{i,j}$ and $J^{A\,\mathrm{out}}_{i,j}$ be the flux of atoms jumping in and out of the spatial element, *j*. From Eq. (B-16), it follows that

$$J^{A\,\mathrm{in}}_{i,j} \propto c^{v}_{i,j}\left(c^{A}_{i,j+1} - c^{A}_{i,j}\right) - c^{A}_{i,j}\left(c^{v}_{i,j+1} - c^{v}_{i,j}\right) \tag{B–18}$$

and

$$J^{A\,\mathrm{out}}_{i,j} \propto c^{v}_{i,j}\left(c^{A}_{i,j} - c^{A}_{i,j-1}\right) - c^{A}_{i,j}\left(c^{v}_{i,j} - c^{v}_{i,j-1}\right) \tag{B–19}$$

Let $\Delta c^{A}_{i,j}$ be the increase in concentration caused by diffusion transport. For *j* = 1 ... *N*-1 the following relationship holds

$$\Delta c^{A}_{i,j} \propto J^{A\,\mathrm{in}}_{i,j} - J^{A\,\mathrm{out}}_{i,j} \propto c^{V}_{i,j}\left(c^{A}_{i,j+1} - 2c^{A}_{i,j} + c^{A}_{i,j-1}\right) - c^{A}_{i,j}\left(c^{V}_{i,j+1} - 2c^{V}_{i,j} + c^{V}_{i,j-1}\right) \tag{B–20}$$

The fraction, $F^{A}_{i,j}$, can be immediately derived from Eq. (B–20) for *j* = 1 ... *N*-1

$$F^{A}_{i,j} = \frac{c^{v}_{i,j}\left(c^{A}_{i,j+1} - 2c^{A}_{i,j} + c^{A}_{i,j-1}\right) - c^{A}_{i,j}\left(c^{v}_{i,j+1} - 2c^{v}_{i,j} + c^{v}_{i,j-1}\right)}{-c_T\left(c^{v}_{i,j+1} - 2c^{v}_{i,j} + c^{v}_{i,j-1}\right)} \quad j=1,..,N-1 \tag{B–21}$$

The denominator in Eq. (B–21) is obtained by adding the numerator for nickel, chromium, and molybdenum, and assuming the total concentration is a constant equal to c_T. Finally, the factor $F^{A}_{i,N}$ needed in Equation (B–15) is computed as

$$F^{A}_{i,N} = \frac{c^{v}_{i,N}\left(c^{A}_{i,N} - c^{A}_{i,N-1}\right) - c^{A}_{i,0}\left(c^{v}_{i,N} - c^{v}_{i,N-1}\right)}{-c_T\left(c^{v}_{i,N} - c^{v}_{i,N-1}\right)} \tag{B–22}$$

Equation (B–21) is a postulated equation, that is suggested by Eq. (B–20). Likewise, in Eq. (B–20), the denominator in Eq. (B–21) is obtained by adding the numerator for Ni, Cr, and Mo and assuming the total concentration is a constant equal to c_T.

The system of equations in this appendix is valid provided that the diffusion coefficients in the bulk of the alloy are similar for all alloy components. If this assumption is not valid, it may be possible the existence of enhanced transport of one of the alloy components toward the interface. Equations developed in this appendix can be extended to address the case of dissimilar diffusion.